



**HAL**  
open science

# Design and synthesis of mechanical systems with coupled units

Yang Zhang

► **To cite this version:**

Yang Zhang. Design and synthesis of mechanical systems with coupled units. Mechanical engineering [physics.class-ph]. INSA de Rennes, 2019. English. NNT : 2019ISAR0004 . tel-02307221

**HAL Id: tel-02307221**

**<https://theses.hal.science/tel-02307221v1>**

Submitted on 7 Oct 2019

**HAL** is a multi-disciplinary open access archive for the deposit and dissemination of scientific research documents, whether they are published or not. The documents may come from teaching and research institutions in France or abroad, or from public or private research centers.

L'archive ouverte pluridisciplinaire **HAL**, est destinée au dépôt et à la diffusion de documents scientifiques de niveau recherche, publiés ou non, émanant des établissements d'enseignement et de recherche français ou étrangers, des laboratoires publics ou privés.

# THESE DE DOCTORAT DE

L'INSA RENNES  
COMUE UNIVERSITE BRETAGNE LOIRE

ECOLE DOCTORALE N° 602  
*Sciences pour l'Ingénieur*  
Spécialité : « *Génie Mécanique* »

Par

« **Yang ZHANG** »

« **DESIGN AND SYNTHESIS OF MECHANICAL SYSTEMS WITH  
COUPLED UNITS** »

Thèse présentée et soutenue à Rennes, le 19.04.2019

Unité de recherche : LS2N

Thèse N° : 19ISAR 06 / D19 - 06

## Rapporteurs avant soutenance :

**BEN OUEZDOU Féthi**  
Professeur des Universités, UVSQ, Versailles  
**DELALEAU Emmanuel**  
Professeur des Universités, ENIB, Brest

## Composition du Jury :

**WENGER Philippe**  
Directeur de Recherche CNRS, LS2N Nantes / Président  
**BEN OUEZDOU Féthi**  
Professeur des Universités, UVSQ, Versailles / Rapporteur  
**DELALEAU Emmanuel**  
Professeur des Universités, ENIB, Brest / Rapporteur  
**COSTE Michel**  
Professeur Emerite, IRMAR, Université de Rennes 1 / Examineur  
**AOUSTIN Yannick**  
Professeur des Universités, Université de Nantes / Examineur  
**SMITH-GUERIN Natalie**  
Maître de Conférences, Université d'Orléans / Examineur

Directeur de thèse  
**ARAKELYAN Vigen**  
Professeur des Universités, INSA de Rennes

Intitulé de la thèse :

Design and Synthesis of Mechanical Systems  
with Coupled Units

Yang ZHANG

En partenariat avec :



*Document protégé par les droits d'auteur*



---

---

# Abstract

---

---

This thesis deals with the design principles, which are based on the coupling of two mechanical structures. The criteria for optimal design and the types of combined units are different. However, all the tasks are considered in coupling of given mechanical units. The thesis consists of 5 chapters, conclusions, appendices and bibliography.

The critical review given in the first chapter is divided into three sections due to the nature of the examined problems: legged walking robots, gravity compensators used in robots and collaborative robots. It is shown that the design principles used for the development of these devices and robots can be represented as the coupling systems of different mechanical units. The optimal coupling of these units and their improved design can significantly enhance the performance of robots.

Chapter 2 deals with the development of single actuator walking robots designed by coupling of two mechanisms. The advantage of such systems is the simplicity of the design and its control system. Three various design concepts are considered. In the first section of the chapter 2, the single actuator walking robot is designed via coupling of two four-bar linkages. For this purpose, the geometric synthesis of the four-bar linkage through the prescribed path has been developed. Based on the Genetic Algorithm, the synthesis allows one to ensure the reproduction of prescribed points of the given trajectory obtained from the walking gait. The actuator mounted on the robot's frame moves both legs, which are four-bar linkages. A walking robot designed by suggested concept can move both forward and backward directions. The observations showed that such a robot can ensure only a constant step during the walking gait. The adjustment of geometric parameters of a four-bar linkage to obtain variable lengths of steps is a fairly complex problem. Therefore, in the next section, the design of a single actuator walking robot based on the coupling of slider-crank mechanisms is considered. It is shown that the length of the step can be modified via changing the offset of the slider guide. The adjustment of the offset of the slider guide allows one to obtain steps with variable lengths. However, that does not allow one to change the form and the orientation of steps. Hence, in the last section of the chapter, the design of a single walking robot via coupling of a cam mechanism and a pantograph linkage is discussed. In this case, the adjustable parameters are the angle between the cam mechanism and the robot moving frame, as well as the input points of the pantograph mechanism. The proposed concept allows significant variations of the walking speed during the horizontal displacements of the robot and climbing stairs.

Chapter 3 deals with the design and synthesis of gravity balancers. In the proposed design concepts, a rotating link to be balanced is coupled with a two-link dyad. It is known that a fully gravity compensation of a rotating link cannot be achieved when a non-zero free length spring, i.e. conventional linear spring, is used. To use non-zero length springs, it is necessary to apply auxiliary mechanical systems. The first section of the chapter 3 deals with a simple and analytically tractable solution permitting to carry out quasi-perfect balancing of a rotating link by means of a non-zero length spring. In the proposed design the balancing spring is connected with the rotating link

by means of an articulated dyad forming a four-bar linkage. Upon rotation of the output link of the four-bar mechanism moves the end of the spring and changes the length of the spring creating a variable balancing moment. An optimization method based on the geometric synthesis of four-bar mechanism and potential energy conservation is developed, which allows one to control the optimal displacements of the spring providing a suitable balancing moment. The second section of the chapter 3 deals with a similar problem by coupling a rotating link to be balanced and an articulated dyad with prismatic pair, forming with the rotating link a slider-crank mechanism. The particularity of the suggested structural concept is that the balancing spring is installed on the fixed frame, which allows one to reduce the errors due to the spring's weight. Upon rotation of the link moves the end of the spring and changes the length of the spring creating a variable balancing moment. A similar optimization method with some modifications devoted to the geometric synthesis was applied. In the last section of the chapter, it is proposed an improved solution for reduction the error caused by neglecting the masses of the spring and associated links. It is based on the inverted slider crank mechanism considering the masses of the rocker and the spring. It is shown that the errors caused by neglecting the masses of the associated links lead to a significant unbalanced moment. Then, it is proposed to use the minimization of the root-mean-square value of the unbalanced moment to reduce these errors.

Chapter 4 considers the design and study of an exosuit that can provide assistance to people carrying heavy load. The proposed exosuit presents a symbiosis of two systems: rigid lightweight support and cable system. The cable system is mounted on the rigid lightweight support permitting to compensate the gravitational force of a heavy load. The exosuit is made up of high-intensity polyethylene cables which are very light and add almost zero inertia to users. A cable winding and locking mechanism has been designed in order to keep cables in tension while users changing their postures and meanwhile stop the movement of the cables while users carrying loads. The chapter is organized as follows. In the first part, the design concept of the exosuit is presented. Then, the kinematic and dynamic models of the exsuit-human coupled system are established. In the third section, the static, kinematic and dynamic simulations with the optimization of the distribution of the cable attaching positions of the proposed coupled system is considered. Finally, the experimental results carried out on a mannequin test bench are presented.

In the last chapter, a coupled system including a hand-operated balanced manipulator (HOBM) and an industrial collaborative robot is presented. The aim of such a cooperation is to manipulate heavy payloads with less powerful robots. In other term, in the coupled system for handling of heavy payloads by a HOBM, an operator is replaced by a cobot. The advantages of the coupled HOBM and cobot are disclosed and the optimal design of the cooperative workspace is discussed. The Behavior of the coupled system in a static mode when the velocities of the HOBM are limited does not present any special problems. In this mode, the inertial forces are significantly lower than the gravitational one. The payload is completely balanced by the HOBM and the cobot assumes the prescribed displacements with low load. However, in the dynamic mode, the HOBM with massive links creates additional loads on the cobot due to the inertia effect, which can be significant. The determination of inertia effects of the HOBM on the cobot is considered. Dynamic analysis of the coupled system is performed and methods for reducing the oscillation of the HOBM at the final phase of the prescribed trajectories are proposed.

---

---

## Acknowledgement

---

---

Before starting my Ph.D. dissertation, I would like to say a few words to the people who have supported me and had a good time together during the 42-month study.

Firstly, I would like to express my sincere gratitude to my supervisor Prof. Vigen ARAKELIAN for continuous support and valuable discussion during my Ph. D. studies. This dissertation cannot be finished without his tremendous experience in robotics and mechanism design and his patient guidance. I also learned a lot from his rigorous attitude and passion for research work which would be very helpful for my future research career.

This work has been supported by China Scholarship Council (CSC) and INSA de Rennes. I would like to thank CSC for the financial support and the opportunity to study in France.

I would also like to express my thanks to the two rapporteurs of my thesis, Prof. Féthi BEN OUEZDOU and Emmanuel DELALEAU, and the other member of my thesis defense committee, Prof. Philippe ZENGER, Yannick Aoustin, Michel COSTE and Dr. Natalie SMITH-GUERIN. Their insightful comments and recommendations helped a lot to the quality of my thesis and also encouraged me to widen my research from various perspective.

Besides, I would like to express my gratitude to the people and collaborators who helped me for my Ph.D. researches. Thanks to Patrick WEBER and to all the members of the C.C.M. (Manufacturing Centre of Mechanics) of INSA, for their help during the fabrication of mannequin testbench for the robotic suit. And I also thanks to Dr. Baptiste VÉRON for his help for the experiments of cobot-HOBM coupled system.

I also wish to thank to the other Ph.D. students in our research group MECAPROCE (Jing, Léo, Elias), we had a good time and shared an excellent word atmosphere during my study. I would like to express my thanks as well to all my friends in Rennes and the teammates of basketball team PANDA, we had unforgettable memories in this beautiful city and fight for the championship in the courts.

Finally, I would like to express my sincere gratitude to my mom Yang Baohua and my father Zhang Jianhua, your silent supports and comprehension during my study ten thousand kilometers away from home.





---

---

# Table of Contents

---

---

<b>Abstract.....</b>	<b>I</b>
<b>Acknowledgement.....</b>	<b>III</b>
<b>Table of Contents.....</b>	<b>V</b>
<b>List of Figures.....</b>	<b>XI</b>
<b>List of Tables .....</b>	<b>XVII</b>
<b>Chapter 1 Introduction .....</b>	<b>1</b>
1.1 Legged Walking Robot.....	2
1.1.1 Multi-degree-of-freedom legged walking robots .....	2
1.1.2 Reduced-degree-of-freedom walking robots.....	5
1.2 Gravity Compensation in Robotics.....	8
1.2.1 Gravity compensation by counterweights .....	9
1.2.2 Gravity compensation by auxiliary actuators.....	11
1.2.3 Gravity compensation by springs and auxiliary mechanisms .....	13
1.3 Collaborative robotics.....	18
1.3.1 Hand-operated balanced manipulator (HOBM).....	18
1.3.2 Wearable robotic devices for power assistance and rehabilitation.....	23
1.3.3 Collaborative industrial robot.....	29
1.4 Outline of the thesis .....	32
<b>Chapter 2 Design and synthesis of single actuator walking robots via coupling of linkages .....</b>	<b>35</b>
2.1 Design and synthesis of a single actuator walking robot via coupling of four-bar linkages .....	37
2.1.1 Introduction .....	37

2.1.2	Synthesis of the four-bar linkage via genetic algorithm.....	37
2.1.3	Design of the walking robot with one actuator via four-bar mechanism.....	41
2.1.4	Illustrative example with CAD simulation results .....	44
2.2	Design and synthesis of a single actuator walking robot via coupling adjustable slider-crank mechanisms .....	46
2.2.1	Introduction .....	46
2.2.2	Synthesis of adjustable slider-crank mechanisms .....	47
2.2.3	Design of the single actuator walking robot via adjustable slider-crank mechanism.....	49
2.2.4	Illustrative example with CAD simulation results .....	50
2.3	Design and synthesis of a single actuator walking robot via coupling of the driven cam system and the pantograph mechanism .....	53
2.3.1	Introduction .....	53
2.3.2	Design of the walking robot with adjustable parameters .....	53
2.3.3	Properties of the proposed walking robot and its CAD model.....	55
2.3.4	Simulation results .....	56
2.4	Summary.....	60

## **Chapter 3 Design and synthesis of gravity balancers with coupled units** ..... **61**

3.1	Design and synthesis of a gravity balancer via coupling a rotating link and a dyad with revolute joints .....	62
3.1.1	Introduction .....	62
3.1.2	Design concept of a gravity compensator by creating a four-bar mechanism.....	62
3.1.3	Optimization of gravity balancer based on the geometric synthesis of four-bar linkage and potential energy conservation .....	63
3.1.4	Illustrative example with simulation results.....	67

---

3.2	Design and synthesis of a gravity balancer via coupling a rotating link and a dyad with a prismatic pair .....	67
3.2.1	Introduction .....	67
3.2.2	Design concept of a gravity compensator by creating a slider-crank mechanism.....	68
3.2.3	Optimization of gravity balancer based on geometric synthesis of slider-crank mechanism and potential energy conservation.....	68
3.2.4	Illustrative examples with simulation results .....	72
3.3	Improved design of gravity compensators based on the inverted slider crank mechanism.....	74
3.3.1	Introduction .....	74
3.3.2	Improvement of the balancing accuracy by taking into account the masses of auxiliary links coupled with the rotating arm .....	74
3.3.3	Illustrative example with error analysis .....	81
3.4	Summary.....	83
<b>Chapter 4 Design and optimization of a new robotic suit for load carriage via coupling cables and a rigid support.....</b>		<b>85</b>
4.1	Design concept .....	86
4.1.1	Development of the robotic suit's rigid frame .....	86
4.1.2	Coupling of cables with the rigid frame.....	87
4.1.3	Robotic suit operation .....	88
4.2	Modelling of the robotic suite .....	89
4.2.1	Kinematic and geometric modelling .....	89
4.2.2	Dynamic modeling .....	91
4.3	Simulations, optimization, and control of the robotic suite.....	93
4.3.1	Static simulations and optimization .....	93
4.3.2	Workspace analysis .....	98
4.3.3	Dynamic simulations and controller design .....	99

4.4	Experimental validation of obtained results .....	102
4.5	Summary.....	104
<b>Chapter 5 Design and optimization of a mechanical system coupling hand operated balanced manipulator with cobot.....</b>		<b>107</b>
5.1	Design concept of coupling HOBM with cobot .....	108
5.1.1	Statement of the problem.....	108
5.1.2	Proposed coupled system .....	108
5.1.3	Optimal design of the collaborative workspace of the coupled system.....	109
5.2	Dynamic analysis of the coupled system and methods for reducing oscillations in the final phase of the trajectories.....	111
5.2.1	Dynamic modelling and oscillation analysis of the coupled system in the final phase of generated trajectories .....	111
5.2.2	Redaction of oscillations in the final phase of generated trajectories by introducing a rigid vertical axis .....	115
5.2.3	Redaction of oscillations in the final phase of generated trajectories by introducing damping moments .....	117
5.3	Dynamic modeling of the HOBM-cobot coupled system for determining admissible trajectories of the cobot .....	119
5.3.1	Dynamic modeling of the cobot UR10.....	119
5.3.2	Dynamic modelling of the HOBM .....	123
5.3.3	Loads of inertial forces on the cobot for the HOBM with a vertical rigid axis.....	125
5.3.4	Loads of inertial forces on the cobot after introducing damping moments... ..	126
5.3.5	Determination of admissible trajectory of the cobot while payload and HOBM are connected via a vertical rigid axis .....	129
5.3.6	Determination of admissible trajectory of the cobot after introducing damping moments on the HOBM.....	131
5.4	Summary.....	134

**Conclusion and future works.....137**

**Bibliography .....141**

**Appendix A Kinematic and dynamic equation of the robotic suit ..151**

**Appendix B Simulink model for the dynamic simulation of the robotic  
suit .....153**

**Appendix C Simulink models of the cobot-HOBM coupled system in  
Chapter 5 .....155**

**List of publications .....157**



---

---

## List of Figures

---

---

Figure 1-1. Two-stage step cycle of bipedal walking gait. ....	2
Figure 1-2. Legged Walking Robot.....	3
Figure 1-3. Legged Walking Robot (Continued) .....	4
Figure 1-4. Legged Walking Robot (Continued) .....	5
Figure 1-5. A 3-D reconstruction model of “The Plantigrade Machine” .....	6
Figure 1-6. A prototype of the walking chair.....	6
Figure 1-7. A prototype of one DOF biped robot built at Cassino University.....	6
Figure 1-8. Leg mechanism of University of Maryland’s walking robot .....	7
Figure 1-9. Walking robots using Klann linkage. ....	8
Figure 1-10. “Strandbeest” .....	8
Figure 1-11. Gravity compensation by adding counterweights on links: serial (left) [46] and planar parallel (right) [47] manipulators. ....	9
Figure 1-12. KUKA R360 (left) and ABB IRB 6700 (right). ....	10
Figure 1-13. Gravity compensation by counterweights mounted on the auxiliary linkage connected with the initial system. ....	10
Figure 1-14. Gravity compensation by auxiliary actuators. ....	11
Figure 1-15. Automated movement of a gravity-compensated payload. ....	12
Figure 1-16. Walking assistive devices.....	12
Figure 1-17. Force-length characteristics of springs. ....	13
Figure 1-18. Gravity balancing by spring directly linked with the rotating link.....	14
Figure 1-19. Gravity compensation by a spring joined with a pulley and a cable. ....	15
Figure 1-20. Gravity compensation based on inversed slider-crank mechanisms. ....	16
Figure 1-21. Gravity balancer with auxiliary linkages.....	17
Figure 1-22. Upper-limb and lower-limb rehabilitation devices by using springs. ....	18

Figure 1-23. HOMBs designed by Robert A. Olsen. ....	19
Figure 1-24. HOMB in [84].....	19
Figure 1-25. HOBM «KCH-160».....	19
Figure 1-26. HOBM with pantograph actuator. ....	20
Figure 1-27. Balancing schemes with springs.....	21
Figure 1-28. HOBM with parallelogram mechanism.....	22
Figure 1-29. Some examples of HOBM applications («dalmec» Italy).....	22
Figure 1-30. Exoskeletons for walking assistance and rehabilitation. ....	24
Figure 1-31. Exoskeletons for human power augmentation.....	26
Figure 1-32. Lower-limb Exosuits. ....	27
Figure 1-33. Upper-limb Exoskeletons. ....	28
Figure 1-34. Upper-limb exoskeleton using soft material.....	29
Figure 1-35. Collaborative industrial robots. ....	31
Figure 2-1. General procedure of Genetic Algorithm. ....	38
Figure 2-2. A planar four-bar mechanism with design parameters. ....	39
Figure 2-3. Best fitness values with respect to the generation. ....	42
Figure 2-4. Trajectory generated by the optimal mechanism and design points.....	43
Figure 2-5. Change of transmission angle with respect to the input bar angle. ....	43
Figure 2-6. Leg trajectory with respect to the motion of input link. ....	44
Figure 2-7. CAD model of the walking robot. ....	44
Figure 2-8. Snapshots of the simulation when robot moving forward.....	45
Figure 2-9. Snapshots of the simulation when robot moving backward. ....	45
Figure 2-10. Displacements of the mass center of robot's moving frame along walking direction with different walking speeds. ....	46
Figure 2-11. Power consumption in different phase of gait. ....	46
Figure 2-12. The adjustable slider-crank mechanism.....	47



---

Figure 2-13. Different paths generated by the adjustable slider-crank mechanism. ...	48
Figure 2-14. Step length with respect to the slider guide position. ....	50
Figure 2-15. ADAMS model of the proposed design. ....	50
Figure 2-16. Different gaits generated by the walking robot. ....	51
Figure 2-17. Snapshots of the simulations with different configuration. ....	52
Figure 2-18. Horizontal displacement of the robot. ....	53
Figure 2-19. Energy consumption with respect to the phase of gait cycle. ....	53
Figure 2-20. Leg mechanism with two output trajectories. ....	54
Figure 2-21. Leg mechanism with a rotated input cam mechanism. ....	55
Figure 2-22. Robot's body without pantograph mechanism. ....	55
Figure 2-23. ADAMS model of the legged walking robot. ....	56
Figure 2-24. Horizontal displacement with fixed points: $B_1$ and $B_2$ . ....	57
Figure 2-25. Snapshots of simulations with different fixed points of pantograph mechanism. (walking on plane surface) ....	57
Figure 2-26. Power consumption of the actuator of the left leg when fixed point on $B_1$ and $B_2$ (walking on a plane surface) ....	58
Figure 2-27. Horizontal and vertical displacement when the fixed point on $B_1$ and $B_2$ ....	58
Figure 2-28. Snapshots of simulations with different fixed points of pantograph mechanism. (climbing stairs) ....	59
Figure 2-29. Power consumption of the actuator of the left leg when fixed point on $B_1$ and $B_2$ (climbing stairs) ....	59
Figure 3-1. Gravity compensator with a four-bar linkage. ....	63
Figure 3-2. Moment of the gravitational forces before balancing (a) and the remaining moment after balancing (b). ....	67
Figure 3-3. Gravity compensator by forming a crank-slider mechanism. ....	68
Figure 3-4. Moment of the gravitational forces before balancing (a) and the remained moment after balancing (b). ....	73

Figure 3-5. Moment of the gravitational forces before balancing (a) and the remained moment after balancing (b). .....	73
Figure 3-6. Gravity compensator based on the inverted slider crank mechanism.....	75
Figure 3-7. Active and reaction forces due to the gravitational forces of auxiliary links. ....	77
Figure 3-8. Moment produced by the gravity of the rotating link 2.....	81
Figure 3-9. Moments produced by the gravity of the rotating link 2 (a) and by the gravity of the linkage with the spring (b). ....	82
Figure 3-10. Residual moments without taking into account the masses of auxiliary links (c) and with them (d). ....	83
Figure 4-1. Rigid frame of the robotic suit.....	86
Figure 4-2. 3D model of the robotic suit. ....	88
Figure 4-3. Cable locking mechanism.....	89
Figure 4-4. Planar diagram of the distribution of anchors and attachment points while used wearing the robotic suit.....	90
Figure 4-5. Gravitational moment on the shoulder(a) and elbow(b) joint when carrying a 10kg load with different postures. ....	94
Figure 4-6. Cable tensions when carrying a 10kg load with different postures. ....	95
Figure 4-7. Force on the user’s shoulder when carrying a 10kg load with different postures.....	95
Figure 4-8. Optimization procedure. ....	97
Figure 4-9. Cable tensions when carrying a 10kg load with different postures after optimization.....	97
Figure 4-10. Force on the user’s shoulder when carrying a 10kg load with different postures after optimization. ....	98
Figure 4-11. Workspace of the propose exosuit.....	99
Figure 4-12. Block diagram of the PD controller with gravity compensation. ....	100
Figure 4-13. Comparison of the actual and desired trajectories.....	101
Figure 4-14. Cable tensions for the tested trajectories. ....	102
Figure 4-15. Mannequin test bench (a) and the added joints (b, c). ....	103

---

Figure 4-16. Cable tensions with respect to the change of forearm flexion angle (shoulder extension angle is $0^\circ$ ). .....	104
Figure 4-17. Cable tensions with respect to the change of forearm flexion angle (shoulder extension angle is $30^\circ$ ). .....	104
Figure 5-1. Lightweight cobot and HOBM cooperation for handling of heavy parts. ....	109
Figure 5-2. Workspace of the HOBM before (a) and after (b) modification for cooperating with cobot. ....	110
Figure 5-3. Frame of the usual HOBM (a) and its modified version (b) for balancer - lightweight robot cooperation. ....	110
Figure 5-4. Coupled system in which the HOBM is in the singular configuration... ..	111
Figure 5-5. Workspace of the HOBM after modification. ....	111
Figure 5-6. ADAMS model of the coupled system. ....	112
Figure 5-7. Trapezoidal trajectory .....	113
Figure 5-8. Oscillation of the proximal arm of the HOBM .....	114
Figure 5-9. Oscillation of the distal arm of the HOBM .....	114
Figure 5-10. Force applied on the cobot due to the inertia effect of the HOBM .....	115
Figure 5-11. The rigid axis connecting cobot and HOBM. ....	116
Figure 5-12. Comparison of the force applied on the cobot due to the inertia effect of the HOBM before and after the implementation of the rigid axis .....	116
Figure 5-13. Oscillations of the rotating arms of the HOBM after introducing damping moments. ....	118
Figure 5-14. Force applied on the cobot after introducing damping moments .....	118
Figure 5-15. The Denavit–Hartenberg parameterization of the cobot UR10. ....	119
Figure 5-16. Representation of the HOBM .....	123
Figure 5-17. Comparison between the ADAMS and Matlab models .....	126
Figure 5-18. Forces applied on the end effector of HOBM .....	127
Figure 5-19. Forces applied on the end effector of the cobot. ....	128
Figure 5-20. Comparison between the ADAMS and Matlab models. ....	129

Figure 5-21. Input torques of the cobot: (a) without HOBM (b) taking into account inertial forces of the HOBM..... 130

Figure 5-22. Maximum angular acceleration of the trajectory with respect to the payload mass when the HOBM and cobot are connected via a telescopic axis..... 131

Figure 5-23. Input torques of the cobot: (a) no damping moments, (b) damping coefficients are  $0.4\text{ Nms/deg}$  and (c) damping coefficients are  $0.8\text{ Nms/deg}$  ..... 133

Figure 5-24. The maximum angular acceleration of the trajectory with respect to the payload mass: (a) no damping moment and (b) damping coefficients are  $0.8\text{ Nms/deg}$  . ..... 134

Figure B-1. Simulink model of the robotic suit with PD controller ..... 153

Figure C-1. The general system of the cobot-HOBM coupled dynamic model when cobot and HOBM are linked via a telescopic axis ..... 155

Figure C-2. The general system of the cobot-HOBM coupled dynamic model after introducing frictions on the HOBM's joints..... 155

---

---

## List of Tables

---

---

Table 2-1. General Setting of the optimization .....	42
Table 2-2. Variation of adjustable parameters and step length of the leg mechanism	51
Table 2-3. Coordinates of the axes, input and output points of the pantograph mechanism.....	56
Table 4-1. Body segment parameters of an adult male. ....	93
Table 4-2. Parameters of the trajectories.....	101
Table 5-1. Parameters of the trajectories.....	113
Table 5-2. Denavit-Hartenberg parameters of UR10 .....	120
Table 5-3. Mass-inertia characteristics of UR10.....	123
Table 5-4. Mass-inertia characteristics of the HOBM .....	125
Table 5-5. Maximum torques of the motors of cobot UR10.....	131



# Chapter 1

## Introduction

---

1.1	Legged Walking Robot.....	2
1.2	Gravity Compensation in Robotics.....	8
1.3	Collaborative robotics.....	18
1.4	Outline of the thesis .....	32

---

*In the first chapter of the thesis, the critical review of the coupling systems is given. Due to the variety of the coupling system, this chapter is divided into three sections with respect to the nature of the examined problems: legged walking robots, gravity compensators used in robots and collaborative robotics.*

*It is shown that the design principles used for the development of these devices and robots can be represented as the coupling systems of different mechanical units. The optimal coupling of these units and their improved design can significantly enhance the performance of robots.*

*The known solutions are summarized through the suggested critical review and some of their drawbacks are disclosed.*

## 1.1 Legged Walking Robot

Since the term “robot” was firstly used by the Czech writer Karel Čapek in his fictional play “R.U.R” in 1920 [1], the robot industry has been through a prosperous development in the past fifty years. As its initial object in the play, a robot is designed as a machine to take place of humans for doing the jobs which are dangerous or physically intensive.

As an important part of robot family, legged robots more versatile than track or wheeled robots when they work in unconventional environments including rough terrains and steep stairs. However, achieving such versatility require increased complexity and power consumption.

The typical walking consists of a repeated gait cycle. The cycle itself contains two phases: the propelling phase and the non-propelling phase. Figure 1-1 shows a classic two-stage cycle of bipedal walking gait where the thicker line represents the supporting leg (right leg) in propelling (stand) phase and the thin line represents the swing leg (left leg) in non-propelling (swing) phase. While in stand phase, the leg is in contact with the ground and generating a propelling force to push the body moving forward. And while in swing phase, the leg is leaving the ground and swinging from back to forth, the foot trajectory is a curved line.

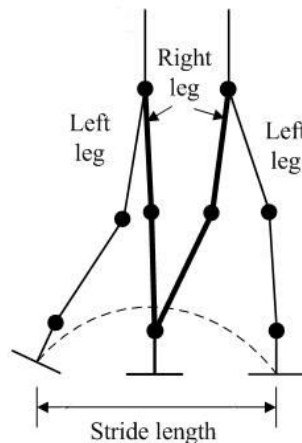


**Figure 1-1.** Two-stage step cycle of bipedal walking gait.

In this section, a review of the development of legged walking robots since the born of the first humanoid legged walking robot WABOT 1 is presented.

### 1.1.1 Multi-degree-of-freedom legged walking robots

The pioneering works in the field of legged robots were started in Japan around 1970. Ichiro Kato and his team at Waseda University designed two bipedal walking robots WL-1 and WL-3 based on a human leg mechanism in 1967 and 1969 respectively [2]. WL-3 (Figure 1-2a) has an electro-hydraulic servomotor and performed humanoid walking locomotion in the swing phase and stance phase using a master-slave control method. While in 1973, they created the world’s first full-scale anthropomorphic legged robot – WABOT-1 (Figure 1-2b) [3]. WABOT-1 has disproportionately large feet to



maintain its balance. It was hydraulically powered and controlled by a minicomputer and experiment showed that it was able to realize a few slow steps in static equilibrium. Followed by the way paved by Kato, researchers from Waseda University have developed several generations of WL and WABIAN family walking robots where the latest generation named WABIAN-2 (Figure 1-2c) [4], [5]. WABIAN-2 is 1.53m tall and 64.5kg weight, it has 41 DOFs and the joints designed for bio-mimicking the actual human's one. Experiments showed that it can walk steadily with the speed of 1.8km/h.

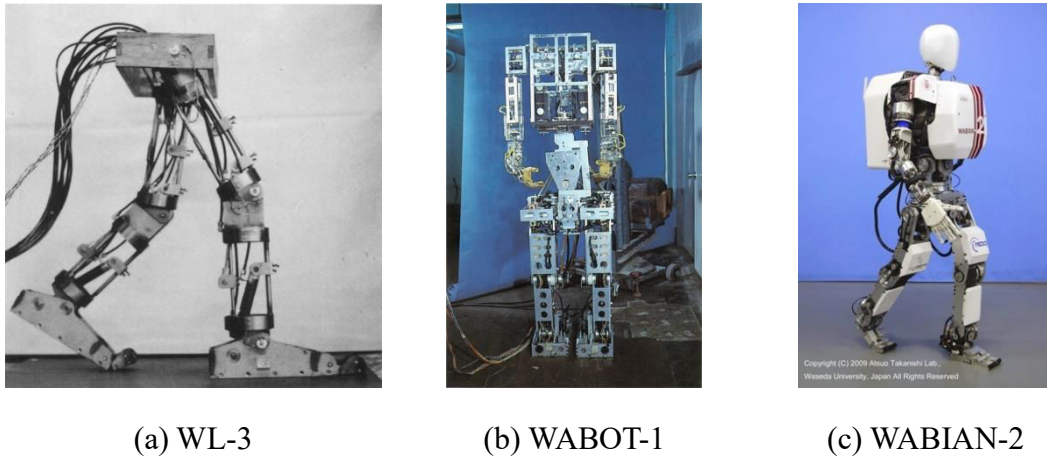
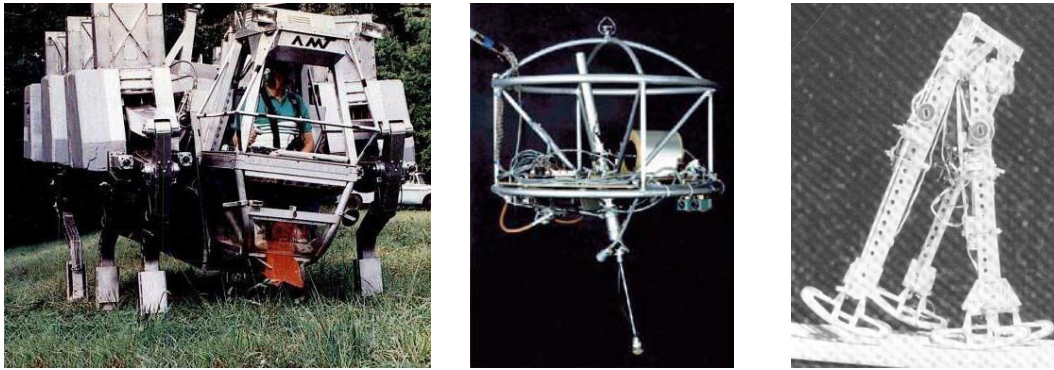


**Figure 1-2.** Legged Walking Robot

In the same period with Kato, in Europe, M. Vukobratovic and his team from the Mihailo Puppin Institute, Belgrade, Yugoslavia were very involved in the problems generated by functional rehabilitation. They designed the first active exoskeletons, and several other devices such as the Belgrade's hand [6], [7]. But the most well-known outcome remains their analysis of locomotion stability, which exhibited around 1972 the concept of zero-moment point (ZMP), widely used since that time [8]. This was the first attempt to formalize the need for dynamical stability of legged robots; the idea was to use the dynamic wrench in order to extend a classical criterion of static balance (the center of mass should project inside the convex hull of contact points).

In the next decade, the breakthroughs came from the United States. Robert McGhee and Kenneth Waldron achieved the design of the world's largest hexapod which is a man-driven quasi-industrial system able to walk on natural irregular terrain called adaptive suspension vehicle (Figure 1-3d) [9]. The vehicle uses a parallelogram mechanism and two jack actuators for each of its legs. Simultaneously, Marc Raibert started to study dynamically stable running at Carnegie Mellon University. Then, he launched the Massachusetts Institute of Technology LegLab, where he and his teammates designed a 3D one-leg hopper (Figure 1-3e) which can be actively balanced in dynamic locomotion with simple control algorithms [10]. After the one-leg prototype, they also designed a sequence of biped and quadruped versions where the biped hopping machine could even perform a flip [11]–[13].



(d) Adaptive suspension vehicle (e) 3D one-leg hopper (f) Passive biped robot

**Figure 1-3.** Legged Walking Robot (Continued)

In the 1990s, Tad McGeer pioneered the field of passive walking robots by proposing the idea of studying purely passive mechanical systems (Figure 1-3f). He has shown that there exists a class of two-legged machines for which walking is a natural dynamic mode: once started on a shallow slope, such a machine will settle into a steady gait quite comparable to human walking, without active control or energy input [14]. His work led the way of designing a walking robot by adding a minimum set of actuators to a passive system in order to just compensate for the loss of energy when the system is on flat ground. Because of the energy efficiency of this kind of design, several researchers have followed the tracks open by Tad McGeer [15], [16].

The end of the millennium was a period of intense technological activities. Industrial breakthroughs showed to the world that building true humanoids was now possible. Several international industrial enterprises started to conduct research in the field of humanoid walking robots. In Japan, Honda designed one of the world's famous humanoid robots - ASIMO (Figure 1-4g) and it was firstly unveiled in 2000 [17], [18]. ASIMO has 34 DOFs and it is the first humanoid robot capable walking and running autonomously with the maximum speed of 2.7km/h at walking and 9km/h at running for the latest version. Similarly, Kawada also designed a series of biped robot and the latest version – HRP-4 (Figure 1-4h) can even accomplish some complicated tasks like dancing and pouring drinks [19], [20]. In recent years, an American robot company, Boston Dynamic, has designed several biped and quadruped robots with great breakthroughs [21]. Its biped robot, Atlas (Figure 1-4i), has an impressive dynamic balancing ability and it can even perform some acrobatic movements like the backward somersault.



(g) ASIMO



(h) HRP-4



(i) Atlas

**Figure 1-4.** Legged Walking Robot (Continued)

### 1.1.2 Reduced-degree-of-freedom walking robots

To create biped robots walking like a human is necessary to use a large number of actuators. Therefore, these robots are automorphic and flexible. However, there are several drawbacks: complexities of the design and the control system, low energy efficiency due to the masses of motors, as well as an overly high price complicating practical use.

To make a biped robot more attractive, a different methodology can be considered such as constructing a biped robot with reduced number of degrees of freedom. One of the effective ways to design a walking robot with reduced DOFs is to use leg mechanisms which is an assembly of links and joints intended to simulate the walking gait of humans or animals.

Russian mathematician Pafnuty Chebyshev suggested the very first walking machine by using a four-bar mechanism which converts rotational motion to approximate straight-line motion with approximate constant velocity (as known as Chebyshev Linkage). A quadruped prototype of this machine named “The Plantigrade Machine” (Figure 1-5 shows a 3-D reconstruction model) was first shown in Paris on the Exposition Universelle in 1878 [22]. Inspired by the work of Chebyshev, several designs of single DOF walking robot based on Chebyshev linkage have been achieved. Funabashi et al. from the Tokyo Institute of Technology designed a human-driven walking chair where its leg mechanism is a Chebyshev linkage jointed with a pantograph mechanism (Figure 1-6) [23]. The fixed point of the pantograph mechanism can change both vertically and horizontally which gives the possibility to deal with different terrains. Another unique feature of this walking chair is that it has a hybrid actuation system including two assisting actuators for reducing the effects of variations in user’s driving velocity [24]. Similarly, Marco Ceccarelli and his team at the Laboratory of Robotics and Mechatronics in Cassino University have proposed various solutions for Low-Cost Easy-Operation leg design where the Chebichev four-bar linkage has been successively used for generating a foot trajectory (Figure 1-7) [25], [26]. In order to amplify the produced motion of the Chebyshev linkage, a pantograph mechanism has been applied.

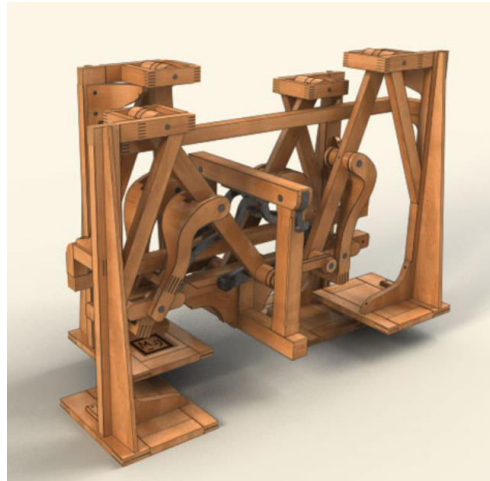


**Figure 1-5.** A 3-D reconstruction model of “The Plantigrade Machine”.

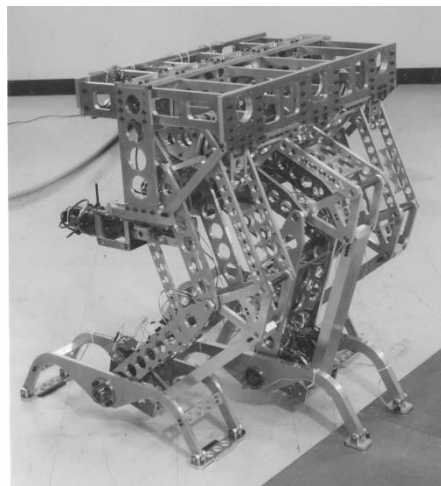


**Figure 1-6.** A prototype of the walking chair.

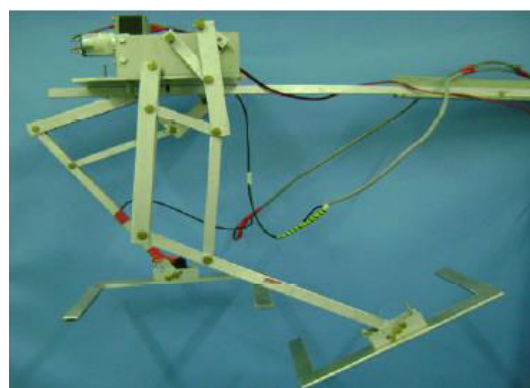


**Figure 1-7.** A prototype of one DOF biped robot built at Cassino University.

Researchers from the University of Maryland has designed a walking mechanism by using a modified four-bar mechanism and a pantograph mechanism (Figure 1-8) [27]. A unique feature of this mechanism is that it contains a leg lift mechanism which can change the position of the fixed point of pantograph mechanism. Hence, this lift mechanism is capable of changing the leg height as well as the stride length. And a few

years later, they designed a six-link leg mechanism which is essentially a four-bar linkage with an embedded skew pantograph [28]. This mechanism can generate a  $\Delta$ -shaped gait with sufficient height for the walking machine to step over obstacles or to climb stairs. With the embedded pantograph design, the mechanism size can be slender and compact.

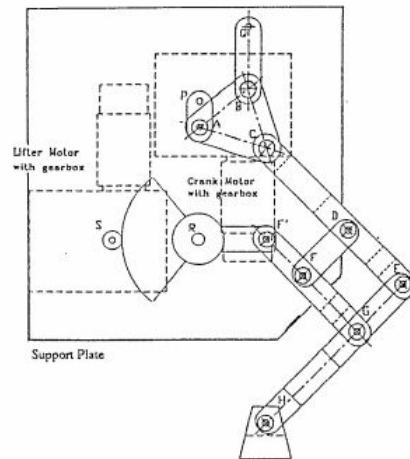


**Figure 1-8.** Leg mechanism of University of Maryland's walking robot

Except for the four-bar linkage, other linkages have been also used for the design of the single-DOF walking robot. Simionescu and Tempea designed an eight-bar leg mechanism based on Watt II linkage [29]. An RRR dyad was articulated for amplifying the output path. The Klann linkage is another famous leg mechanism designed by Joseph Klann [30], [31]. It has six links including the frame, a crank, two grounded rockers, and two couplers connected by pivot joints. Klann linkage is categorized as a modified Stephenson III kinematic chain and the proportions of each its links are defined to optimize the linearity of the foot for one-half of the rotation of the crank. Several legged walking robots have been designed based on Klann linkage (Figure 1-9) [32]–[34].

Dutch artist Theo Jansen designed a planar single-DOF leg mechanism for his kinetic sculptures “Strandbeest” where he intended to build large mechanisms which are able to move on their own (Figure 1-10) [35]. Jansen's leg mechanism has 12 links including a crank which is the input of the mechanism and a fixed link which is part of the chassis of the legged system. Several researchers have conducted studies on the kinetic and dynamic of Jansen's mechanism and some new walking robots have been designed [36]–[39].



(a) The Walking Beast



(b) An underwater walking robot

**Figure 1-9.** Walking robots using Klann linkage.



**Figure 1-10.** “Strandbeest”

## 1.2 Gravity Compensation in Robotics

While the industrialization spreading throughout the world from the 19<sup>th</sup> century, robots have been a crucial part in manufacture because of their efficiency, high precision and not being restricted by the environment. Since the first commercial industrial robot was brought out by George Devol in 1954 [40], the industry of robot has drastically prospered through the past decades.

The performance of a robotic system is often related to the capacity of the actuator. The dynamic equation of the robotic system is [41]:

$$\boldsymbol{\tau} = [ \underbrace{\mathbf{I}(\boldsymbol{\theta})\ddot{\boldsymbol{\theta}}}_{\text{Inertial moment}} + \underbrace{\mathbf{f}(\boldsymbol{\theta}, \dot{\boldsymbol{\theta}})}_{\text{Coriolis and centripetal moment}} + \underbrace{\mathbf{G}(\boldsymbol{\theta})}_{\text{Gravitational moment}} ] \quad (1-1)$$

where  $\boldsymbol{\tau}$  is the vector of actuator torques,  $\mathbf{I}$  the inertia tensor of the robotic system and the inertial moment on each joint is the inertia tensor times the joint acceleration  $\ddot{\boldsymbol{\theta}}$ ,  $\mathbf{f}$  is the Coriolis and centripetal moment which is a non-linear function of joint position  $\boldsymbol{\theta}$  and joint velocity  $\dot{\boldsymbol{\theta}}$  and  $\mathbf{G}$  is the gravitational moment which is a function of  $\boldsymbol{\theta}$ .

It can be seen that for a robotic system operated with relatively low speed and low acceleration, a large part of the actuator’s torques are used to compensation

gravitational effect. And since many robotic systems are operated at low speed to ensure the different tasks, gravity compensation would be very beneficial by which a robotic system can be operated with relatively small actuators generating less torque.

A robotic system is statically balanced if its potential energy is constant for all possible configurations. In this condition, robotic systems work similarly in a zero-gravity environment which means that nearly zero actuator forces are required when the mechanism is in slow motion. The static balancing of rotating links, which are often elements of serial or parallel manipulators, is well known. Different approaches and solutions devoted to this problem have been developed and documented [42], [43]. The nature of the compensation force used for balancing of rotation links may be various:

- The gravitational force of a counterweight arranged on the opposite side of the rotating link or via an auxiliary linkage;
- Forces generated by auxiliary actuators;
- The elastic force of a spring jointed directly with links or via an auxiliary mechanism, which can be a cable and pulley arrangement, a linkage, a cam mechanism or a gear train.

### 1.2.1 Gravity compensation by counterweights

The using of counterweights is one of the classical ways for eliminating gravitational effect in mechanical systems [44], [45]. The application approach is adding counterweights on the rotating links in order to make the total center of mass at a fixed point.

Comparing with the spatial manipulator, gravity compensation by counterweights mounted on the links is more appropriate for serial and planar parallel manipulators (Figure 1-11).

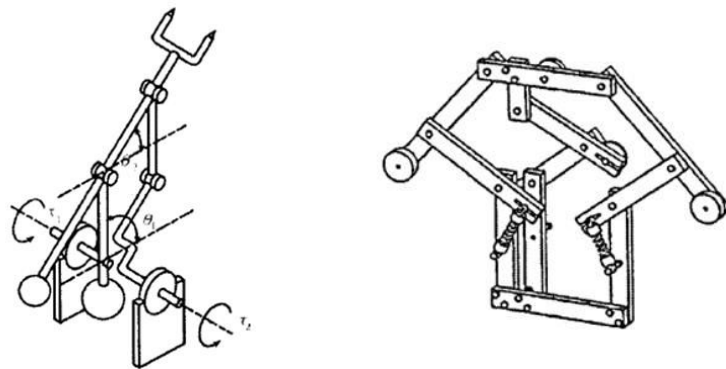


**Figure 1-11.** Gravity compensation by adding counterweights on links: serial (left) [46] and planar parallel (right) [47] manipulators.

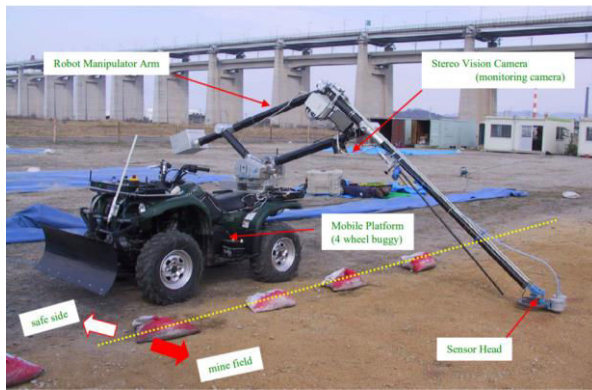
It is obvious that by directly adding the supplementary mass as a counterweight on the robot is not desirable since it leads to the increase of the total mass and the overall size of the robot. Therefore, in many industrial robots, for example, KUKA R360 and ABB IRB 6700 (Figure 1-12), the masses of the motors are often used for gravity compensation [48].



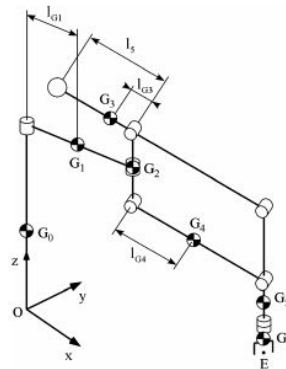
**Figure 1-12.** KUKA R360 (left) and ABB IRB 6700 (right).

Except for joining counterweight directly with the initial system, another way of gravity compensation by counterweights is to connect counterweights with original structure via auxiliary linkages. The goal of these linkages is to improve the compensation and design conditions via optimizing the location of balancing elements.

Fukushima et al. designed a mine detection vehicle where a weight balanced manipulator was installed (Figure 1-13a). A counterweight was linked with the manipulator via pantograph mechanism [49]. It has been shown that the robot arm with properly dimensioned balancing counterweights can be efficiently actuated with very low power and energy consumption. Similarly, Bruzzone and Bozzini studied the balancing of the SCARA robot by means of a counterweight via auxiliary linkages (Figure 1-13b) or a spring. The obtained simulation results showed that for low-speed motions the counterweight balancing is more efficient, while for high-speed motions the elastic balancing is advantageous [50].



(a) Mine detection vehicle with weight balanced arm



(b) Gravity compensation of a SCARA robot

**Figure 1-13.** Gravity compensation by counterweights mounted on the auxiliary linkage connected with the initial system.

Although many studies illustrate the promising results of gravity balancing of parallel manipulators comprising auxiliary systems equipped with counterweights. However, in reality, such a method often becomes complicated for application because of the limitation of the overall size of manipulators and the possibility of collision of extended moving links carrying counterweights.



### 1.2.2 Gravity compensation by auxiliary actuators

Because of the limitation of gravity compensation by counterweights, in some designs, pneumatic, hydraulic or electromagnetic actuators are used for the gravity balancing of serial manipulator [51] or parallel robots [52] (Figure 1-14).

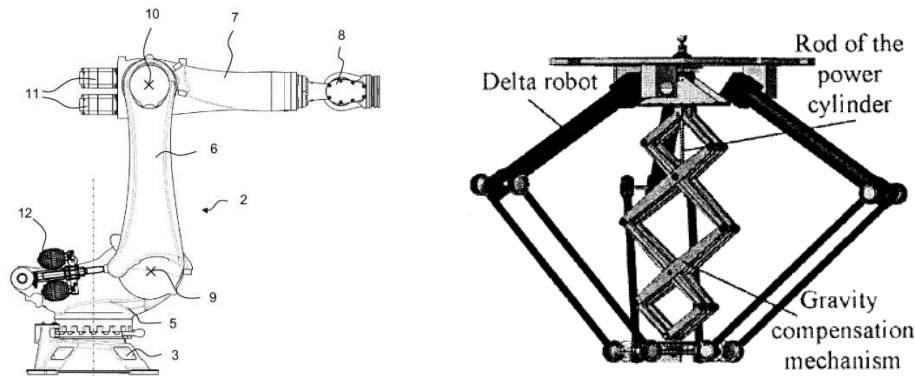


**Figure 1-14.** Gravity compensation by auxiliary actuators.

Lacasse et al. from the University of Laval developed a gravity compensation system for a 7-DOF robotic manipulator using remote counterweights connected to the robot via a hydraulic transmission [53], [54]. The experiment showed that the built prototype of the 7-DOF robot is able to adapt its balancing counterweights to a payload of up to 10 kg, which was a maximal payload for the tested prototype.

It should be noticed that in comparison with the gravity compensation of planar manipulators, the gravity compensation of spatial architectures is more complicated because it can be achieved either by an unavoidable increase of the total mass of moving links or by a considerably complicated design of the initial mechanism. One of the promising approaches is to combine auxiliary linkages with actuators.

Baradat et al. proposed a gravity balancing mechanism for the Delta robot which combines a multi-loop pantograph linkage with actuator. The active force of the actuator generates a vertical force applied to the platform via added linkages [52], [55].

Unlike the previous designs whose object is to eliminate the gravitational effect of the original systems, for the robotic manipulators, another approach is to eliminate the gravitational effect of the payload which is significant when manipulating heavy loads. A method for the automated movement of a gravity-compensated payload and an automated handling system for gravity compensation of the payload were presented by Brudniok et al. (Figure 1-15) [56]. It involves supporting a payload by a holding unit that is connected with an end-effector flange of the robot for automatically moving of the load body. Similar studies were successfully carried out in [57], [58].

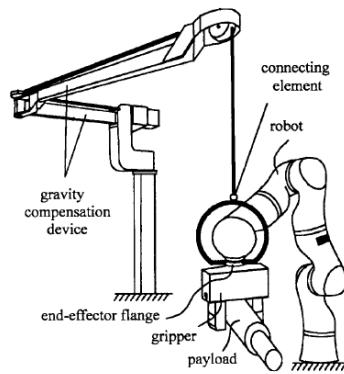
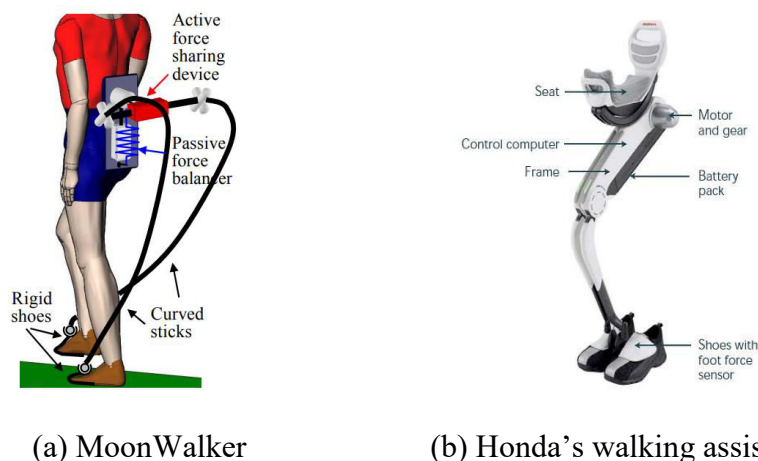


**Figure 1-15.** Automated movement of a gravity-compensated payload.

Another promising application of gravity balancing by using actuators is walking assist devices and rehabilitation exoskeleton. In therapeutic situations, therapists often apply full or partial support to a paretic limb to help reduce the effect of gravity on the patient's motion. For the patients whose muscles are weak or lacks normal neuromuscular control due to a neurological disease like stroke, it is extremely difficult to do during walking, where the weight of the leg may create problems [59].

MoonWalker (Figure 1-16a) is a lower limb exoskeleton [60], which is able to sustain part of a user's body weight. This system can be used for rehabilitation, to help people having weak legs, or to help those suffering from a broken leg to walk. The main characteristic of MoonWalker is that a passive force balancer provides the force to sustain bodyweight. It is controlled using an actuator that requires very low energy to work on flat terrains, as it is used only to shift that force the same side as the leg in stance. That motor is able also to provide a part of the energy to climb stairs or slopes. The authors believe that this approach can help to improve the energetic autonomy of lower limb exoskeletons.



(a) MoonWalker

(b) Honda's walking assist device

**Figure 1-16.** Walking assistive devices.

Honda's walking assist device (Figure 1-16b) [61] helps support bodyweight to reduce the load on the user's legs while walking. This could lead to reduced fatigue and less physical exertion. Honda's device lightens the load on the user's legs and helps maintain a center of gravity via special mechanisms developed by the company. There are plenty

of use cases for this product helping people afflicted with mobility issues or leg problems. It can also be used for rehabilitation.

### 1.2.3 Gravity compensation by springs and auxiliary mechanisms

As was mentioned above, for an equilibrium system, its total potential energy stays constant at any of its configurations. The spring as an element which has the property of storing and releasing energy is often used for gravity balancing. For a robotic system balanced with springs, the gravitational potential energy of the robot system and the elastic potential energy of the spring transfer between each other, hence the total potential energy can stay as a constant.

Before introducing gravity balancing mechanisms by spring, let us firstly disclose the differences of two types of springs which are used for gravity compensation in robotic systems: zero-free length and non-zero-free length springs.

Zero-free length spring is a term for a specially designed coil spring that would exert zero force if it had zero length. Whereas for the non-zero-free length spring, zero force will be exerted at its non-zero initial length.

Obviously, a coil spring cannot contract to zero length because at some point the coils will touch each other and the spring will not be able to shorten any more. Zero-length springs are made by manufacturing a coil spring with built-in tension, so if it could contract further, the equilibrium point of the spring, the point at which its restoring force is zero, occurs at a length of zero [62]. The force-length characteristics of springs of these two types of springs are shown in Figure 1-17.

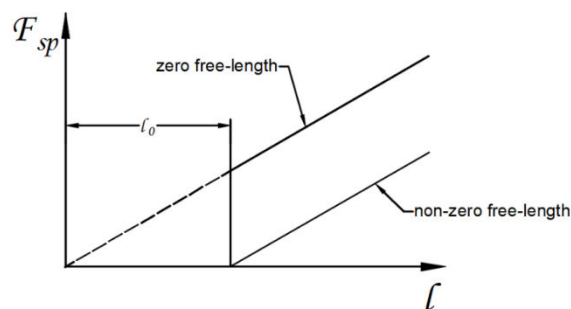


**Figure 1-17.** Force-length characteristics of springs.

In order to better understand the difference between the gravity compensation by zero-free and non-zero-free length springs, let us consider the gravity compensation of a rotating link by directly linking a spring.

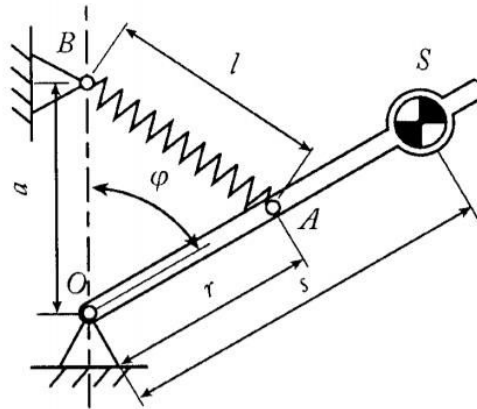


**Figure 1-18.** Gravity balancing by spring directly linked with the rotating link.

For the system shown in Figure 1-18, the system will be fully balanced if the moment of the gravitational forces equals to the moment of the elastic force of the spring, i.e.

$$mgs \sin \varphi = (F_{sp} ar / l) \sin \varphi \quad (1-2)$$

where  $m$  is the mass of the rotating link,  $s = l_{os}$  is the distance of gravity center  $S$  from axis  $O$ ,  $\varphi$  is the angle between the vertical axis and the link axis,  $F_{sp} = F_0 + k(l - l_0)$  is the elastic force of the spring,  $F_0$  is the initial force of the spring (the initial force is the internal force that holds the coils tightly together),  $k$  is the stiffness coefficient of the spring,  $l_0$  is the initial length of the spring,  $a = l_{OB}$  is the distance of point  $B$  from axis  $O$ ,  $r = l_{OA}$  is the distance of point  $A$  from axis  $O$  and  $l = l_{AB}$  is the length of the spring at current angle  $\varphi$ .

It can be seen from Equation (1-2) that a fully gravity compensation can be achieved when  $F_0 = kl_0$ , i.e. when a zero free length spring is used. In the case of a non-zero-free length springs with  $F_0 = 0$  or  $F_0 \neq kl_0$ , only partial gravity compensation of a rotating link can be achieved.

However, zero-free-length springs are often applied in theoretical solutions, but they are very rare in real robotic structures. Therefore, the use of conventional linear springs for gravity compensation often considered with auxiliary mechanisms. The additional parameters of the auxiliary mechanisms can be used for optimizing gravity compensation efficiency.

A simple scheme of gravity compensation by a spring and an auxiliary mechanism is shown in Figure 1-19. The adding of the cable and pulley allows full compensation of gravity by using non-zero-free length spring. The condition of the gravity compensation of the rotating link can be rewritten as:

$$mgs \sin \varphi = F_{sp} h \quad (1-3)$$

where  $h = (ar/l_{AB}) \sin \varphi$ . Thus, Expression (1-3) is similar to (1-2) when the length  $l$  of the spring is equal to  $l_{AB}$ . However, in this case, thanks to the cable, it is possible to

consider that  $l_{AB} = l - l_0$ , which leads to the condition  $mgs = kar$ , with  $F_0 = 0$ . So, the rotating link can be balanced with non-zero-free length spring.

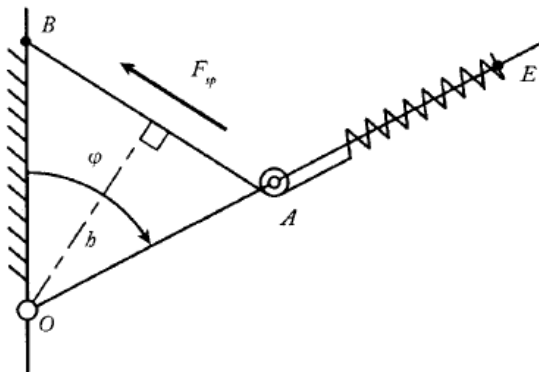


**Figure 1-19.** Gravity compensation by a spring joined with a pulley and a cable.

Apart from using the conventional round pulley, Endo et al. designed a gravity compensation mechanism with non-circular pulleys and springs. After the preliminary verification of the design methodology for a single pendulum system, the authors extend the compensation mechanism to four-bar and five-bar linkage arms. It has been shown that the introduction of the weight compensation mechanism reduces the maximum static torque up to 50-80% [63].

Although theoretically, the method of joining springs with pulley-cable mechanism is an effective approach for gravity compensation, several error sources in the practical implementations decrease the actual efficiency [64]. The condition of maximum elongation of the spring that should be not more than 25% of its initial length leads to the design concept, in which the spring must often be installed along the rotating arm and the number of pulleys should be at least two. Considering the diameter of the cable with protection, the diameter of the pulley turns out to be relatively large, which leads to a perturbation of the theoretical conditions of the balancing. Furthermore, the frictional forces between the pulley and the cable are also not low. All these factors lead to an unbalanced moment of more than 10-15% of the moment of gravitational forces.

Except for cable-pulley arrangement, gravity balancing systems with non-zero-free length spring are often considered with auxiliary linkages as well.

Figure 1-20 shows two gravity equilibrators based on inversed slider-crank mechanisms [65], [66]. In the left system, rotating link 1 is connected with coulisse 2 and slider 3. The elastic force generated by the compression spring 4 is proportional to  $\sin(\varphi/2)$  which let the whole system fully balanced. And in the right design, the lengths of links of the mechanism must satisfy to the condition  $l_{OA} = l_{OB}$  leading to the displacement of the spring proportional to  $\sin(\varphi/2)$ , which ensure the complete gravity compensation of the rotating link 1.

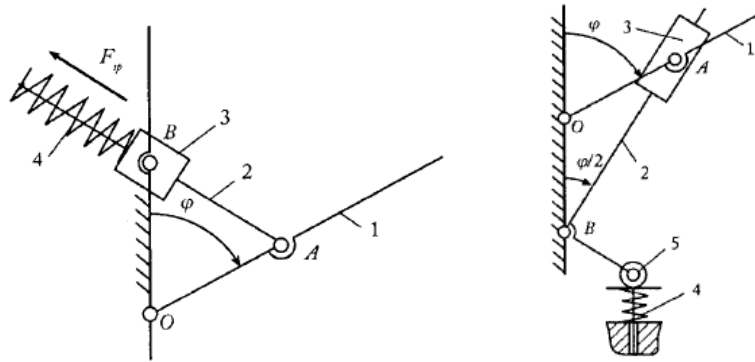


**Figure 1-20.** Gravity compensation based on inversed slider-crank mechanisms.

Several of the other design concepts carried out by adding auxiliary linkages are shown in Figure 1-21 [67]–[71]. In these designs, the geometrical dimensions of the auxiliary linkages, i.e. the lengths of the links, are functioned as adjustable parameters. While changing these parameters, the relationship between the rotational angle of the balanced link and the length of the spring will be changed as well. Numerical minimization methods are used for obtaining optimal parameters.

Gravity compensation with springs can be also applied for upper-limb or lower-limb rehabilitation. Unlike the rehabilitation devices driven by motors, for the designs with springs, no external active force (or low active force for hybrid designs) is needed. Hence, these designs will not be affected by the size of the motors or battery duration etc.

Figure 1-22 shows two rehabilitation devices by using springs for upper limb and lower limb respectively [72], [73]. For the upper-limb design, a parallelogram linkage joined with two springs was used for the gravity compensation of the whole arm. While for the lower-limb design, a hybrid method was employed where the center of mass of the leg is geometrically located using a parallelogram mechanism and then the springs are placed at suitable positions in order to fully compensate the effect of gravity over the range of motion. A hybrid design was also proposed where a motor was added for compensating the errors caused by friction [74].

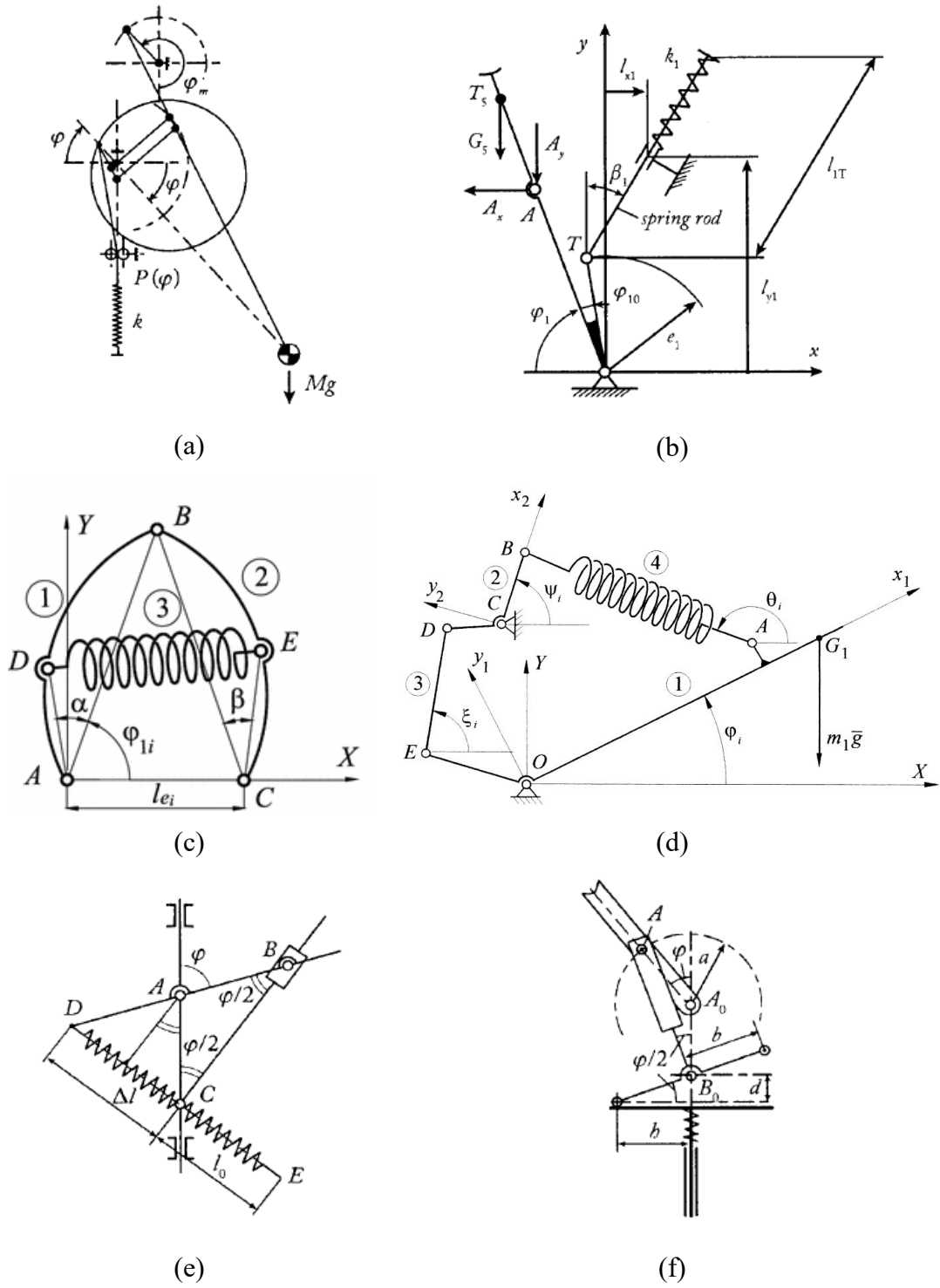
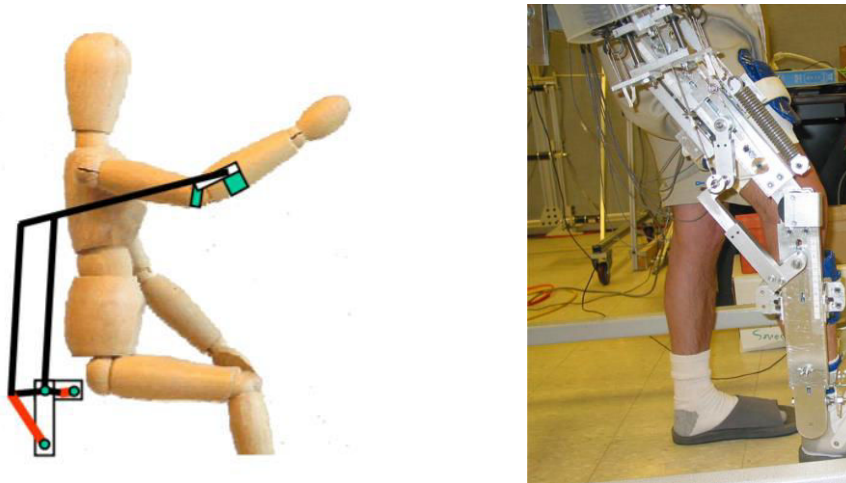


Figure 1-21. Gravity balancer with auxiliary linkages.



**Figure 1-22.** Upper-limb and lower-limb rehabilitation devices by using springs.

In several designs, cam mechanism joint with linear springs were used for gravity balanced where the optimal profiles of cams were found in order to compensate the gravity of links or a payload [41], [75]. In addition, for some multi-DOF manipulators, gear trains like bevel gears were used for the gravity compensation of each link of the manipulators [76], [77].

### ***1.3 Collaborative robotics***

In the past decades, our society benefits a lot from the booming development of the robotic industry. With the automatic systems and pre-programmed settings, robots can accomplish plenty of tasks more efficiently, and the physical burdens of human have also been relieved.

However, up to now, there are still some tasks which cannot be fully automatized (due to the complexity of the task or the unpredictability of the workspace) or need the involvement of human. But for these tasks, robots can still be beneficial while working with human and sharing the same workspace and we call these robots - collaborative robots or cobots (the portmanteau of collaborative robots). Cobots were invented in 1996 by Colgate and Peshkin, professors at Northwestern University. A 1997 US patent filing describes cobot as "an apparatus and method for direct physical interaction between a person and a general purpose manipulator controlled by a computer" [78]. Despite its very specific initial meaning, the word cobot now often refers to the robot having direct interaction with the human within a shared workspace. Cobots provide a variety of benefits such as weight compensation, inertia masking, strength amplification, and guidance via virtual surfaces and paths [79].

In this section, a brief review of three kinds of widely-used cobots: hand-operated balanced manipulators, wearable robotic devices and collaborative industrial robots is proposed.

#### **1.3.1 Hand-operated balanced manipulator (HOBM)**

The creation of a new class of mechanical systems called manual balanced manipulators (HOBM) was a logical stage in the field of the improvement of the means for the



mechanization of production. HOBM is a handling system with a simple mechanical actuator in which the manipulated object in any position of the workspace is balanced. Such a state of constant balance allows displacements of heavy objects manually. HOBMs are used in such conditions as when the application of hoisting machinery is not efficient and automation by using industrial robots is expensive and consequently unjustified. [80]

The creation and industrial application of HOBM began in 1964 when Robert A. Olsen suggested a new original balanced assembly [81], [82] (Figure 1-23). This invention was the basis for the development of the manual balanced manipulator proposed by Reizou Matsumoto in 1975 (Figure 1-24) which is the prototype of the modern HOBM [83] (Figure 1-24).

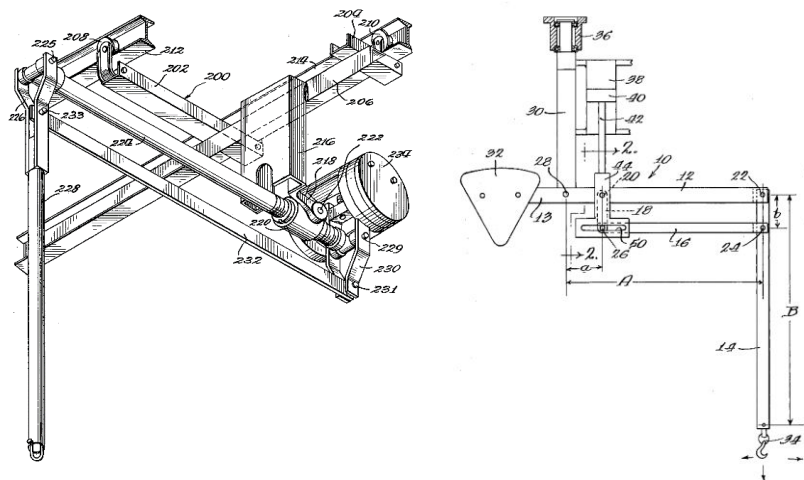


Figure 1-23. HOBMs designed by Robert A. Olsen.

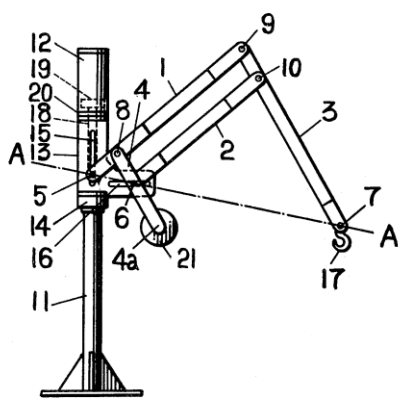


Figure 1-24. HOMB in [84].

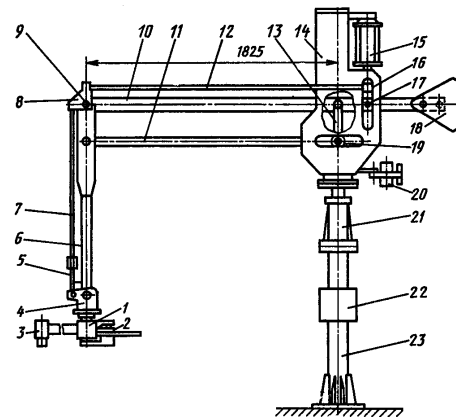
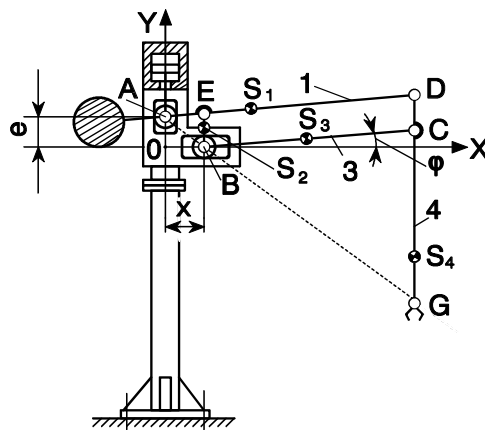


Figure 1-25. HOBM «KCH-160».

In the suggested solution of Reizou Matsumoto, the following property of the pantograph is used: if three points (see Figure 1-24: points 5, 6 and 7) of the pantograph lie on the same straight line A-A, then any path traced by point 5 is reproduced by point 7 (for fixed point 6) and any path traced by point 6 is reproduced by point 7 (for fixed point 5). Thus, if points 5 and 6 are located in the vertical and horizontal guides, the displacement of point 7 in the horizontal plane may be realized by the horizontal

displacement of point 6 combined with the rotation of the system about the vertical axis (for fixed point 5). In a similar manner, the vertical displacement of point 7 may be realized by the vertical displacement of point 5 (for fixed point 6). The interesting characteristic of such a system is the following: if the pantograph system is balanced about axis through point 5, the displacements of the manipulated object in the horizontal plane may be realized without effort (the only resistance being due to friction in the joints) because the gravitational forces are always perpendicular to the displacements. Thus, the displacements in the horizontal plane may be realized manually. For the vertical displacement, a suitable driver may be used, which can balance the weight of the manipulated object or produce the vertical displacement directly.

The pantograph applications are often used in the HOBMs since they allow the transformation of the small displacements into the large displacements. For example, in Figure 1-26, the small displacements of the points A and B lead to a large displacement at the end effector G, which gives a large working space to the manipulator.



**Figure 1-26.** HOBM with pantograph actuator.

The term "balanced manipulator" shows that, for the HOBMs, in the operating procedure of these systems, it is very important to achieve an accurate mass balancing. The general approach for determination of balancing conditions was proposed by the study of the motion of the center of mass of the pantograph actuator.

It should be noticed that the basic function of a HOBM is that operators can move the manipulated object horizontally, overcoming only the forces of friction, the total work done by the forces of gravity of the elements of the actuator must be equal to zero. For this purpose, the center of mass of the pantograph mechanism must only move in the horizontal direction (or must be fixed).

Which are the advantages of these manipulators relative to industrial robots? Primarily it is the simplicity of their construction and the low-cost price. They have a very simple command system, a great weight-carrying capacity (up to 2500 kg) and a very large workspace (in the horizontal direction the gripper can reach to approximately 3000mm). This allows the HOBM to be used for moving workpieces between machine tools very smoothly because it is controlled manually. The implantation of HOBM in existing production is very simple without the need for important additional surfaces, special auxiliary devices or essential reorganization of the production layout.

It is obvious that the balancing condition achieved by a counterweight leads to a significant augmentation of the inertia of the whole system which increases the effort for manipulation. Therefore, instead of using a counterweight, there are also balancing schemes based on the application of springs (Figure 1-27). [83], [85]–[87]

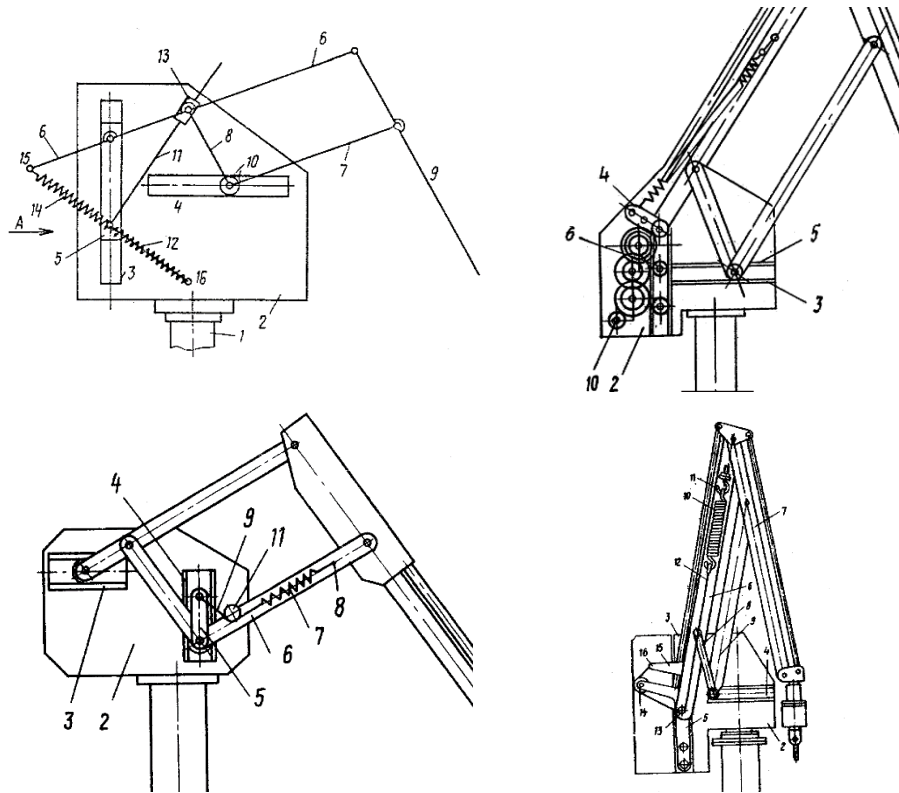


**Figure 1-27.** Balancing schemes with springs.

It should be noticed that, during the usage of HOBM, most of the works are used to overcome the frictional forces. Therefore, how to diminish friction is one of the essential parts in the design process of a HOBM. Practical applications show that the operation of the manual balanced manipulator is easier when the mechanical actuator contains only revolute pairs. In this case, the frictional forces are low and, consequently, the manual effort exerted by the operator is less. Figure 1-28 shows a version of a manual balanced manipulator with only revolute pairs [88], [89]. It can be seen that, in these designs, pneumatic/hydraulic actuators were used.

The design of the drive system in manual balanced manipulators also determines the construction of the manipulator, its functional capacity, as well as its reliability and speed. In industry, one can find manipulators with electric, pneumatic and hydraulic drives. For manipulators having up to 150 kg load capacity, one uses electric motors or pneumatic drives; if the load capacity is up to 500 kg one uses electric motors. With regard to manipulators with very great load capacity (up to 2500 kg), essentially one uses hydraulic drives.

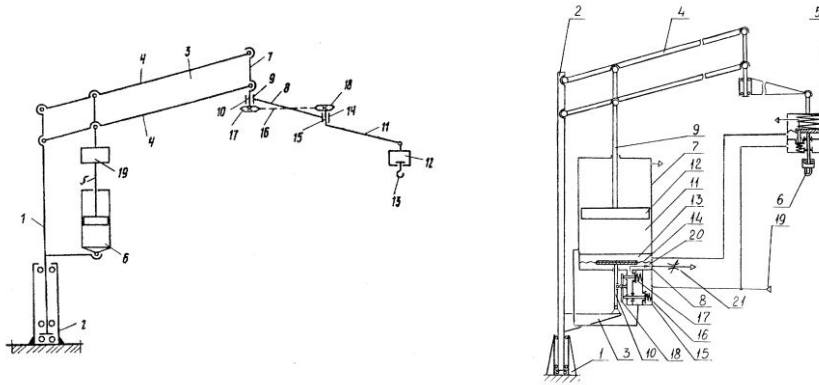


**Figure 1-28.** HOBM with parallelogram mechanism.



**Figure 1-29.** Some examples of HOBM applications («dalmec» Italy).

The applicability of HOBM in the different fields is very wide, including: loading and unloading of machine tools, presses and other production equipment; displacement of heavy objects during machine assembly; movement of foundry ladles; handling of heavy objects as, for example electric motors, various devices, etc.; as well as handling of objects during storage. Figure 1-29 represents some examples of their application.

### 1.3.2 Wearable robotic devices for power assistance and rehabilitation

The wearable robotic devices, also known as exoskeleton, have strong advantages given their unique features such as their outstanding physical performance, exceeding that of humans, and their mobility. As a result, attempts to adopt these devices in the rehabilitation and the industrial field provide a huge benefit for their users [90].

Assistive robots have applications in the industrial field as well as for patients and the elderly with mobility impairments. They free people from much labor and the burdens of many kinds of manual work. There have been many approaches to the reduction of labor that do not only fully assist but also partly aid workers, such as in the use of extremely heavy payload-oriented construction equipment, which is manipulated by humans. Manual or semi-automatic machine tools are mostly used in contemporary industries. In particular, without manpower, especially without the manipulability and mobility of human limbs, full automation will be incompatible with today's technologies.

According to which part of the user's body is assisted, the exoskeletons can be divided into two classes: lower-limb designs and upper-limb designs.

#### *(a) Lower-limb designs*

Locomotor disability is the most commonly reported type of disability. It is defined as a person's inability to execute distinctive activities associated with moving both himself and objects, from place to place and such inability resulting from the affliction of the musculoskeletal and/or nervous system. All over the world, several dozen million people suffer from the effects of post-polio, multiple sclerosis, spinal cord injury, cerebral palsy, paraplegia, quadriplegia, muscular dystrophy etc. and could benefit from the advances in robotic devices for rehabilitation [91]. The temporary or permanent loss of human motor functions can be compensated by means of various rehabilitation and assistive devices.

Wearable robotic systems or exoskeletons for rehabilitation or for walking assistance in daily living offer real advantages. In the last decade, the interest in this field has raised mainly due to the growing demand caused by an increasing number of lower-limb disabled patients.

Hybrid Assistive Limb (HAL, Figure 1-30a) is an exoskeleton that is targeted for both performance-augmenting: heavy works, physical training support and rehabilitative purposes [92], [93]. HAL employs controller, computer, harmonic drive motors at the hip, knee, and ankle joints. Power for the motors is supplied by a battery pack mounted on the backpack. HAL system utilizes a number of sensors for control: skin-surface EMG electrodes (Electromyographic electrodes for measuring the activation level of the muscles), potentiometers for joint angle measurement, ground reaction force sensors, a gyroscope, and accelerometer mounted on the backpack for torso posture estimation. The total weight of the device is 21kg. HAL supports activities like standing up from a chair, walking, climbing up and down stairs.

Similarly, ARGO Medical Technologies Ltd. designed a wearable, motorized quasi-robotic exoskeleton that can be used for therapeutic activities named ReWalk (Figure

1-30b) [94]. ReWalk comprises light wearable brace support suit, which integrates DC motors at the joints, rechargeable batteries, an array of sensors, and a computer-based control system. Upper-body movements of the user are detected and used to initiate and maintain walking processes. ReWalk allows paraplegic patients to walk, sit and stand-up, climb up and down the stairs. It lacks body weight support and stability, hence for that reason, there is a need to utilize crutches, to maintain upright position and balance.



(a) HAL



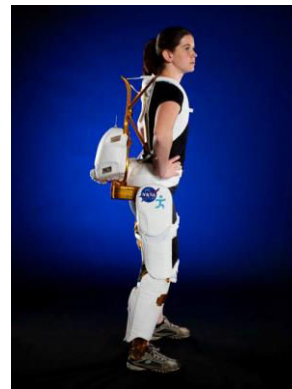
(b) ReWalk



(c) WADBSA



(d) WADSM



(e) X1

**Figure 1-30.** Exoskeletons for walking assistance and rehabilitation.

Japanese company Honda has several devices for walking assistance. One of them named Walking Assist Device with Bodyweight Support Assist (WADBSA, Figure 1-30c) helps support bodyweight to reduce the load on the user's legs while walking [61]. This could lead to reduced fatigue and less physical exertion. The device comprises of 2 motors and gears, rechargeable lithium-ion batteries, control computer, shoes with foot force sensors and a seat. The motors can lighten the load on the user's legs and helps maintain a center of gravity via special mechanisms developed by the company. There is plenty of use cases for this product, not the least of which would be helping industrial workers, people afflicted with mobility issues or leg problems. It can also be used for rehabilitation. Another exoskeleton designed by Honda is Walking Assistive Device with Stride Management (WADS, Figure 1-30d) [95]. This device is developed for patients with weakened leg muscles who are still able to walk. It is comprised of 2 brushless DC motors, rechargeable lithium-ion battery, angle sensors, control computer and operates about 2 hours. A motor helps lift each leg at the thigh as it moves forward and backward. This helps lengthen the user's stride, making it easier to cover longer distances at a greater speed. Its lightweight and simple design with a

belt worn around the hips and thighs reduces the wearer's load and fits different body shapes. The device weighs 2.8kg with batteries.

Dexterous Robotics Lab (DRL) at the NASA Johnson Space Centre in Houston developed an exoskeleton named X1 (Figure 1-30e) in cooperation with the Florida Institute for Human and Machine Cognition (IHMC) in Pensacola [96]. Initially designed as a mobility device for people with paraplegia, X1 had been tailored as an in-space countermeasures device and a dynamometry device to measure muscle strength. The X1 exoskeleton currently has four active degrees of freedom (DOF) at the hips and the knees, with powered movement constrained to the sagittal plane which can assist or resist human movement. It also has six passive degrees of freedom for abduction and adduction; internal and external rotation; and dorsiflexion and plantarflexion. Any of these passive DOFs may be left free to move or locked out to intentionally constrain movement.

Except for the application on walking assistance and rehabilitation, the exoskeletons can be also used for the human power augmentation.

The Berkeley Lower Extremity Exoskeleton (BLEEX, Figure 1-31a) is powered by an internal combustion engine which is located in the backpack [97]. The hybrid engine delivers hydraulic power for locomotion and electrical power for the electronics. The exoskeleton is actuated via bidirectional linear hydraulic cylinders. BLEEX consumes an average of 1143 Watts of hydraulic power during level-ground walking, as well as 200 Watts of electrical power for the electronics and control. In contrast, a similarly sized, 75 kg human consumes approximately 165 W of metabolic power during level-ground walking. The control system utilizes the information from eight encoders and sixteen linear accelerometers to determine angle, angular velocity, and angular acceleration of each of the eight actuated joints, a foot switch, and load distribution sensor per foot to determine ground contact and force distribution between the feet during double stance, eight single-axis force sensors for use in force control of each of the actuators, and an inclinometer to determine the orientation of the backpack with respect to gravity. This control algorithm essentially minimizes the interaction forces between the human and the exoskeleton and instead, utilizes mainly sensory information from the exoskeleton. BLEEX can support a load of up to 75 kg while walking at 0.9 m/s and walk at speeds of up to 1.3 m/s without the load.

Hercule (Figure 1-31b) is another exoskeleton designed for accompanying persons and providing assistance to carry and manipulate heavy loads, developed by the French company RB3D and CEA LIST Interactive Robotics Laboratory [9]. It uses highly efficient electric actuators allowing the current prototype to carry a 40 kg load at 4 km/h speed with an electric autonomy of 4 hours. Only the flexion /extension joints of the knee and hip are actuated. The controller principle is that actuated joints are providing torques to counteract the load weight. The high back-drivability of the actuators (CEA patents) is a key feature to have machine following the user smoothly. The back of the exoskeleton can transmit the load carried by the arms to the exoskeleton legs.



(a) BLEEX



(b) Hercule

**Figure 1-31.** Exoskeletons for human power augmentation

While for the previous designs, rigid links are used for forming their structure and transmitting force to the users. However, the use of rigid components leads to several drawbacks. For example, the caused adding inertia effects which must be compensated by users or actuators, and the misalignment of the links will cause the discomfort and even dangerous injuries to the users.

For solving the previous problems, several soft, suit-like exoskeletons (also known as “exosuit”) have been proposed in recent years. Because of using soft materials like fabrics and cables, the exosuits much lighter than the exoskeletons, therefore, only a little inertia is added to the wearer’s movement. Additionally, since there is no rigid joints or frames exist in exosuits, so there is no problem relating to the joint misalignment. Unlike conventional exoskeleton, exosuit does not contain any rigid elements which can transfer loads to the ground hence the wearers must sustain all the compressive forces by their own bones. Two prototypes of lower-extremity exosuit have been designed by researchers from the Wyss Institute for Biologically Inspired Engineering at Harvard University [98]–[101]. The first one is a lower-extremity exosuit actuated by custom Mckibben style pneumatic actuators (Figure 1-32a) which can assist the hip, knee, and ankle. The actuators attach to the exosuit through a network of soft, inextensible webbing triangulated to attachment points. Because of the use of soft material, this exosuit itself (human interface) weighs only 3.5kg, and experiment shows that it can comfortably transmit joint torques to the user while not restricting mobility. However, it also has some drawbacks like the air supplier is not portable which can limit its mobility. The second one is a soft cable-driven exosuit (Figure 1-32b) that can apply forces to the body to assist walking. The exosuit is fixed on the body by straps and actuated cables can generate moments at the ankle and hip with magnitudes of 18% and 30% of those naturally generated by the body during walking, respectively. The geared motors are used to pull on Bowden cables connected to the suit near the ankle. Like the first design, the worn part of the suit is extremely light, hence the suit’s unintentional interference with the body’s natural biomechanics is negligible.





(a) Pneumatically actuated exosuit



(b) Cable-driven exosuit

**Figure 1-32.** Lower-limb Exosuits.*(b) Upper-limb designs*

Work-related diseases of muscle and skeletal system are prevalent among physically demanding labors. Despite the industrialization has already proceeded for hundreds of years, the number of occupational diseases, as well as cumulative trauma disorders (CTD) caused by overwork, is still significant nowadays. They are caused by ergonomic factors of the work environment, such as physical overload, compulsive working postures, local stiffness of definite muscle groups and an adverse microclimate [102]. When workers carry the load, the gravity and dynamic force of the load will induce quite significant moments to the elbow, shoulder and trunk joint which will lead to the fatigue and even injury of muscles like the bicep, anterior deltoid, spinal extensor etc. [103].

Unlike the lower-limb designs which are mainly focused on the walking assistance, upper-limb exoskeletons can be used for heavy load carriage and upper-limb rehabilitation.

In some factories, workers need to operate hand tools like driller and welding gun and using these tools for a long time can not only be physically exhausting but also lead to muscle fatigue and injury. An exoskeleton recently designed by Lockheed Martin named FORTIS (Figure 1-33a) allows its operators to support heavy tools and enhancing their strength and endurance [104]. FORTIS weighs less than 12.3kg and it transfers the weight of tools to the ground through a series of joints at hips, knees, and ankles. One of the great advantages of FORTIS is that it does not need any actuators (i.e. unpowered) and it can be used in different environments from factory to field work because it is a wearable device and it moves along with the operator's natural movement while standing, bending, leaning or kneeling.

A French company, EXHAUSS, offers a range of exoskeletons, each intended to relieve and protect operators, for various constraints related to handling or carrying loads or tools [105]. In one of their designs, Cinemaker (Figure 1-33b), springs are used for gravity balancing of carrying loads. Cinemaker has 6 DOFs which ensure the user holding load with different postures.



(a) FORTIS



(b) Cinemaker

**Figure 1-33.** Upper-limb Exoskeletons.

Similar to the lower-limb designs, several researchers have also conducted their research on the exoskeleton with soft materials for upper-limb rehabilitation and power augmentation.

MAXFAS (Mechatronic Arm Exoskeleton for Firearm Aim Stabilization, Figure 1-34a) was designed by researchers from U.S. Army Research Laboratory [106]. This exoskeleton aims at sensing and damping involuntary tremors in the arm during shooting activities, and it consists of three carbon fiber braces: one attached to the forearm and the rests attached to the upper arm. Six cables which control 5DOF of the arm terminated at the braces and the motors are mounted on a fixed frame. Due to its cable-driven architecture and carbon fiber construction, MAXFAS adds very little weight to the arm and unlike passive shooting aids that restrict natural voluntary motion of the arm, it allows such motions due to its control algorithm and the lack of rigid joints at the shoulder and elbow. In the test of a small group of mostly inexperienced shooters, MASFAS significantly improved shooting performance and reduced arm tremors. However, one of the major defects of this exoskeleton is that it can not move because of the fixed motors.

Another assistive device with cables for handling heavy objects has been proposed by STRONGARM (Figure 1-34b). The handling system has a rigid frame with a cable winding system. The rigid frame is worn on the user's body and the other end of the cable with the is on the user's finger. When users want to pick up the load, they stretch their arms to the load with the cable locking mechanism on their fingers. Then when they pick up the load, because of the pressure between the load and hands, the cable locking mechanism will be engaged to stop the releasing of the cable. Hence, the gravity of the load will be transferred to the user's body through the cables.



(a) MAXFAS



(b) STRONGARM

**Figure 1-34.** Upper-limb exoskeleton using soft material.

### 1.3.3 Collaborative industrial robot

In the late 20<sup>th</sup> century and the new millennium, industrial robots have been widely used in the manufacturing industry with various applications, ranging from spot welding in the manufacturing in automobiles to the pick-and-place operations in the packaging process. The deployment of industrial robots has many advantages, such as: the repeatability as a tool to achieve consistent quality, the speed and force they make available for the manufacturing processes, the flexibility for different tasks brought by the programmability, the possibility to directly participate hazardous production tasks, and the reduction of the manpower needed. Although industrial robots have drastically increased the efficiency of manufacturing, however, they still have some drawbacks. The installation and commissioning of industrial robot applications are associated with appreciable effort and cost, the underlying assumption in their large-scale deployment in production environments still rests on the economy of scale, which means that for small-scale production or customized production, the deployment of industrial robots is not favorable in terms of the cost. Besides, according to ISO standards, industrial robots are hazardous machines that require safeguarding against human intervention, therefore, investments in protective guards and safety equipment are non-negligible and large spaces are needed for creating safe space for the workers.

Recent years have seen a rather rapid development of more complex safety functionality for industrial robots, driven by the advances in microprocessors and safer components on all levels. In this context, small-scale industrial robots which allow the physical interaction between robot and human have been developed by the top industrial robot manufacturers and technology start-ups. This kind of robot is called collaborative industrial robot (cobot for short). Collaborative industrial robots are highly complex machines which are able to work hand in hand with human beings and support and relieve the human operator in a conjoint workflow. Compare to conventional robots, collaborative robots have their unique features in terms of safety concerns. According to the International Standards ISO 10218 [107], there are four general safety features for cobots:

- **Safety Monitored Stop:** This kind of collaborative feature is used when a robot is mostly working on its own, but occasionally a human might need to enter its workspace. For example, if a worker had to perform a certain operation to a part while the robot was still handling it or remove that part from the cobot's end effector, the cobot will cease movement, but not completely shut down to easily resume its

tasks when the human leaves. Notice that these types of robots are most efficient when people work mostly apart from the robot, but might get closer for a small amount of time. Otherwise, a lot of time could be lost as the robot continuously stops for human interruptions.

- **Hand Guiding:** Hand guiding is a collaborative feature used for path teaching a robot – literally guiding the robot through a sequence of motions required to complete a task, like pick-and-place applications. These cobots often using end effector technology to sense its position and read forces applied to the robot's tooling, allowing a cobot to learn through the demonstration of an operator. It should be noticed that, this type of collaboration only applies to the robot while it is performing this particular function, which means that while the robot is functioning in its other modes, the robot still needs to have safeguarding in place.
- **Speed and Separation Monitoring:** For applications requiring more frequent human intervention with larger cobots, a laser vision system can be installed in the environment to allow the robot to sense a human's proximity. The robot will act within the functions of the safety zones that have been pre-designed for it. If the human is within a certain safety zone, the robot will respond with designated speeds (generally slow) and stop when the worker comes too close. So, when the workers are approaching the robot, it slows down, as the workers approach even closer, the robot slows down even more or stops. The robot will resume its task and slowly accelerate its motion as the operator moves further away.
- **Power and Force Limiting:** Force limited collaborative robots can read forces in their joints, like pressure, resistance or impacts using embedded sensors. The cobot can feel abnormal forces in its path. In fact, it is programmed to stop when it reads an overload in terms of force. The new ISO/TS 15066 technical specification specify the maximum forces and energy that can be applied to a human without any harm.

With the great benefits and potentials of cobots, conventional industrial robot companies start to develop their collaborative versions of robot. German-based industrial robot pioneer KUKA released the first cobot LBR 3 in 2004. This computer-controlled lightweight robot was the result of a long collaboration with the German Aerospace Center since 1995 [108]. The LBR 3 has 7 degrees of freedom and with the capability of handling a payload up to 14kg. After the LBR 3, KUKA developed the succeeding models with more advanced collaborative features: the KUKA LBR 4 in 2008 and the KUKA LBR iiwa (shown in Figure 1-35a) in 2013. It can be seen that the KUKA LBR-series robots are all designed with round shells which are expected to dissipate forces in case of impact on a wide surface. Additionally, they all have internal motors and wiring which is intended to shrink their overall size as much as possible.

Following the step of KUKA, a Danish technology start-up Universal Robots which was founded by three engineers at the University of Southern Denmark, released its first cobot, the UR5 (shown in Figure 1-35b), in 2008. After the UR5, Universal Robots released the UR10 which has a higher lifting ability and a tabletop cobot UR3, in 2012 and 2015 respectively. All these three cobots have six degrees of freedom and the number in their name denotes the maximum payload in kg they can manipulate.



(a) KUKA: LBR iiwa



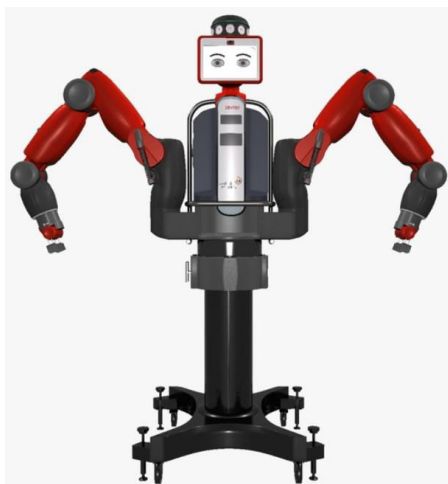
(b) Universal Robots: UR 5



(c) Fanuc: CR-35iA



(d) Denso: Cobotta



(e) Rethink Robotics: Baxter



(f) ABB: Yumi

**Figure 1-35.** Collaborative industrial robots.

After the success of cobots from KUKA and Universal Robots, Japanese robot manufacturer Fanuc released its first cobot CR-35iA (shown in Figure 1-35c) in 2015. CR-35iA is one of the biggest cobots from now with the maximum payload up to 35kg.

Another Japanese company Denso released a tiny table top 6-DoF cobots Cobotta (shown in Figure 1-35d) in 2017 which is one of the smallest cobot with a maximum payload of only 0.5kg.

Apart from the previously mentioned cobots which are all single-arm design, dual-arm cobots are also developed for having more flexibility and being more anthropomorphic. Dual-arm cobots function more like a human, hence during co-working with workers, they have more autonomy which operates similarly to a co-worker instead of a robot.

The American startup Rethink Robotics which was founded by the former professor of MIT Rodney Brooks, released their first industrial cobot Baxter (shown in Figure 1-35e) in 2012 and a smaller, faster collaborative robot Sawyer in 2015, designed for high precision tasks. Baxter is a dual-arm cobot which has 7 degrees of freedom for each of its arm (14 degrees of freedom in total). It has an animated screen for a "face" that allows it to display multiple facial expressions determined by its current status. There are sets of sensors on its head that allow it to sense people nearby and give Baxter the ability to adapt to its environment. These sensors give Baxter the ability to adapt to its surroundings. Similar to Baxter, the Swiss-based industrial robot manufacturing giant ABB also released a dual-arm cobot Yumi (shown in Figure 1-35f) in 2015.

Although the collaborative industrial robots provide a lot of merits in terms of its collaborative features, however, it should be noticed that for most of the cobots, the maximum payload they can handle is below 10kg. Hence, if we want a robot by itself to take an operation on a heavy payload, the only choice is the conventional industrial robot.

The critical review has shown that in each of the three examined parts there are design concepts that can be improved. Therefore, the following tasks have been considered in the thesis.

### ***1.4 Outline of the thesis***

The following problems have been discussed in the next chapters.

- Chapter 2 deals with the development of single actuator walking robots designed by coupling of two mechanisms. Three various design concepts are carried out via coupling of two units, which are either linkages or cam mechanisms. The designs presented in this chapter have more flexibility related to reviewed solutions. They allow one to create the walking robots with different step lengths, with possibility to climb up stairs.
- Chapter 3 considers the optimal design and synthesis of gravity balancers, which consist of a rotating link to be balanced and a two-link dyad. It is known that a full gravity compensation of a rotating link cannot be achieved when a non-zero free length spring, i.e. conventional linear spring, is used. To use non-zero length springs, it is necessary to apply auxiliary mechanical systems. In this chapter, three gravity balancers with different coupled units are proposed. An optimization method based on the geometric synthesis of mechanism and potential energy conservation is developed, which allows one to control the optimal displacement of the spring providing a suitable balancing moment. The

minimization of the unbalanced moment by taking into account the mass of the added rocker and the spring is also considered.

- Chapter 4 presents a robotic suit (exosuit) designed for assisting people while carrying heavy loads. Unlike the designs with rigid structures which have some drawbacks like additional inertia and the in compliant interface between them and users, for the proposed exosuit, polyethylene braid-style cables are used and attached to the user's body through anchors and attachment points, which function as auxiliary muscles to apply force on both upper arm and forearm. The weight of the cables is negligible and adds nearly zero inertia to users. One of the characteristics of the proposed exosuit is that it has two operation modes: passive and active modes. The kinematic and the dynamic models of the exosuit-human coupled system are developed. And the static, kinematic and dynamic simulation of the coupled system, as well as the optimization of the distribution of cable attaching positions, are discussed. Finally, the experimental results carried out on a mannequin test bench are presented.

- Chapter 5 considers a coupled system including a hand-operated balanced manipulator (HOBM) and an industrial collaborative robot (cobot) is presented. The advantages of the coupled HOBM and cobot are disclosed and the optimal design of the cooperative workspace is discussed. Dynamic analysis of the coupled system is performed for investigating the oscillation of the HOBM at the final phase of the prescribed trajectories. Two methods for reducing the oscillation of the HOBM through introducing a telescopic axis and damping moments are proposed. The additional load exerted on the cobot by the inertia effects of the HOBM is studied and the admissible trajectory of the coupled system is determined.

- This thesis ends with conclusions.





# Design and synthesis of single actuator walking robots via coupling of linkages

---

2.1	Design and synthesis of a single actuator walking robot via coupling of four-bar linkages .....	37
2.2	Design and Synthesis of a Single Actuating Walking Robot via Coupling an adjustable slider-crank mechanism .....	46
2.3	Design and synthesis of a single actuator walking robot via coupling of the driven cam system and the pantograph mechanism .....	53
2.4	Summary.....	60

---

*This chapter deals with the development of single actuator walking robots designed by coupling of two mechanisms. The advantages of such robots have been disclosed in chapter 1. It is the simplicity of the design and its control system. In this chapter, three various design concepts are considered. All proposed concepts are carried out via coupling of two units, which are either linkages or cam mechanisms.*

*In the first section of the chapter, the single actuator walking robot is designed via coupling of two four-bar linkages. For this purpose, the geometric synthesis of the four-bar linkage through the prescribed path has been developed. Based on the Genetic Algorithm, the synthesis allows one to ensure the reproduction of prescribed points of the given trajectory obtained from the walking gait. The actuator mounted on the robot's frame moves both legs, which are four-bar linkages. A walking robot designed by suggested concept can move both forward and backward directions. The observations showed that such a robot can ensure only a constant step during the walking gait.*

*The adjustment of geometric parameters of a four-bar linkage to obtain variable lengths of steps is a fairly complex problem. Therefore, in the next section, the design of a single actuator walking robot based on the coupling of slider-crank mechanisms is considered. It is shown that the length of the step can be modified via the changing the offset of the slider guide. The CAD simulations show that the proposed design concept allows one to vary the offset of the slider guide from 0 to 60cm and obtain lengths of steps from 120cm to 160cm. Thus, the adjustment of the offset of the slider guide allows one to obtain steps with variable*

*lengths. However, that does not allow one to change the form and the orientation of steps.*

*Hence, in the last section of the chapter, the design of a single actuator walking robot via the coupling of a cam mechanism and a pantograph linkage is discussed. In this case, the adjustable parameters are the angle between the cam mechanism and the robot moving frame, as well as the input points of the pantograph mechanism. The proposed concept allows significant variations of the walking speed during the horizontal displacements of the robot and climbing stairs.*

*All suggested design concepts have been validated through CAD simulations carried out via ADAMS software.*

## ***2.1 Design and synthesis of a single actuator walking robot via coupling of four-bar linkages***

### **2.1.1 Introduction**

The four-bar mechanism is one of the simplest but practically widespread mechanisms. It has been used in various industrial fields, such as automatic door-closing systems, train suspensions, front loader mechanisms, wiper-blades mechanism, etc. In order to adopt the four-bar mechanism into different engineering fields, many researchers [109]–[112] have conducted their researches on the graphical and analytical methods of the synthesis of the four-bar mechanism. However, these methods are often with low precision and will increase the complexity when the prescribed points increased [113].

In the last three decades, with significant development of the computer industry, the computational ability of computer has been greatly increased which allow researchers via numerical methods to solve sophisticated optimization problems in the field of geometrical synthesis. Genetic algorithm (GA) is a kind of mathematical algorithm which is inspired by the process of natural selection. Nowadays, GA is widely and commonly used for solving complex optimization problems [114].

In this section, the design of a single actuator walking robot via coupling of four-bar linkages is considered. Therefore, firstly, let us consider the synthesis of the four-bar linkage with GA.

### **2.1.2 Synthesis of the four-bar linkage via genetic algorithm**

#### **a) Optimization method**

In GA, a population of candidate solutions (individuals) to an optimization problem is evolved toward better solutions. Like the creature, each individual has a set of properties (chromosomes) which can be mutated and altered.

Normally, the GA starts from a population of individuals which are randomly generated, and the population in each iteration is called a generation. In each generation, there is an objective function to evaluate the fitness of each individual in the population. The more fit individuals are stochastically selected from the current population, and each individual's genome is modified (recombined and mutated) to form a new generation. The new generation of candidate solutions is then used in the next iteration of the algorithm. Commonly, when the maximum number of generations or a satisfactory fitness level is reached, the GA will be terminated. The general procedure of GA is shown in Figure 2-1.

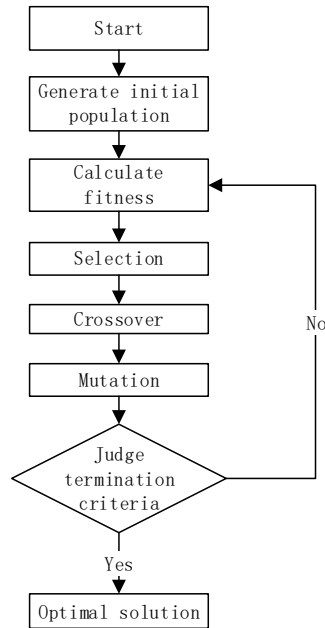


**Figure 2-1.** General procedure of Genetic Algorithm.

The selection procedure chooses parents for the next generation based on their fitness values. During each successive generation, a portion of the existing population is selected to breed a new generation. Certain selection methods rate the fitness of each solution and preferentially select the best solutions. Other methods rate only a random sample of the population, as the former process may be very time-consuming.

In the present study, the stochastic uniform method is used in the selection procedure. It lays out a line in which each parent corresponds to a section of the line of length proportional to its expectation. The algorithm moves along the line in steps of equal size, one step for each parent. At each step, the algorithm allocates a parent from the section it lands on. The first step is a uniform random number less than the step size.

In GA, the crossover is a genetic operator used to vary the programming of a chromosome or chromosomes from one generation to the next. It is analogous to reproduction and biological crossover, upon which genetic algorithms are based. Crossover is a process of taking more than one parent solutions and producing a child solution from them. There are methods for selection of the chromosomes (i.e. Scattered, Single point, Intermediate).

Scattered has been used in the Crossover process of the present study. Scattered creates a random binary vector. It then selects the genes where the vector is a 1 from the first parent, and the genes where the vector is a 0 from the second parent, and combines the genes to form the child. This method can be shown as

$$\begin{aligned}
 p_1 &= [a \ b \ c \ d \ e \ f \ g \ h] \\
 p_2 &= [1 \ 2 \ 3 \ 4 \ 5 \ 6 \ 7 \ 8] \\
 \text{random crossover vector} &= [1 \ 1 \ 0 \ 0 \ 1 \ 0 \ 0 \ 0] \\
 \text{child} &= [a \ b \ 3 \ 4 \ e \ 6 \ 7 \ 8]
 \end{aligned}
 \tag{2-1}$$

Mutation is a genetic operator used to maintain genetic diversity from one generation to the next. It is analogous to biological mutation. Mutation alters one or more gene values in a chromosome from its initial state. In mutation, the solution may change entirely from the previous solution. Hence GA can come to a better solution by using mutation. A mutation occurs during evolution according to a user-definable mutation probability. This probability should be set low. If it is set too high, the search will turn into a primitive random search.

There are several algorithms for Mutation in GA, for example, Gaussian, Uniform, and Adaptive feasible. In the present study, the Adaptive feasible has been used in the Mutation procedure. It randomly generates directions that are adaptive with respect to the last successful or unsuccessful generation. A step length is chosen along each direction so that linear constraints and bounds are satisfied.

Let us consider the application of the GA to the optimal synthesis of the four-bar linkage.

**b) synthesis of four-bar mechanism with prescribed path trajectory**

To adapt the GA to the path-generation based optimal synthesis of the four-bar mechanism (Figure 2-2), the goal function in the GA must be defined at first.

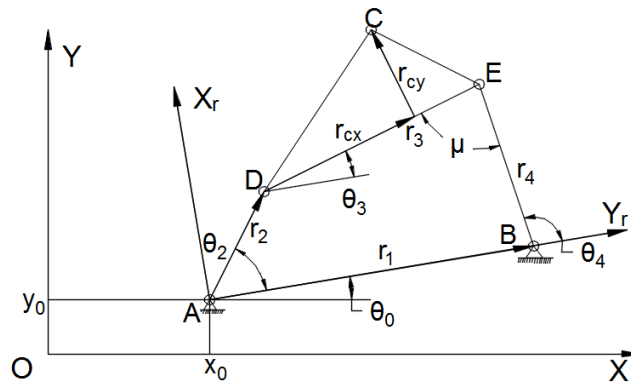


**Figure 2-2.** A planar four-bar mechanism with design parameters.

The ultimate goal of the path-generation based optimal synthesis is to optimize a four-bar mechanism which can generate a path (the trajectory of point C in Figure 2.2) as close as possible to the prescribed points (also known as design points). Hence, the first part of the goal function is the difference between actual points and design points, which can be expressed by:

$$\sum_{i=1}^N [(C_{Xd}^i - C_X^i)^2 + (C_{Yd}^i - C_Y^i)^2] \tag{2-2}$$

where  $N$  is the number of design points,  $\mathbf{C}_i = [C_X^i, C_Y^i] = [C_X(\theta_2^i), C_Y(\theta_2^i)]$  is the coordinates of actual path points of the optimized four-bar mechanism,  $\mathbf{C}_d^i = [C_{Xd}^i, C_{Yd}^i]$  is the coordinates of the design points.

In the optimal synthesis, the design variables are  $r_1, r_2, r_3, r_4, r_{cx}, r_{cy}, \theta_0, x_0, y_0$ , and input angle  $\theta_2$  as shown in Figure 2.2. However, to calculate the coordinates of actual points

$C_i$ , the value of  $\theta_3$  must be solved first. In order to calculate  $\theta_3$ , the closed equation of the four-bar mechanism has been introduced:

$$\begin{cases} r_2 \sin \theta_2 + r_3 \sin \theta_3 = r_4 \sin \theta_4 \\ r_2 \cos \theta_2 + r_3 \cos \theta_3 = r_1 + r_4 \cos \theta_4 \end{cases} \quad (2-3)$$

It can be rewritten as:

$$\begin{cases} \cos \theta_4 = (r_2 \cos \theta_2 + r_3 \cos \theta_3 - r_1) / r_4 \\ \sin \theta_4 = (r_2 \sin \theta_2 + r_3 \sin \theta_3) / r_4 \end{cases} \quad (2-4)$$

By squaring both the equations of Eq. 2-4 and adding them together, we can obtain a quadratic equation with respect to  $\cos \theta_3$ . And the solution can be represented as flowing:

$$\cos \theta_3 = \frac{AB}{D^2} \pm \left[ \left( \frac{AB}{D^2} \right)^2 - \frac{B^2 - C^2}{D^2} \right]^{1/2} \quad (2-5)$$

where:

$$\begin{aligned} A &= 2r_3(r_2 \cos \theta_2 - r_1) \\ B &= r_4^2 - r_1^2 - r_2^2 - r_3^2 + 2r_1 r_2 \cos \theta_2 \\ C &= 2r_2 r_3 \sin \theta_2 \\ D &= (A^2 + C^2)^{1/2} \end{aligned}$$

then  $\theta_3$  and  $\theta_4$  can be easily calculated:

$$\begin{aligned} \theta_3 &= \arccos \left\{ \frac{AB}{D^2} \pm \left[ \left( \frac{AB}{D^2} \right)^2 - \frac{B^2 - C^2}{D^2} \right]^{1/2} \right\} \\ \theta_4 &= \arccos [(r_2 \cos \theta_2 + r_3 \cos \theta_3 - r_1) / r_4] \end{aligned} \quad (2-6)$$

Thus, the position of point  $C$  in the local reference  $O_2X_rY_r$ , which has been defined in Figure 2-2, is:

$$\begin{aligned} C_{X_r} &= r_2 \cos \theta_2 + r_{cx} \cos \theta_3 - r_{cy} \sin \theta_3 \\ C_{Y_r} &= r_2 \sin \theta_2 + r_{cx} \sin \theta_3 + r_{cy} \cos \theta_3 \end{aligned} \quad (2-7)$$

and it can be transferred to the global coordinate in reference  $OXY$ :

$$\begin{bmatrix} C_X \\ C_Y \end{bmatrix} = \begin{bmatrix} \cos \theta_0 & -\sin \theta_0 \\ \sin \theta_0 & \cos \theta_0 \end{bmatrix} \begin{bmatrix} C_{X_r} \\ C_{Y_r} \end{bmatrix} + \begin{bmatrix} x_0 \\ y_0 \end{bmatrix} \quad (2-8)$$

The first part of the goal function can be calculated from Eq. (2-2).

In order to obtain a desirable four-bar mechanism, there are several constraints which have to comply with. For example, the Grashof condition which allows at least one link has the entire rotation, sequence condition of input angle  $\theta_2$  which guarantee the continuity of input angles, and the limitation of design variables. Therefore, in the second part of the goal function, these constraints have been introduced. Now, the synthesis conditions can be described as follows:

$$\min \left\{ \sum_{i=1}^N \left[ (C_{Xd}^i(X) - C_X^i(X))^2 + (C_{Yd}^i(X) - C_Y^i(X))^2 \right] \right\}$$

subject to:

(a) Grashof condition:  $2(r_{max} + r_{min}) < (r_1 + r_2 + r_3 + r_4)$

(b) Sequence condition:  $\theta_2^j < \theta_2^{mod(j+1,N)} < \dots < \theta_2^{mod(j+N,N)}$

(c) Limitation of design variables:  $x_i \in [L_i^l, L_i^u] \forall x_i \in X$

where  $r_{max}$  is the length of the longest linkage,  $r_{min}$  is the length of the shortest linkage,  $\theta_2^i$  is the value of  $\theta_2$  in its  $i^{th}$  position,  $\theta_2^j = \min\{\theta_2^i\}$ ,  $X$  is the set of all design variables,  $L_i^l$  and  $L_i^u$  are the lower and upper limit of  $i^{th}$  design variable.

In GA, the limitation of design variables can be prescribed. With the addition of the penalty of the constraints, the entire goal function can be written as:

$$\min \left\{ \sum_{i=1}^N \left[ (C_{Xd}^i(X) - C_X^i(X))^2 + (C_{Yd}^i(X) - C_Y^i(X))^2 \right] + P_1 f_1(X) + P_2 f_2(X) \right\} \quad (2-9)$$

where  $f_1(X) = 0$  when Grashof condition is satisfied

$$f_1(X) = 1 \text{ when Grashof condition is not satisfied}$$

$$f_2(X) = 0 \text{ when Sequence condition is satisfied}$$

$$f_2(X) = 1 \text{ when Sequence condition is not satisfied}$$

and  $P_1$  and  $P_2$  are the penalty coefficients of Grashof and Sequence condition, which are usually set to a high value in order to have suitable results.

### 2.1.3 Design of the walking robot with one actuator via four-bar mechanism

In the present study, Matlab and its GA toolbox have been used for the implementation of the method described in the previous part. The general setting of the problem is showed by Table 2-1. During the optimization, the best fitness values with respect to the generation are shown in Figure 2-3. The optimization satisfied the stopping criteria

at 50<sup>th</sup> generation with a final error of 0.029 and the best optimized parameters are:  $r_1=34.38$  mm;  $r_2=12.45$  mm;  $r_3=33.19$  mm;  $r_4=40.85$  mm;  $r_{cx}=14.66$  mm;  $r_{cy}=34.20$  mm;  $\theta_0=0.249$ ;  $x_0=44.95$  mm;  $y_0=25.73$  mm;  $\theta_2^1=5.806$ ;  $\theta_2^2=6.209$ ;  $\theta_2^3=0.221$ ;  $\theta_2^4=0.524$ ;  $\theta_2^5=0.949$ ;  $\theta_2^6=3.481$ . Figure 2-4 shows the trajectory generated by the designed mechanism and prescribed points. As we can see, this is a very desirable trajectory for design a walking robot. Figure 2-5 shows the change transmission angle of the optimal mechanism with the rotation of the input link. It can be seen that the optimal mechanism is a proper design since the transmission angles are between 35° and 80° [115].

**Table 2-1.** General Setting of the optimization

$C_d^i$ ( $i=1-6$ ) (mm)	(20,20), (30,20), (40,20), (50,20), (60,20), (40,4)
Optimized Parameters	$r_1, r_2, r_3, r_4, r_{cx}, r_{cy}, \theta_0, x_0, y_0, \theta_2^i; i=1,2,\dots,6$
Limits of the Parameters	$r_1, r_2, r_3, r_4, r_{cx}, r_{cy}, x_0, y_0 \in [0,60];$ $\theta_0, \theta_2^i \in [0,2\pi]; i=1,2,\dots,6$
Setting of GA	Amount of population: 1000; Crossover fraction: 0.8; Maximum generation: 1000

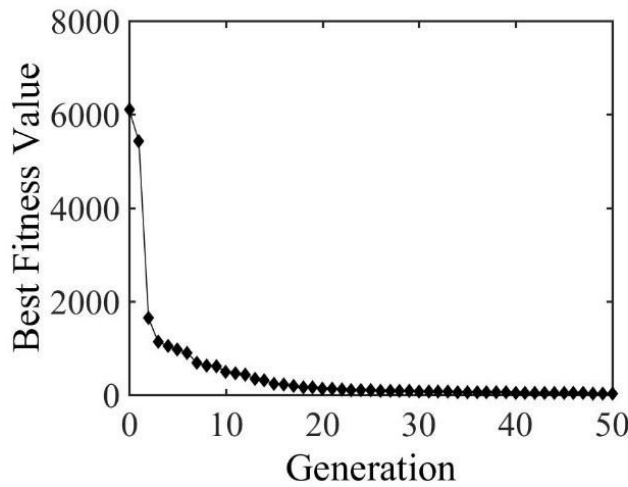


**Figure 2-3.** Best fitness values with respect to the generation.



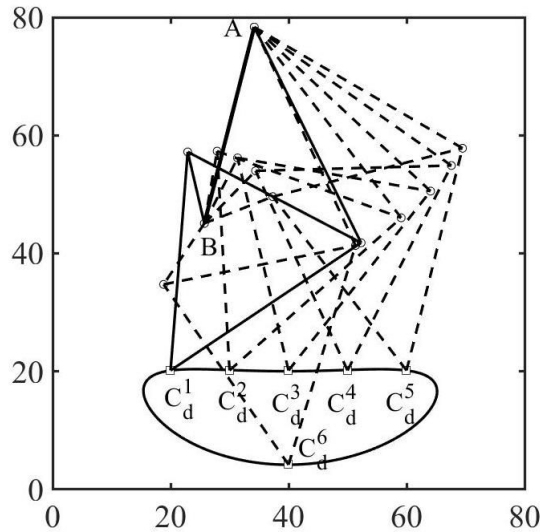


**Figure 2-4.** Trajectory generated by the optimal mechanism and design points.

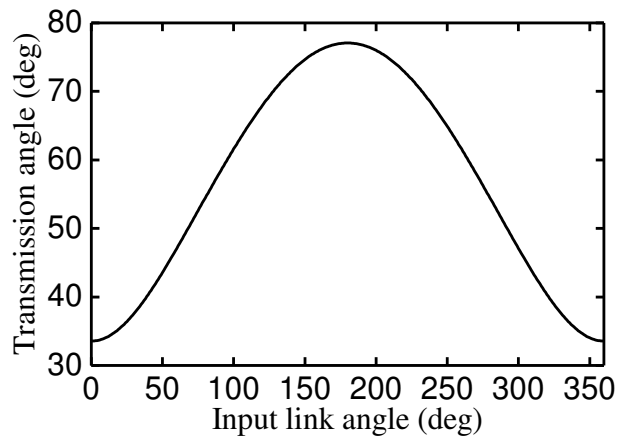


**Figure 2-5.** Change of transmission angle with respect to the input bar angle.

After obtaining the parameters of the optimal four-bar mechanism, the design the walking robot can be carried out. Figure 2-6 shows the relationship between input link motion and leg trajectory. It can be seen that the input link motion with respect to the stand and swing phase are equally divided where the input link motion with respect to the stand and swing phase is represented by the thick and thin dot lines respectively. The thick and thin part of the foot trajectory represent the leg in stand and swing phase respectively; the difference of the angles of input bar between two legs is always 180 deg, hence the left and right leg can be driven by a single actuator. The CAD model of the suggested walking robot was built by using dynamics simulation software ADAMS (Figure 2-7). It should be noted that two feet are connected at the output points of the four-bar mechanisms by torsion springs and dampers which maintain the balance of the robot during walking.

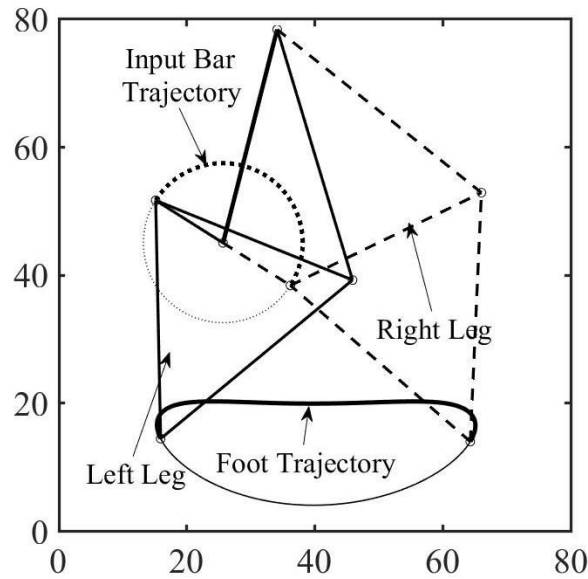


**Figure 2-6.** Leg trajectory with respect to the motion of input link.

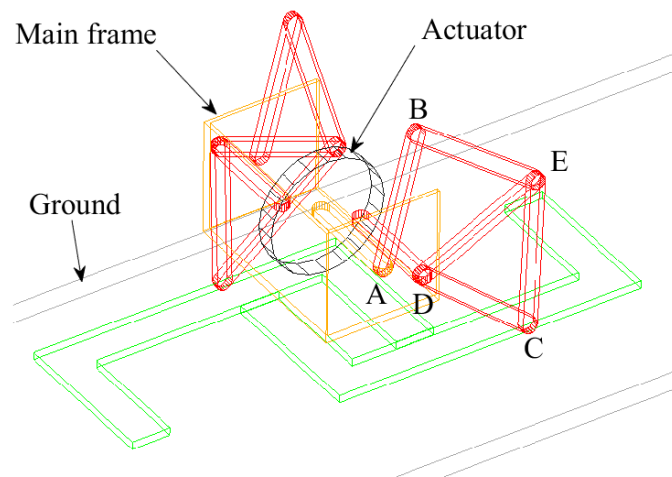


**Figure 2-7.** CAD model of the walking robot.

### 2.1.4 Illustrative example with CAD simulation results

To validate the capability of the proposed walking robot, simulations were carried out via ADAMS software.

In order to simulate the proposed design in both different speeds and different walking directions, there different rotational speeds of actuator have been set, which are 60deg/s, 120 deg/s, -60 deg/s respectively. The total simulation time of each simulation is 30s.

Figure 2-8 and Figure 2-9 show the snapshots of part of the motion of the walking robot during simulation when it's walking forward and backward with the speeds of the actuator are 60 deg/s and -60 deg/s respectively. The simulations validated that the robot has the ability of both walking forward and backward.

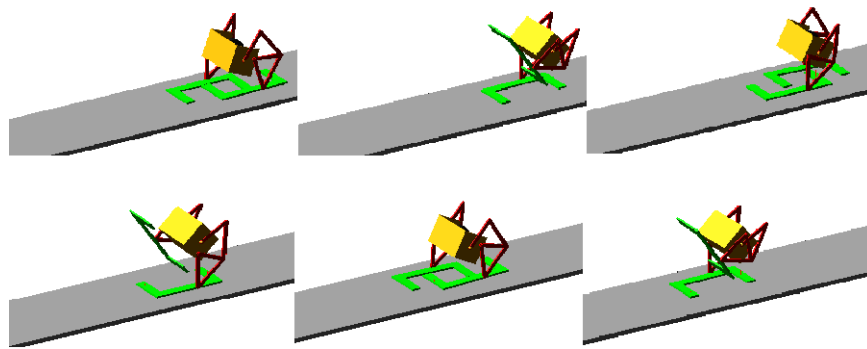


**Figure 2-8.** Snapshots of the simulation when robot moving forward.

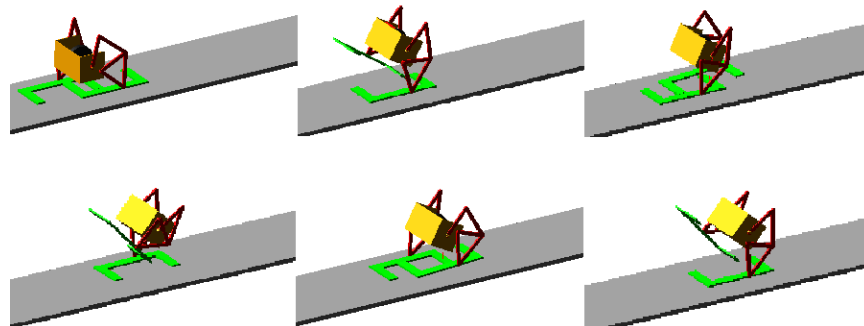


**Figure 2-9.** Snapshots of the simulation when robot moving backward.

The displacements of the mass center of the robot's moving frame along the walking direction with different actuator speeds are shown in Figure 2-10. As we can see from these two figures, the robot was walking at a constant speed with both low and high speeds and different walking directions.

Figure 2-11 shows the power consumption with respect to the different phase of the gait cycle. It can be seen that, during the two transition phases (about 0~10% and 50~60%), the power consumption is fluctuating since in these phases, the front foot is transiting from the swing phase to the stand phase and the contact force between the foot and the ground will exert perturbation to the robot.

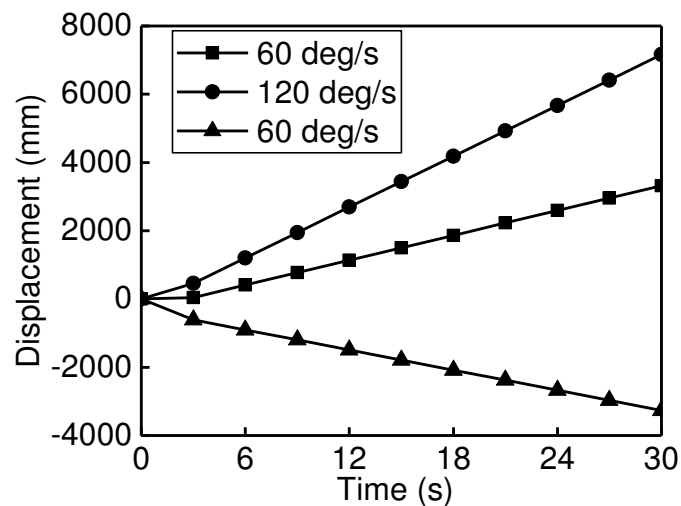


**Figure 2-10.** Displacements of the mass center of robot’s moving frame along walking direction with different walking speeds.

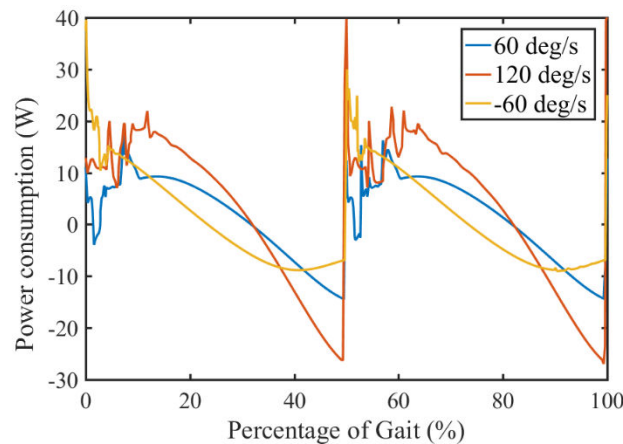


**Figure 2-11.** Power consumption in different phase of gait.

## 2.2 Design and synthesis of a single actuator walking robot via coupling adjustable slider-crank mechanisms

### 2.2.1 Introduction

As shown in the previous section, leg mechanisms have a lot of advantage like having only a single DOF and not requiring a complicated control systems. However, for a leg mechanism with certain lengths of links and revolute joints, only a fixed gait can be generated. If one wants to change the gait, for example, increasing the stride length, we have to redesign the mechanism and change the lengths of its links. Thus, the adaptability of the leg based on the four-bar linkage is limited.

To create a leg with variable gaits, in this section, an adjustable slider-crank mechanism is proposed.

### 2.2.2 Synthesis of adjustable slider-crank mechanisms

The proposed adjustable slider-crank mechanism is shown in Figure 2-12. In the mechanism, the crank OA rotates about the fixed pivot O, and the slider is linked with crank OA via connecting rod AB. A second rod AC is fixed with link AB for generating the output trajectory at point C.

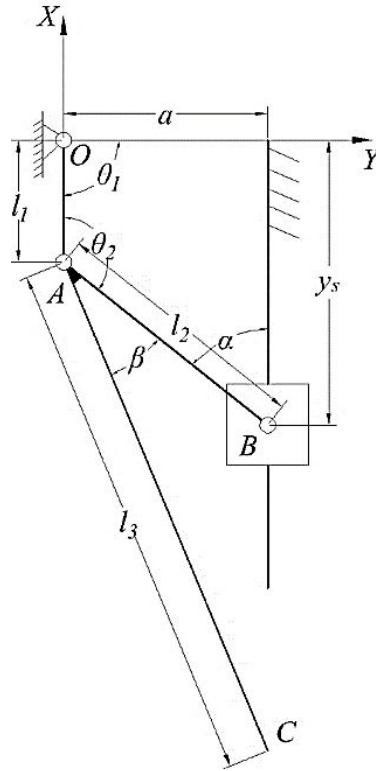


**Figure 2-12.** The adjustable slider-crank mechanism.

For a given input angle of the mechanism  $\theta_1$ , coordinates of the point A can be expressed as:

$$\begin{cases} x_A = l_1 \cos(-\theta_1) \\ y_A = l_1 \sin(-\theta_1) \end{cases} \quad (2-10)$$

where  $l_1$  is the length of the link AB.

Then the position of slider B can be calculated by:

$$\begin{cases} x_B = a \\ y_B = y_A + \sqrt{l_2^2 - (a - x_A)^2} \end{cases} \quad (2-11)$$

where  $l_2$  is the length of connecting rod AB and,  $a$  is the distance between the slider guide and the fixed pivot O.

The counterclockwise angle between the links OA and AB is:

$$\theta_2 = \begin{cases} -\arccos\left(\frac{\mathbf{v}_{OA} \cdot \mathbf{v}_{AB}}{|\mathbf{v}_{OA}| |\mathbf{v}_{AB}|}\right) & (x_A y_B - y_A x_B \geq 0) \\ -\arccos\left(\frac{\mathbf{v}_{OA} \cdot \mathbf{v}_{AB}}{|\mathbf{v}_{OA}| |\mathbf{v}_{AB}|}\right) + \pi & (x_A y_B - y_A x_B < 0) \end{cases} \quad (2-12)$$

where  $\mathbf{v}_{OA}$  and  $\mathbf{v}_{AB}$  denote the vector from point O to point A and from point A to point B respectively.

Thus, the coordinates of the coupler point C can be written as:

$$\begin{cases} x_C = l_1 \cos(-\theta_1) + l_3 \cos(-\theta_1 + \theta_2 + \beta) \\ y_C = l_1 \sin(-\theta_1) + l_3 \sin(-\theta_1 + \theta_2 + \beta) \end{cases} \quad (2-13)$$

where  $l_3$  is the length of the link AC.

For the proposed adjustable slider-crank mechanism, when the lengths of the links are determined, its capability of generating various path is ensured by the adjustment of the offset of slider guide  $a$  and the angle  $\beta$  between the links AB and AC. The output path at the point C is constrained by the geometric property of dyad OAC where all the generated paths are tangent to two concentric circles with radii of  $R_{\max} = l_1 + l_3$  and  $R_{\min} = |l_1 - l_3|$ , and lie inside the range of them. When link OA is colinear with link AC, the point C is at the maximum distant  $R_{\max}$  or minimum distance  $R_{\min}$  to pivot O.

Different paths generated by adjusting the value of  $a$  and  $\beta$  of the proposed slider-crank mechanism with the non-dimensional lengths of links  $l_1=1$ ,  $l_2=5$ ,  $l_3=10$  are show in Figure 2-13. The various adjustable parameters of the paths are as following: path (a):  $\beta=20$  deg,  $a=2$ ; path (b):  $\beta=10$  deg,  $a=2$ ; path (c):  $\beta=20$  deg,  $a=3$ ; path (d):  $\beta=10$  deg;  $a=3$ .

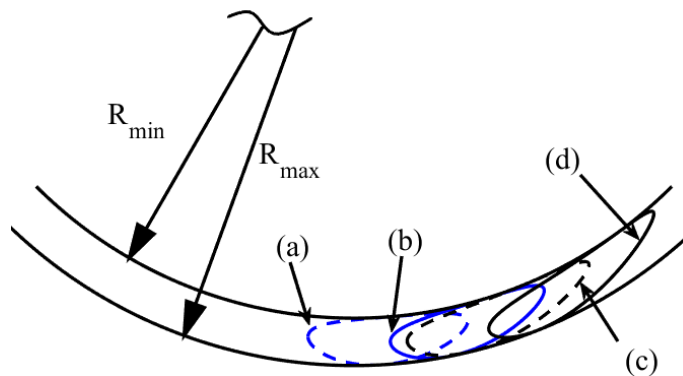


**Figure 2-13.** Different paths generated by the adjustable slider-crank mechanism.

### 2.2.3 Design of the single actuator walking robot via adjustable slider-crank mechanism

In order to apply the proposed mechanism for designing the single actuator robot, let us first assume that for a full range of motion of the driving link OA ( $\theta_1 \in [0, 2\pi]$ ), the input angles corresponding to the stand and swing phases of walking are equally divided. Hence the phase difference between the two legs of the robot is always  $\pi$ , which gives the possibility for actuating the robot by only one motor.

For ensuring the output trajectory of the mechanism is not skew, we let the coupler point at its maximum and minimum distance to the fixed pivot when input angles equal 90 deg and 270 deg respectively. Hence the angle between the coupler AB and connecting link AC is:

$$\beta = \frac{\pi}{2} - \arcsin\left(\frac{a}{l_2}\right) \quad (2-14)$$

Thus, to ensure this constraint, only one adjustable parameter  $a$  should be considered.

The two input angles of the left and right leg,  $\theta_2^{left}$  and  $\theta_2^{right}$  corresponding to the situation when both legs are touching the ground can be calculated by solving Eq. (2-15).

$$\begin{cases} y_C(\theta_1 = \theta_1^{left}) = y_C(\theta_1 = \theta_1^{right}) \\ |\theta_1^{left} - \theta_1^{right}| = \pi \end{cases} \quad (2-15)$$

Then the step length  $l_{step}$  of the leg mechanism can be obtained by:

$$l_{step} = |x_C(\theta_1 = \theta_1^{left}) - x_C(\theta_1 = \theta_1^{right})| \quad (2-16)$$

In the proposed design of the single-actuator walking robot, the lengths of each link of the leg mechanism are chosen as following:  $l_1=20\text{mm}$ ,  $l_2=100\text{mm}$ , and  $l_3=400\text{mm}$ . And the moving range of the slider guide is  $a \in [0, 60\text{mm}]$ .

The step length with respect to the slider guide position is shown in Figure 2-14. It can be seen that, while the slider guide is moving away from the fixed pivot, the step length of the leg mechanism is increasing exponentially.

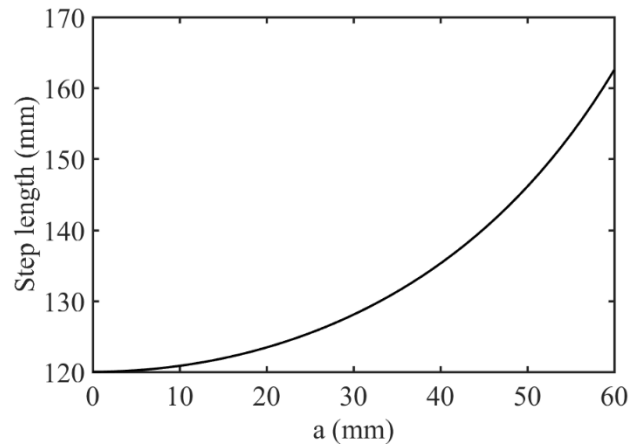


**Figure 2-14.** Step length with respect to the slider guide position.

### 2.2.4 Illustrative example with CAD simulation results

For illustration and evaluation of the performance of the proposed design, a CAD model has been built via ADAMS (Figure 2-15). As shown in the figure, the grey box is the body frame of the robot which contains the actuator, battery, transmission system and payload. Two adjustable slider-crank mechanisms are linked with the body on the left and right sides. In order to keep the feet always being parallel to the ground, parallelogram mechanisms have been created between the leg mechanisms and the feet.

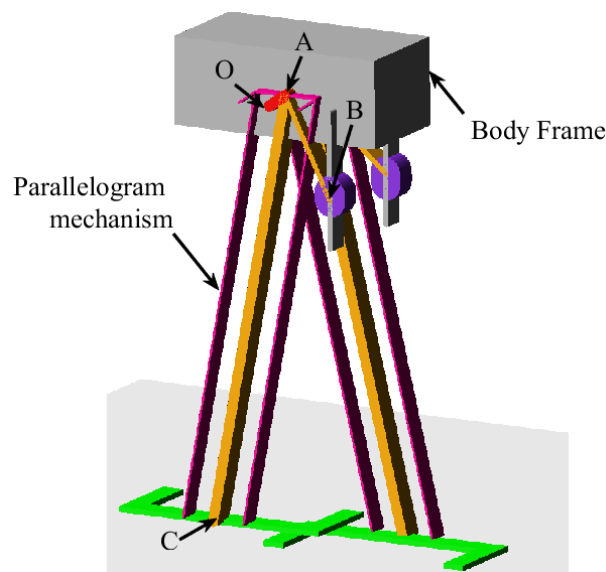


**Figure 2-15.** ADAMS model of the proposed design.

In the simulations, four configurations of the adjustable slider-crank mechanism are chosen and their offset of slider guide ( $a$ ), fixed angle ( $\beta$ ), and step length are shown in Table 2-2. Figure 2-16 shows the gait generated by the slider-crank mechanism with adjustable parameters.



**Table 2-2.** Variation of adjustable parameters and step length of the leg mechanism

No. of gait	1	2	3	4
$a$ (mm)	0	20	40	60
$\beta$ (deg)	0	11.54	23.58	36.87
Step length (mm)	120	123.43	135.25	162.53

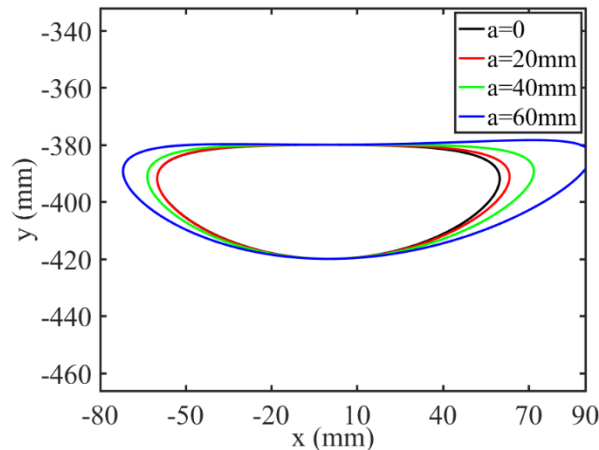
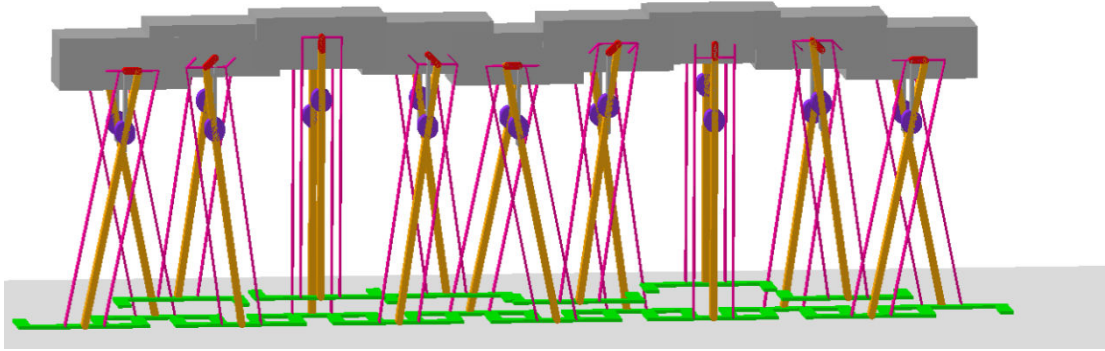


**Figure 2-16.** Different gaits generated by the walking robot.

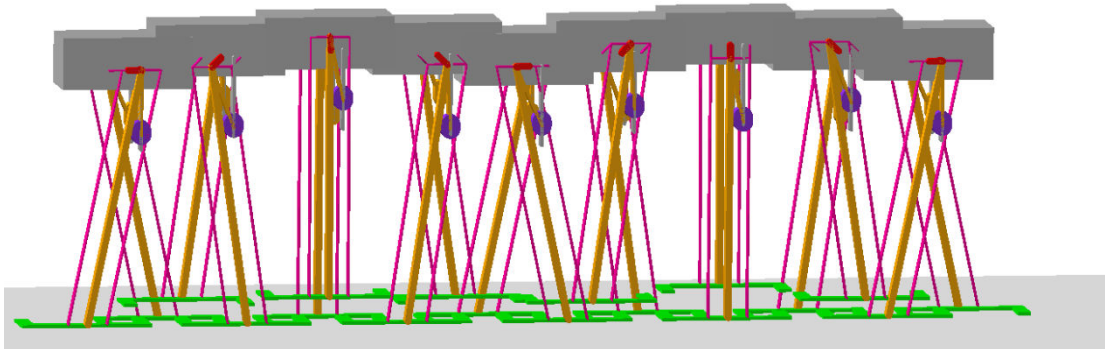
Simulations with different step lengths of the walking robot have been carried out via ADAMS. All the simulations have been carried out with the input rotational velocity of the input crank as 30 deg/s.

Figure 2-17 shows the snapshots of the animation of simulations while the robot is walking with different configurations of the leg mechanism. It can be seen that, for all the simulations, the robot can walk steadily and the distance between the two snapshots is increased when the offset of the glider is increased.

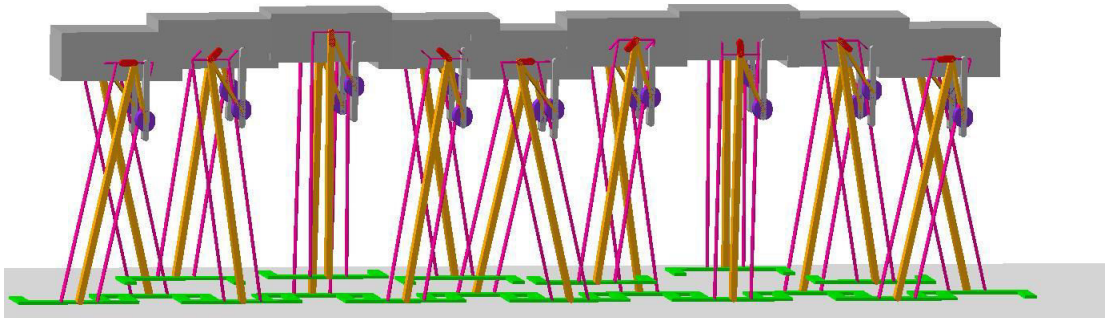
The horizontal displacement of the robot with different configurations is shown in Figure 2-18. For all the simulations, the robot can walk with a constant speed and the speed changes with the variation of the offset of the slider guide. Figure 2-19 shows the energy consumption of the robot while the leg in the different phase of gait cycle. It can be seen that during the swing phase (0-50% of the gait cycle), the energy consumption is very low since the energy is only used for moving the leg. And during the stand phase (50%-100%), the energy is used for actuating the robot to walk forward and the energy consumption is increased as the robot's walking speed is increased.



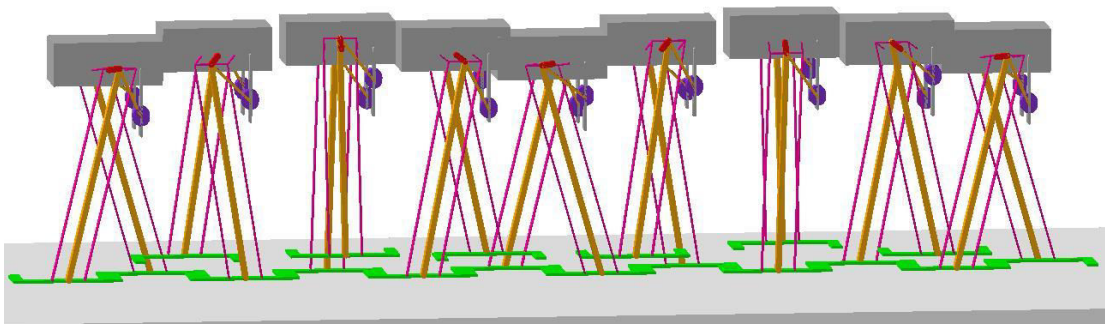
(a) gait 1



(b) gait 2



(c) gait 3



(d) gait 4

**Figure 2-17.** Snapshots of the simulations with different configuration.

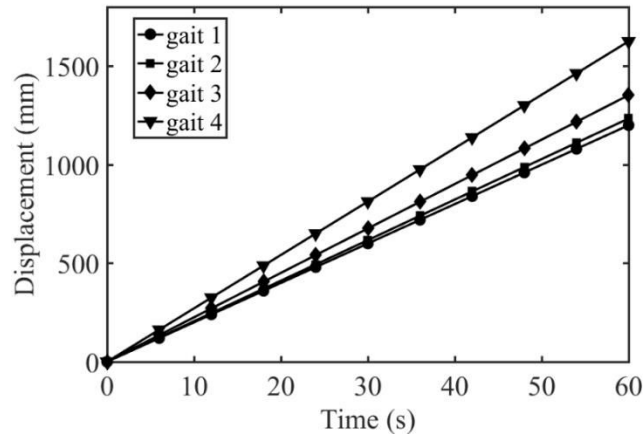


**Figure 2-18.** Horizontal displacement of the robot.

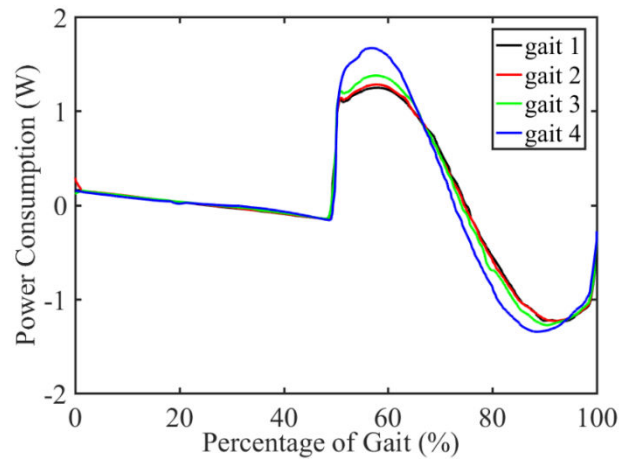


**Figure 2-19.** Energy consumption with respect to the phase of gait cycle.

## 2.3 Design and synthesis of a single actuator walking robot via coupling of the driven cam system and the pantograph mechanism

### 2.3.1 Introduction

The previous sections have shown that the single-actuator walking robots can walk steadily on the flat terrain. Thus, the leg mechanisms produce either a constant or variable step length.

In this section, a single actuator walking robot with the adjustable parameters for changing output gait is proposed. It allows not only to produce a walking motion on a horizontal surface but also to climb stairs.

### 2.3.2 Design of the walking robot with adjustable parameters

The proposed 1 DOF leg consists of a cam mechanism with a variable angle of inclination connected with a pantograph mechanism permitting to amplify the input motion. Two adjustable parameters are included in the proposed walking robot: an

angle of inclination of the cam mechanism permitting the robot to climb stairs and a pantograph mechanism having the possibility to be fixed in two different axes.

Figure 2-20 shows the motions of the proposed leg mechanism with two different points of fixation. As can be seen from Figure 2-20(a) and Figure 2-20(b), for the same input trajectories of the point C of the cam mechanism two output trajectories are produced.

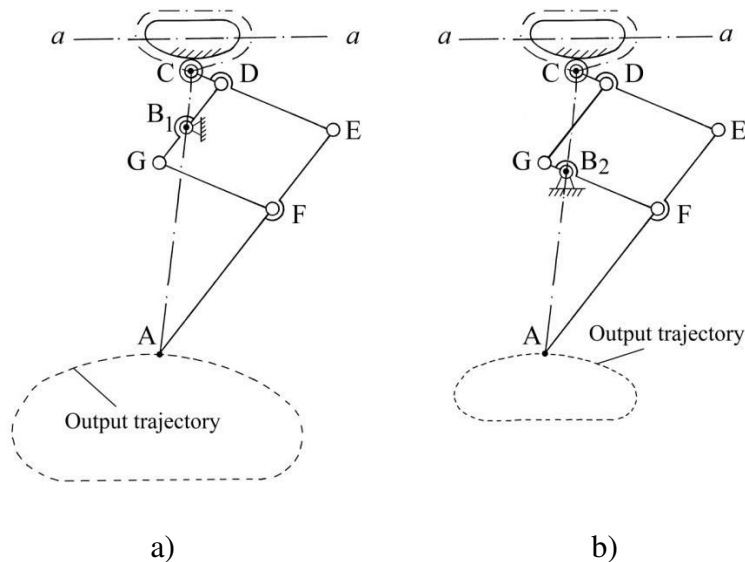


**Figure 2-20.** Leg mechanism with two output trajectories.

The pantograph mechanism is used to amplify the input trajectory of point C into the output trajectory with the same shape of point A. In the suggested design concept, the fixed point can be either  $B_1$  or  $B_2$ . Changing the position of the fixed point  $B_i$  ( $i=1$  or  $2$ ) on the body frame allows one to obtain two output trajectories with different magnitudes. The amplify ratio of the pantograph mechanism depends on the length of links. For the first case shown in Figure 2.20(a), the amplify ratio is  $k_1 = B_1A / B_1C$  and for the second case shown in Figure 2.20(b), the amplify ratio is  $k_2 = B_2A / B_2C$ . Thus, given the need of walking gait, two different possible steps can be produced with small or large stride length.

The choice of adjustable parameters  $B_i$  ( $i=1$  or  $2$ ) can be carried out taking into account the size of the obstacles and the imposed speed of walking.

The second adjustable parameter is the angle of inclination of the cam mechanism. The rotation of the axis  $a-a$  of the cam mechanism at an angle of  $\alpha$  (Figure 2-21) allows one to change the orientation of the input trajectory. Such an adjustment allows the walking robot to climb stairs. The value of the angle  $\alpha$  depends on the stair's parameters (height and width). Based on the stair's parameters, the walking robot can be adjusted with inclination angle  $\alpha$  as well as with small or large stride length.

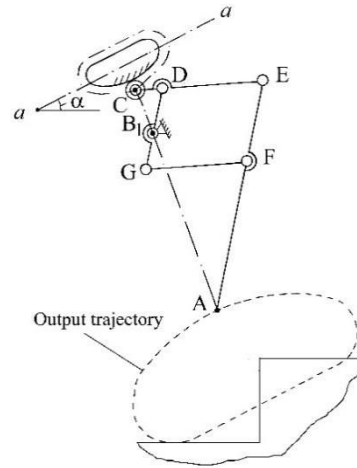


**Figure 2-21.** Leg mechanism with a rotated input cam mechanism.

To illustrate the efficiency of the suggested walking robot let us consider CAD simulations carried out via ADAMS software.

### 2.3.3 Properties of the proposed walking robot and its CAD model

The CAD model of the legged walking robot was created via CATIA software, Figure 2-22 shows the robot's body without the pantograph mechanisms. The robot's body includes a main body, two cams on each side which can rotate relative to the main body, two rolling balls were inserted into the profile of each cam, two rolling bars on each side, which rotate about the center of each cam. Two sliders link to the rolling balls on one side and link to the input point of pantograph mechanism on the other side and have translational motion with rolling bars.

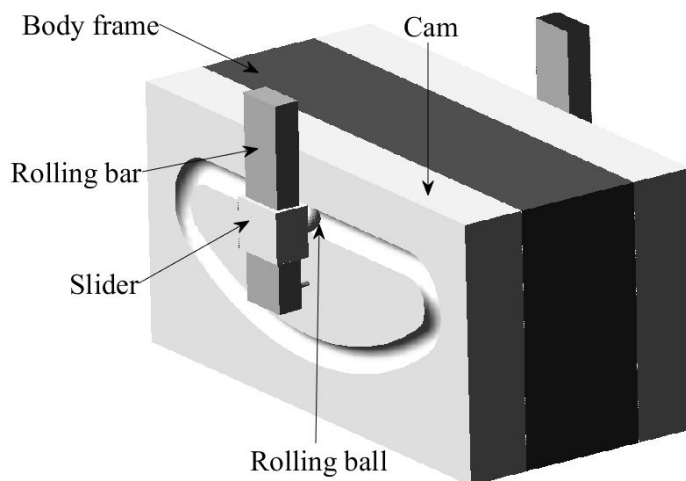


**Figure 2-22.** Robot's body without pantograph mechanism.

Once the CAD model had been built, it was imported to ADAMS and pantograph mechanism was created. And in order to keep the balance of the robot, a movable counterweight was added on the robot. The ADAMS model of the legged walking robot is shown in Figure 2-23. And Table 2-3 shows the geometrical coordinates of this

pantograph mechanism. For this pantograph mechanism, when  $B_1$  is the fixed point, the amplify ratio is 2, and when  $B_2$  is the fixed point, the amplify ratio is 1.

**Table 2-3.** Coordinates of the axes, input and output points of the pantograph mechanism.

Point	X(mm)	Y(mm)
A	0	-600
B <sub>1</sub>	0	-200
B <sub>2</sub>	0	-300
C	0	0
D	-100	-66.67
E	-300	-200
F	-150	-400
G	50	-266.67

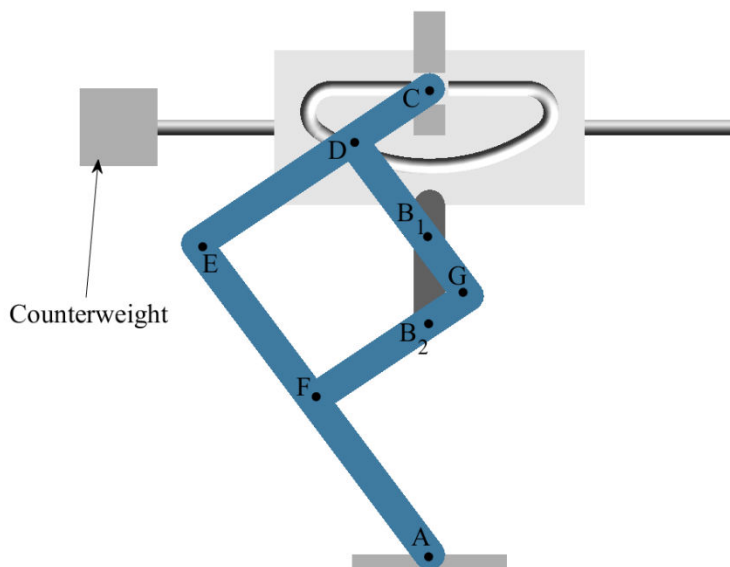


**Figure 2-23.** ADAMS model of the legged walking robot.

### 2.3.4 Simulation results

In order to validate the feasibility of the proposed walking robot, simulations via ADAMS have been conducted with different adjustable parameters and different environments.

First, two simulations were performed when the robot was walking on the plain road and the fixed point of the pantograph mechanisms was on  $B_1$  and  $B_2$  respectively. The

### 2.3 Design and synthesis of a single actuator walking robot via coupling of the driven cam system and the pantograph mechanism

same input motion speed was set for both of the simulations. Figure 2-24 shows the horizontal displacement with the fixed points on  $B_1$  or  $B_2$ . And the snapshots of the simulations are shown in Figure 2-25. It can be seen that, with different fixed positions, the walking robot can generate different gait with different length. And the power consumption of the actuator of the robot's left leg while walking on the plane road is shown in Figure 2-26. From 0 to 50% of the gait is corresponds to the stand phase and the rest is corresponds to the swing phase.

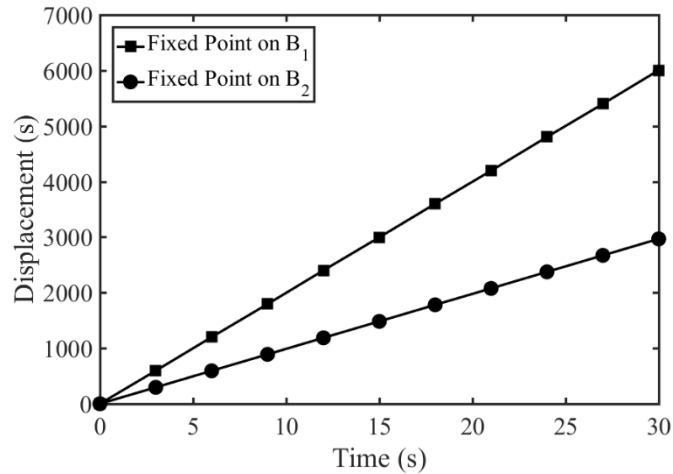


**Figure 2-24.** Horizontal displacement with fixed points:  $B_1$  and  $B_2$ .

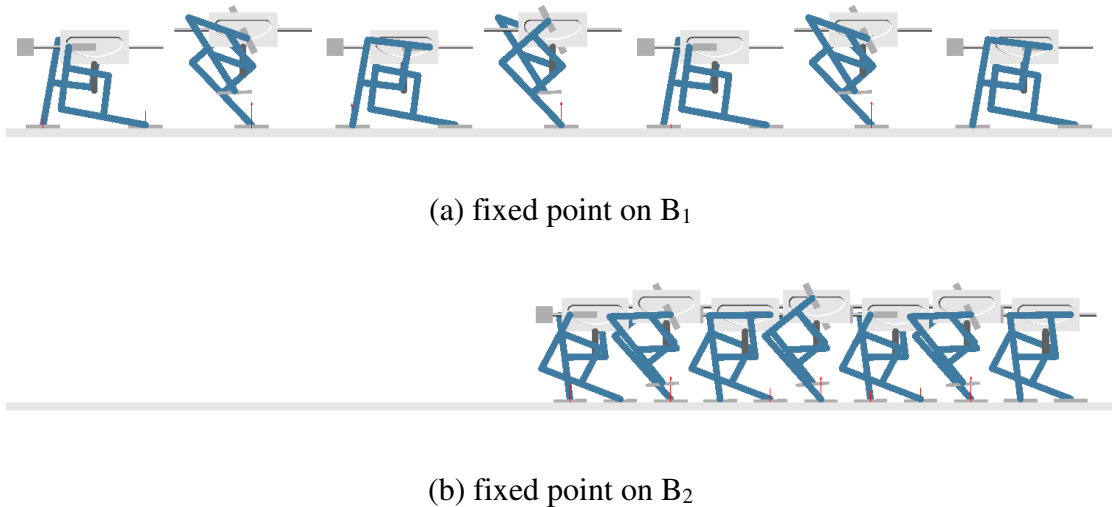


**Figure 2-25.** Snapshots of simulations with different fixed points of pantograph mechanism. (walking on plane surface)

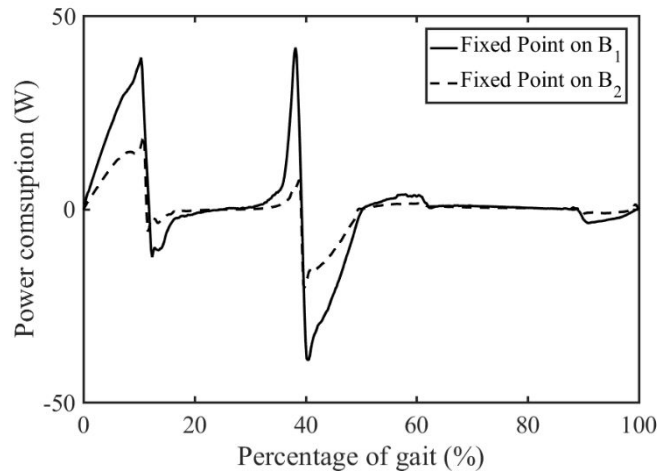


**Figure 2-26.** Power consumption of the actuator of the left leg when fixed point on B<sub>1</sub> and B<sub>2</sub> (walking on a plane surface)

The second set of two simulations were performed when the robot was climbing stairs. Similar to the previous simulations, the same input motion was executed on each side of the rolling bars, the angle between two cams and the body of the robot was adjusted to 20 deg. Figure 2-27 shows the horizontal and vertical displacements of the walking robot when the fixed point is on B<sub>1</sub> or B<sub>2</sub>. Figure 2-28 shows the snapshots the two simulations with different fixed points. It can be seen that, after changing the cam angle  $\alpha$ , the robots can generate tilted gaitis which allow them to climb stairs. Additionally, the change of fixed points of the pantograph mechanism allows the robot to climb different sizes of stairs. Figure 2-29 shows the power consumption of the actuator of the robot's left leg while climbing stairs.

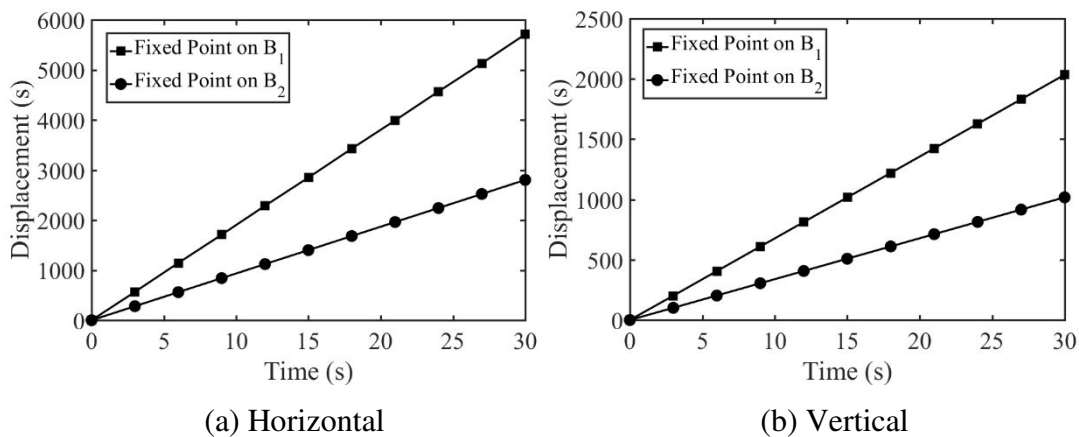
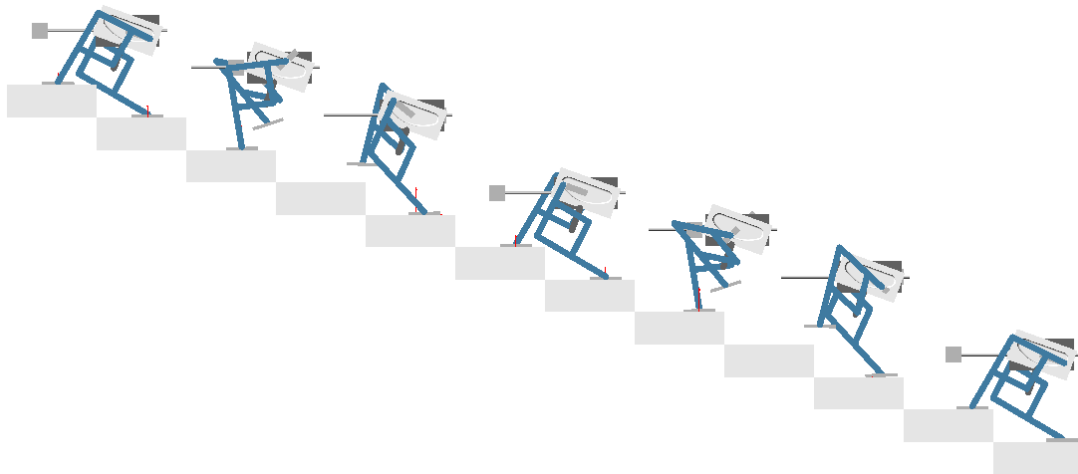
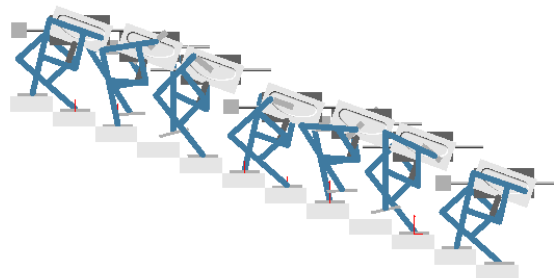


**Figure 2-27.** Horizontal and vertical displacement when the fixed point on B1 and B2





(a) fixed point on  $B_1$



(b) fixed point on  $B_2$

**Figure 2-28.** Snapshots of simulations with different fixed points of pantograph mechanism. (climbing stairs)

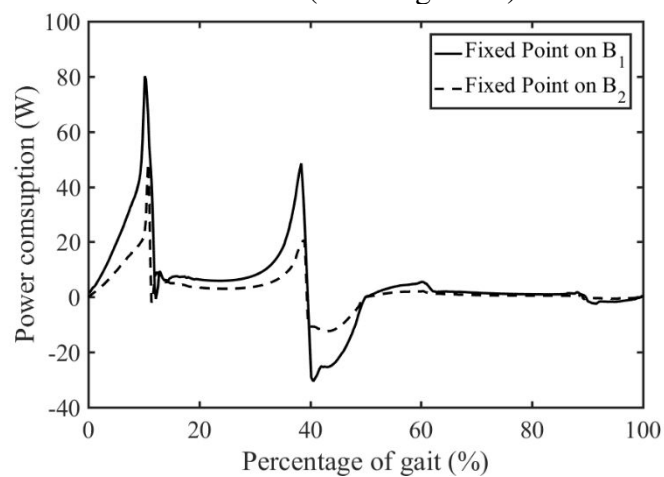


**Figure 2-29.** Power consumption of the actuator of the left leg when fixed point on  $B_1$  and  $B_2$  (climbing stairs)

## **2.4 Summary**

In this chapter, the various techniques of the design of single actuator walking robots have been considered. These designs were achieved via the coupling of different kinds of mechanisms.

In the first section, a walking robot with reduced degree of freedom has been designed based on a four-bar mechanism. In order to let the four-bar mechanism generate the desired trajectory, a mechanism synthesis based on the Genetic Algorithm has been developed. The proposed geometric synthesis of the four-bar linkage allows one to find the lengths of links that ensure the reproduction of prescribed points of the given trajectory. The suggested walking robot consist of a moving frame connected with two synthesized four-bar linkages. The actuator of the walking robot is mounted at the center of its moving frame and moves both legs. Simulation results showed that the robot is capable to walk steadily both forward and backward at different constant speeds.

However, such a robot can only generate a fixed gait pattern. Hence, in the next section, a 1 DOF robot with adjustable slider-crank mechanism has been proposed. The output trajectory of the suggested mechanism can be changed while changing the offset of the slider guide. The step length of the robot is exponentially increased when the slider guide is moving away from the fixed pivot. Simulations have been done with 4 different given combinations of adjustable parameters, and results showed that the robot can walk steadily for all the simulations.

To design a single actuator robot which has the ability of both walking on the plane surface and climbing up the stairs, the robot must generate a tilted gait for reaching higher/lower stair. In the last section, a 1 DOF legged walking robot using cam and pantograph mechanism with adjustable parameters is proposed. The adjustable parameters are the angle between the cam mechanism and the robot body and the fixed point position of the pantograph mechanism. Simulations were performed via ADAMS software. The obtained results showed that the change of fixed point position of the pantograph mechanism can significantly change the speeds of walking and climbing stairs, and it also can also change the power consumption. On the other hand, the variation of the angle between cams and the robot's body can let the robot be able to climb stairs, and the angle can be adjusted to adapt the slope of stairs.

# Design and synthesis of gravity balancers with coupled units

---

3.1	Design and synthesis of a balancer via coupling a rotating link through a dyad with revolute joints.....	62
3.2	Design and synthesis of a balancer via coupling a rotating link through a dyad with prismatic pair.....	67
3.3	Improved design of gravity compensators based on the inverted slider crank mechanism.....	74
3.4	Summary.....	83

---

*This chapter deals with the optimal design and synthesis of gravity balancers, which consist of a rotating link to be balanced and a two-link dyad. The proposed balancers use non-zero length springs.*

*In the design concept described in the first section, the balancing spring is connected with the rotating link by means of an articulated dyad forming a four-bar linkage. An optimization method based on the geometric synthesis of the four-bar mechanism and potential energy conservation is developed, which allows one to control the optimal displacement of the spring providing a suitable balancing moment.*

*The second section of the chapter deals with a similar problem by coupling a rotating link to be balanced with a dyad including a prismatic pair. The added dyad combining with the rotating link forms a slider-crank mechanism. The particularity of the suggested design concept is that the balancing spring is installed on the fixed frame, which allows one to reduce the errors due to the spring's weight. An optimization approach is applied to create a suitable balancing moment.*

*In the last section of the chapter, a balancer based on the inverted slider-crank mechanism is considered. It is proposed to use the minimization of the unbalanced moment by taking into account the mass of the added rocker and the spring.*

### ***3.1 Design and synthesis of a gravity balancer via coupling a rotating link and a dyad with revolute joints***

#### **3.1.1 Introduction**

As the literature review of gravity balancers mentioned in section 1.2, the use of counterweights is a simple and not expensive solution. However, it leads to an increase in the overall dimensions of manipulators, as well as to a substantial increase in inertia of links. Increasing the inertia of links is undesirable because this creates additional dynamic loads on the actuators that are not taken into account in static balancing, i.e. in balancing of gravitational forces.

Balancing by means of springs is one of the promising ways to balance the gravitational force of the robotic arm since it is easy to implement and does not need any further energy consumption. However, it is known that a conventional linear spring directly jointed with a rotating link cannot fully balance its gravitational forces. This requires the use of special springs called “zero free length springs” [43]. These springs are often applied in theoretical solutions, but they are very rare in real robotic structures.

One of the efficient ways to solve this problem is to add an auxiliary linkage to the rotating link thus increases the number of free parameters, allowing the optimization of the gravity balancing.

Various mechanisms and numerical optimization methods have been proposed in previous researches that have been reviewed in the first chapter. It is understandable that the use of numerical methods will lead to the minimization or cancellation of the unbalanced moment due to gravitational forces. However, it is still more attractive to find an analytically tractable solution that can be easily applied for the optimal design of the mechanism.

The aim of this section is to contribute to the development of new balancers with non-zero length springs. A gravity balancer via coupling a rotating link and a dyad with revolute joints has been designed. In addition, an analytically tractable solution based on the geometric synthesis of four-bar linkage and conservation of potential energy is developed.

#### **3.1.2 Design concept of a gravity compensator by creating a four-bar mechanism**

In the proposed design, shown in Figure 3-1, a dyad formed by links 3, 4 has been added and connected with the rotating link 2 to be balanced. It can be seen that the added dyad with original link 2 has formed a four-bar linkage OABC. To carry out the gravity balancing, a spring is installed between the frame and the link 4 (Figure 3-1).

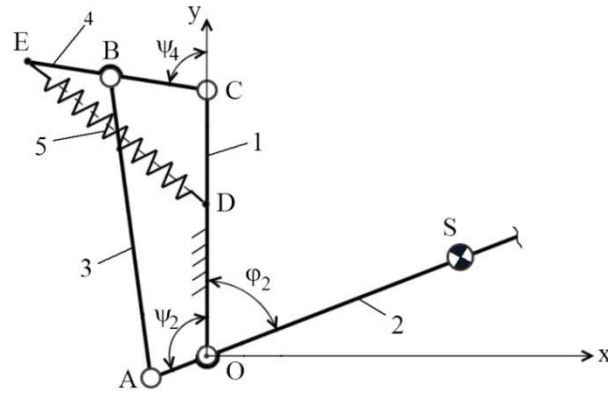


**Figure 3-1.** Gravity compensator with a four-bar linkage.

The created linkage brings new geometrical parameters, which can control the deformation of the spring. For achieving better balancing effect, optimization of these parameters is carried out in the next section.

### 3.1.3 Optimization of gravity balancer based on the geometric synthesis of four-bar linkage and potential energy conservation

#### a) Conservation of potential energy

At first, let us consider the balancing conditions from the conservation of potential energy.

The potential energy of gravity can be written as follows:

$$P_G = Gs(1 + \cos \varphi_2) \quad (3-1)$$

where  $G$  is the gravitational force of the rotating link 2;  $\varphi_2$  is the rotational angle of link 2 and  $s = l_{OS}$  is the distance between the center of mass of the link 2 and its center of rotation.

And the potential energy of the spring:

$$P_{sp} = \frac{1}{2} k \Delta l^2 \quad (3-2)$$

where,  $k$  is the stiffness coefficient of the spring and  $\Delta l$  is the deformation of the spring.

The whole potential energy of the system:

$$P = P_G + P_{sp} \quad (3-3)$$

where  $P_G$  denotes the gravitational potential energy of rotating link 2 and  $P_{sp}$  denotes the elastic potential energy of the spring.

It is known that the system will be balanced if:

$$\frac{dP}{d\varphi_2} = 0 \quad (3-4)$$

That means for every configuration of the system, the whole potential energy will remain as a constant  $C$ .

Hence for a  $C=\text{const}$ , the balancing condition can be expressed as:

$$Gs(1 + \cos \varphi_2) + \frac{1}{2}k\Delta l^2 = C \quad (3-5)$$

and for a given  $C$ , the determination of the spring will be:

$$\Delta l = \sqrt{\frac{2C - 2Gs(1 + \cos \varphi_2)}{k}} \quad (3-6)$$

Thus,  $l = l_0 + \Delta l$ , where  $l_0$  is the initial length of the spring.

The angle  $\angle OCB$  (see in Figure 3-1) of the four-bar mechanism OABC can be represented by the expression:

$$\angle OCB = \arccos \left[ \frac{a^2 + (l_1 - b)^2 - l^2}{2a(l_1 - b)} \right] \quad (3-7)$$

where,  $a = l_{CE}$  is the distance between the centers of joints  $C$  and  $E$ ;  $l_1$  is the distance between fixed pivots  $O$  and  $C$ ;  $b$  is the distance between fixed pivots  $O$  and  $D$ .

The output angle  $\psi_4$  of the four-bar mechanism OABC is:

$$\psi_4 = 180^\circ - \angle OCB \quad (3-8)$$

Hence, by imposing  $C$  and  $\varphi_2^{(i)}$ , where  $i=1, \dots, n$  is the number of given positions of the rotating link 2, the output angles  $\psi_4^{(i)}$  can be determined. In another word, for a balanced system, the output angles  $\psi_4^{(i)}$  is determined by given position of link 2 and constant potential energy  $C$ .

### b) Synthesis of four-bar mechanism

Let us denote the lengths of links of the four-bar mechanism OABC as follows:  $l_1=l_{OC}$ ,  $l_2=l_{OA}$ ,  $l_3=l_{AB}$  and  $l_4=l_{BC}$ . For the proposed geometric synthesis, it is better to use non-dimensional lengths of links. Thus, admitting  $L_1=l$ , the lengths of three other links are  $L_2=l_2/l_1$ ,  $L_3=l_3/l_1$  and  $L_4=l_4/l_1$ .

According to the geometrical relationship of the quadrilateral ABCD [116], we can get:

$$A^* \cos \psi_4 + B^* \cos \psi_2 + C^* = \cos(\psi_4 - \psi_2) \quad (3-9)$$

where,  $A^* = 1/L_2$ ,  $B^* = 1/L_4$ ,  $C^* = (1 + L_2^2 + L_4^2 - L_3^2) / 2L_2L_4$ ,  $\psi_2$  and  $\psi_4$  are shown in Figure 3-1.

Let us now consider the synthesis of the balancing mechanism for 3 prescribed positions. For three given input angles  $\psi_2^{(1)}, \psi_2^{(2)}, \psi_2^{(3)}$  and three given output angles  $\psi_4^{(1)}, \psi_4^{(2)}, \psi_4^{(3)}$ , we will have:

$$\begin{bmatrix} \cos \psi_4^{(1)} & \cos \psi_2^{(1)} & 1 \\ \cos \psi_4^{(2)} & \cos \psi_2^{(2)} & 1 \\ \cos \psi_4^{(3)} & \cos \psi_2^{(3)} & 1 \end{bmatrix} \begin{bmatrix} A^* \\ B^* \\ C^* \end{bmatrix} = \begin{bmatrix} \cos(\psi_4^{(1)} - \psi_2^{(1)}) \\ \cos(\psi_4^{(2)} - \psi_2^{(2)}) \\ \cos(\psi_4^{(3)} - \psi_2^{(3)}) \end{bmatrix} \quad (3-10)$$

It can be seen that with three pairs of  $\psi_2$  and  $\psi_4$ , by solving eq. (3-10), we can get the value of  $A^*$ ,  $B^*$ ,  $C^*$  and the non-dimensional lengths of four-bar mechanism ABCD. Then, with given length of fixed link  $l_1$ , the real lengths of other links  $l_2$ ,  $l_3$  and  $l_4$  can be obtained. For the case with more than three prescribed, numerical methods like the least square method can be used for approximately solving the equations.

### c) Parameter optimization of the balancing mechanism

Although we know that for a balanced mechanism, its total potential energy stays constant, however, the value of this total potential energy is unknown. In order to determine this value, let us first consider the moments of the balancing mechanism generated by the gravity of the link 2 and the spring 5.

The moment produced by the gravity of the rotating link 2 with respect to pivot O is:

$$M_G = -Gs \sin \varphi_2 \quad (3-11)$$

According to the geometrical relationship of triangle  $CDE$ , we can get the length of spring  $l$ :

$$l = a^2 + (l_1 - b)^2 + 2a(l_1 - b) \cos \psi_4 \quad (3-12)$$

Then we can get the elastic force of the spring  $F_{sp}$ :

$$F_{sp} = k(l - l_0) \quad (3-13)$$

According to the geometric relationship of the mentioned triangle, we get:

$$\theta = \arccos \left[ \frac{a^2 + l^2 - (l_1 - b)^2}{2al} \right] \quad (3-14)$$

$$\varphi_3^* = \arccos \left[ \frac{l_3^2 + l_4^2 - (l_1^2 + l_2^2 - 2l_1l_2 \cos(\pi - \varphi_2))^2}{2l_3l_4} \right] \quad (3-15)$$

$$\varphi_3 = \arccos \left[ \frac{l_2^2 + l_3^2 - (l_1^2 + l_4^2 + 2l_1l_4 \cos \psi_4)^2}{2l_2l_3} \right] \quad (3-16)$$

where  $\theta = \angle CED$ ,  $\varphi_3^* = \angle CBA$  and  $\varphi_3 = \angle BAO$ .

Thus, the force acting on the rotation link 2 through link 3 will be:

$$F_{ab} = \frac{F_{sp} a \sin \theta}{l_4 \sin \varphi_3^*} \quad (3-17)$$

The moment produced by the elastic force of the spring acting on the rotating link 2 through the four-bar mechanism OABC is:

$$M_{sp} = F_{ab} l_2 \sin \varphi_3 \quad (3-18)$$

Hence the unbalanced moment of the whole system is:

$$M_{ub} = M_{sp} + M_G \quad (3-19)$$

And the total unbalanced moment for all the prescribed positions is:

$$M_{ub}^{total} = \sum_{\varphi=\varphi_i} M_{ub}(\varphi, l_2, l_3, l_4) \quad (3-20)$$

From the previous part, it has been seen that the values of  $l_2$ ,  $l_3$  and  $l_4$  depend on input angles and their corresponding output angles of the four-bar mechanism. And the output angles depend on the prescribed position of link 2 and the constant potential energy C. Hence the total unbalanced moment  $M_{ub}^{total}$  can be described as a function of prescribed positions and constant potential energy. However, taking into account that the prescribed positions are given, the single variable of the total unbalanced moment  $M_{ub}^{total}$  is C.

For minimizing the total unbalanced moment, the following condition should be satisfied for given configurations of the four-bar linkage:

$$\frac{\partial M_{ub}^{total}}{\partial C} = 0 \quad (3-21)$$

Thus, by solving eq. (3-21), the constant potential energy C can be calculated and then the optimal parameters  $l_2$ ,  $l_3$  and  $l_4$  of the balancing mechanism can be determined as it was disclosed above.



### 3.1.4 Illustrative example with simulation results

Firstly, the balancing via 3 prescribed positions of the rotating link 2 is considered. The initial parameters of the rotating link and the spring are the following:  $k=8000N/m$ ,  $l_0=0.98m$ ,  $G=63N$  and  $s=0.5m$ . The parameters with respect to the spring position and length of fixed link are  $a=1m$ ,  $b=0.8m$  and  $l_1=1m$ . Three prescribed positions of the rotating link are the following:  $\varphi_2^{(1)}=30^\circ$ ,  $\varphi_2^{(2)}=90^\circ$  and  $\varphi_2^{(3)}=150^\circ$ . These positions can be any others. The stages of the solution will be the same.

From Eq. (3-21), the constant potential energy has been determined:  $C=197$ . Thus, by solving the system of linear equations (3-10), three unknown parameters have been determined:  $l_2= 0.019m$ ;  $l_3= 1.175m$  and  $l_4= 0.193m$ . With these parameters, the moment of the gravitational forces before balancing and the remaining moment after balancing are shown in Figure 3-2 and Figure 3-2.

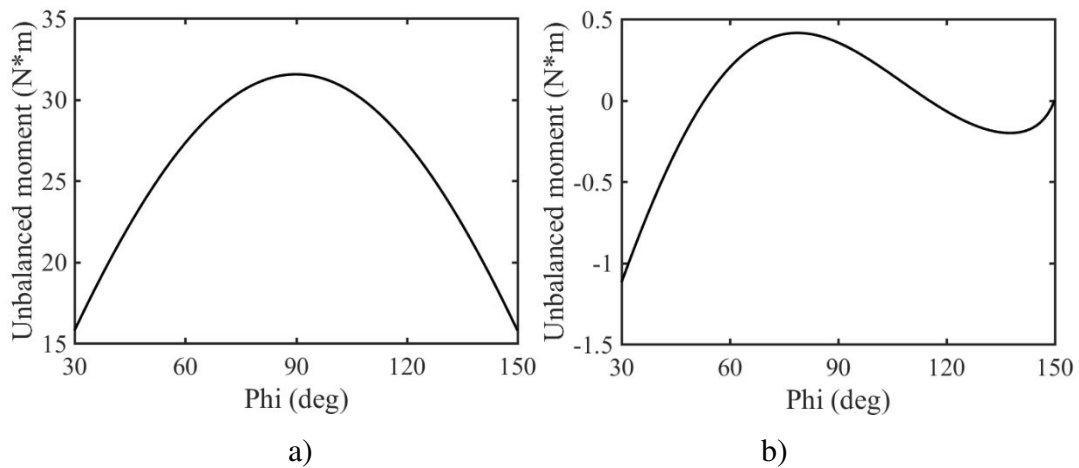


**Figure 3-2.** Moment of the gravitational forces before balancing (a) and the remaining moment after balancing (b).

The obtained results show that the maximum absolute value of the remaining moment after balancing is 1.11 Nm. Thus, 98 % reduction in the gravity forces is achieved.

The same example has been simulated for 120 positions between angle 30° and 150°, i.e. with a step of one degree. However, the obtained results showed that the improvement of the balancing quality is insignificant (less than 1%).

## 3.2 Design and synthesis of a gravity balancer via coupling a rotating link and a dyad with a prismatic pair

### 3.2.1 Introduction

In the previous section, a gravity balancer via coupling a rotating link and a dyad with revolute joints has been considered.

Let us now consider the design and synthesis of a gravity balancer via coupling a rotating link and a dyad with a prismatic pair. Note that the choice of fixed installation of spring is due not only to constructive practicality but also to the fact that the mass of

the spring does not affect the balancing conditions of the rotating link. An optimization method of the geometric parameters of the dyad is proposed, which is similar to the approach examined in the previous section.

### 3.2.2 Design concept of a gravity compensator by creating a slider-crank mechanism

In the proposed gravity balancer, shown in Figure 3-3, the axis B moving by the rotation link 2 through the cable 3, controls the elastic force of the spring 5 mounted between the slider 4 and the fixed frame 1.

Comparing to the design in the previous section, the proposed design has many advantages. For example, the weight of spring will not distort the balancing effect. And because the spring force is single-directionally transmitted to the rotating link, a cable can be used for the force transmission rather than much heavier rigid rod.

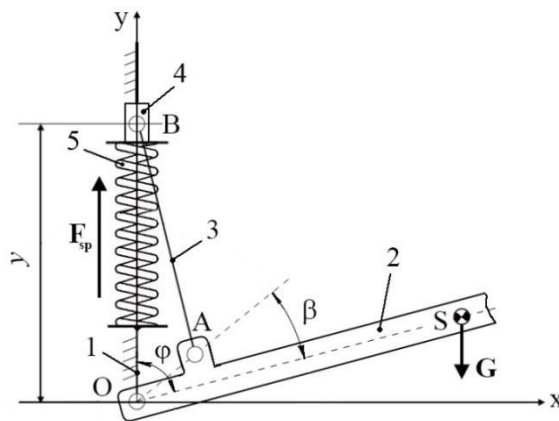


**Figure 3-3.** Gravity compensator by forming a crank-slider mechanism.

As in the previous case, for achieving the optimal balancing result, optimization of the geometrical parameters of the slider-crank mechanism OAB should be carried out.

### 3.2.3 Optimization of gravity balancer based on geometric synthesis of slider-crank mechanism and potential energy conservation

#### a) Conservation of potential energy

Similar to the optimization method proposed in the previous section, let us first consider the balancing condition with respect to the potential energy.

The potential energy of the gravity of the rotating link 2 can be expressed as:

$$P_G = Gs(1 + \cos \varphi) \quad (3-22)$$

where,  $G$  is the gravitational force of the rotating link 2;  $\varphi$  is the rotating angle of the link 2 and  $s = l_{OS}$  is the distance between the center of mass of the link 2 and its center of rotation.

The potential energy of the spring is:

$$P_{sp} = \frac{1}{2}k\Delta y^2 \quad (3-23)$$

where,  $\Delta y$  is the deformation of the spring and  $k$  is its stiffness coefficient.

The whole potential energy of the system is:

$$P = P_G + P_{sp} \quad (3-24)$$

As it was mentioned in the previous section, the system will be balanced if:

$$\frac{dP}{d\varphi} = 0 \quad (3-25)$$

This means, for all the configurations of the system, the whole potential energy will remain as a constant.

Hence for a  $C = \text{const}$ , we can have:

$$Gs(1 + \cos \varphi) + \frac{1}{2}k\Delta y^2 = C \quad (3-26)$$

and for a given  $C$  determine

$$\Delta y = \pm \sqrt{\frac{2C - 2Gs(1 + \cos \varphi)}{k}} \quad (3-27)$$

and

$$y = \Delta y + l_0 \quad (3-28)$$

where  $l_0$  is its initial length of the spring.

Thus, by imposing  $C$  and  $\varphi_i (i = 1, \dots, n)$ , where  $n$  is the number of given positions of the rotating link, the displacements  $y_i$  with respect to each input angle  $\varphi_i$  can be determined.

### **b) Synthesis of the balancing mechanism for prescribed positions of the rotating link**

For the balancing mechanism showed in Figure 3-3, there are three main parameters  $r$ ,  $l$  and  $\beta$ , where,  $r = l_{OA}$  is the distance between the centers of joints  $O$  and  $A$ ;  $y$  is the

position of the axis  $B$  with respect to  $O$ ;  $l = l_{AB}$  is the length of the rod 3;  $\beta$  is the angle between the axes created by the line passing through the centers  $O$  and  $A$ , and the line passing through the centers  $O$  and  $S$  (see Figure 3-3).

In this section, with the prescribed positions, geometric synthesis is used to determine the parameters  $r$ ,  $l$ , and  $\beta$ .

For the mechanism  $OAB$ , we have

$$(y_i - r \cos(\varphi_i - \beta))^2 + r^2 \sin(\varphi_i - \beta)^2 = l^2 \quad (3-29)$$

or

$$y_i^2 - 2y_i r \cos(\varphi_i - \beta) + r^2 = l^2 \quad (3-30)$$

Eq. (3-30) can be rewritten as:

$$y_i^2 - 2y_i r (\cos \varphi_i \cos \beta + \sin \varphi_i \sin \beta) = l^2 - r^2 \quad (3-31)$$

or

$$y_i^2 - 2y_i r \cos \varphi_i \cos \beta - 2y_i r \sin \varphi_i \sin \beta = l^2 - r^2 \quad (3-32)$$

Let's introduce new unknowns, which will allow one to transform the non-linear system of eq. (3-32) to a linear system of equations:

$$z_1 = r \cos \beta \quad (3-33)$$

$$z_2 = r \sin \beta \quad (3-34)$$

$$z_3 = l^2 - r^2 \quad (3-35)$$

Now, the obtained linear system of equations is the following:

$$y_i^2 - 2y_i \cos \varphi_i z_1 - 2y_i \sin \varphi_i z_2 - z_3 = 0 \quad (3-36)$$

or

$$a_i z_1 + b_i z_2 + z_3 = c_i \quad (3-37)$$

where,  $a_i = 2y_i \cos \varphi_i$ ,  $b_i = 2y_i \sin \varphi_i$  and  $c_i = y_i^2$ .

Thus, the unknowns  $r$ ,  $l$ , and  $\beta$  can be determined by:

$$\beta = \arctan \left( \frac{z_2}{z_1} \right) \quad (3-38)$$

$$r = \frac{z_2}{\sin \beta} = \frac{z_1}{\cos \beta} \quad (3-39)$$

$$l = \sqrt{z_3 + r^2} \quad (3-40)$$

### c) Parameter optimization of the balancing mechanism

The moment produced by the gravity of the rotating link 2 is

$$M_G = -Gs \sin \varphi \quad (3-41)$$

From  $OAB$  triangle can be written:

$$r^2 + y^2 - l^2 = 2ry \cos(\varphi - \beta) \quad (3-42)$$

Rearranging eq. (3-42) gives the following relationship:

$$y^2 - 2ry \cos(\varphi - \beta) + r^2 [\cos^2(\varphi - \beta) + \sin^2(\varphi - \beta)] = l^2 \quad (3-43)$$

and

$$[y - r \cos(\varphi - \beta)]^2 = l^2 - r^2 \sin^2(\varphi - \beta) \quad (3-44)$$

Hence the displacement of the slider 4 is:

$$y = r \cos(\varphi - \beta) + \sqrt{l^2 - r^2 \sin^2(\varphi - \beta)} \quad (3-45)$$

Thus, spring force  $F_{sp}$  will be:

$$F_{sp} = k(y - l_0) \quad (3-46)$$

Therefore, the component of spring force  $F_{sp}$  acting on the rod 3 is:

$$F_{ab} = F_{sp} \cos \theta \quad (3-47)$$

where,  $\theta = \angle OBA$  :

$$\theta = \arccos \left[ \frac{y^2 + l^2 - r^2}{2yl} \right] \quad (3-48)$$

The moment generated by the spring force through the rod 3 is:

$$M_{sp} = F_{ab} r \sin \psi \quad (3-49)$$

where,  $\psi = \angle BAO$  :

$$\psi = \arcsin \left[ \frac{y \sin(\varphi - \beta)}{l} \right] \quad (3-50)$$

Thus, the unbalanced moment of the whole system is:

$$M_{ub} = -(M_{sp} + M_G) \quad (3-51)$$

The total unbalanced moment for all the prescribed positions is:

$$M_{ub}^{total} = \sum_{\varphi=\varphi_i} M_{ub}(\varphi, l, r, \beta) \quad (3-52)$$

From the previous part, it can be seen that the values of  $l$ ,  $r$  and  $\beta$  depend on input angles and their corresponding slider's positions. And the slider's positions depend on the input angles and the constant potential energy  $C$ . Hence the total unbalanced moment  $M_{ub}^{total}$  can be described as a function of input angles and constant potential energy. Taking into account that the input angles are prescribed, the only variable of the function  $M_{ub}^{total}$  is  $C$ .

For minimizing the total unbalanced moment, the following condition should be satisfied for given configurations of the gravity balancer:

$$\frac{\partial M_{ub}^{total}}{\partial C} = 0 \quad (3-53)$$

By solving Eq. (3-53), the constant potential energy  $C$  can be calculated and then the optimal parameters  $l$ ,  $r$  and  $\beta$  of the gravity balancer can be determined.

### 3.2.4 Illustrative examples with simulation results

**Balancing via 3 prescribed positions of the rotating link.** The initial parameters of the rotating link and the spring are the following:  $k = 1000\text{N/m}$ ,  $l_0 = 1\text{m}$ ,  $G = 75\text{N}$  and  $s = 0.84\text{m}$ . Three prescribed positions of the rotating link 2 are the following:  $\varphi_1 = 30^\circ$ ,  $\varphi_2 = 60^\circ$  and  $\varphi_3 = 150^\circ$ .

From Eq. (3-53), the constant potential energy has been determined:  $C=184$ . Thus, by solving the system of linear equations (3-37) and taking into account relationships in eq. (3-38) – (3-40), the three unknown parameters have been determined:  $r = 0.132\text{m}$ ;  $l = 0.526\text{m}$  and  $\beta = -0.662^\circ$ .

With these parameters, the moment of the gravitational forces before balancing and the remained moment after balancing are shown in Figure 3-4a and Figure 3-4b.

### 3.2 Design and synthesis of a gravity balancer via coupling a rotating link and a dyad with a prismatic pair

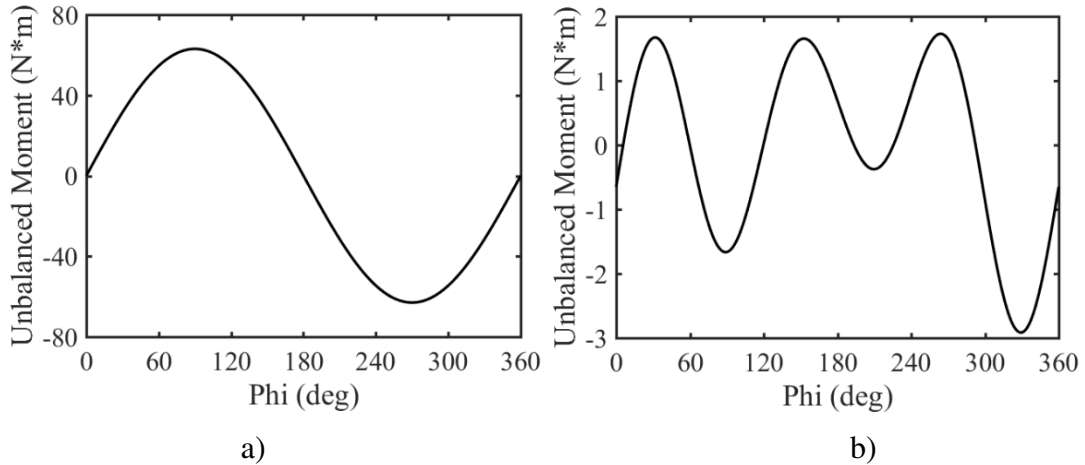


**Figure 3-4.** Moment of the gravitational forces before balancing (a) and the remained moment after balancing (b).

As we can see from these figures, via the proposed gravity compensation solution, the maximum value of the unbalanced moment has been reduced from 63 Nm to 2.92 Nm, i.e. 95.37%.

**Balancing via  $n$  prescribed positions of the rotating link.** The initial parameters of the rotating link and the spring are the following:  $k = 1000\text{N/m}$ ,  $l_0 = 1\text{m}$ ,  $G = 75\text{N}$  and  $s = 0.84\text{m}$ . The prescribed locations of the rotating link 2 were given for  $n = 120$  positions between angles  $30^\circ$  and  $150^\circ$ , i.e. with a step of one degree.

In this case:  $C=195$  and the following parameters of the crank-slider mechanism have been obtained:  $r = 0.125\text{m}$ ;  $l = 0.502\text{m}$  and  $\beta = 0.08^\circ$ .

With these parameters, the moments of the gravitational forces before and after balancing have shown in Figure 3-5a and Figure 3-5b.

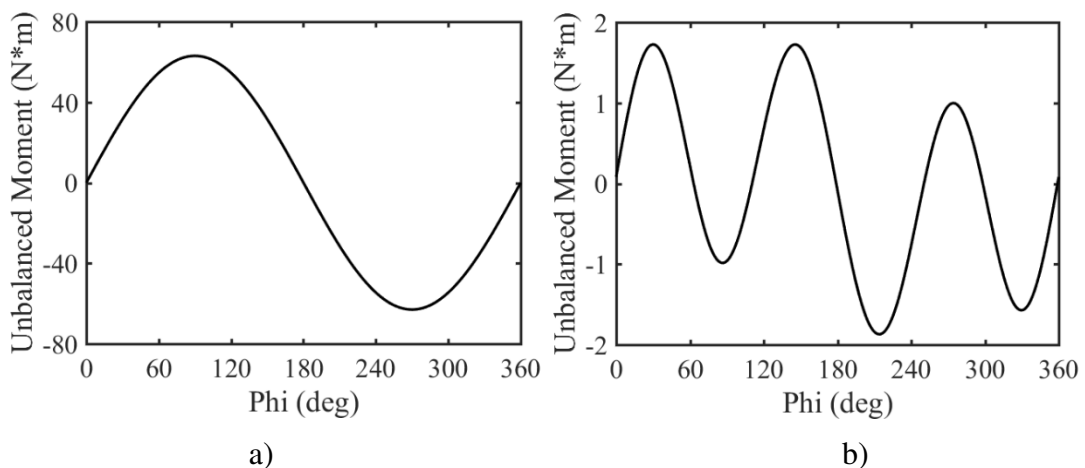


**Figure 3-5.** Moment of the gravitational forces before balancing (a) and the remained moment after balancing (b).

The obtained results show that the maximum value of the unbalanced moment quite small, about 1.87 Nm, which is better than the three given position case. The reduction of the moment of the gravitational forces is 97.03%.

Thus, one can state with certainty that a quasi-perfect balancing has been achieved.

### ***3.3 Improved design of gravity compensators based on the inverted slider crank mechanism***

#### **3.3.1 Introduction**

As mentioned in the literature review in section 1.2, in many cases the masses of the auxiliary links and springs used for gravity balancing are mainly neglected because they are considered much lighter than the principal rotating link. However, it does not always correspond to reality and for many balancing schemes it is the source of errors.

For diminishing these errors, in the previous section, an idea of installing spring on the fixed frame and replacing the rigid links by much lighter cables have been considered. In this section, the mass of auxiliary links and the spring will be taken into account in the design of gravity balancer based on the inverted slider crank mechanism. This structure can be obtained via coupling a rotating link and a dyad with a prismatic pair. However, it is different from the system examined in the previous section by forming a slider-crank mechanism. In this case, an inverted slider crank mechanism is created. Such a gravity balancer is known [117]. In the present section, the design of this mechanism will be considered taking into account the mass of the added dyad and the spring.

For this purpose, the torques due to auxiliary links are determined. Then, they are introduced into the balancing equation for minimization of the residual unbalance. In this way, a more accurate balancing of gravity compensators is achieved. The efficiency of the suggested approach is illustrated by numerical simulations.

#### **3.3.2 Improvement of the balancing accuracy by taking into account the masses of auxiliary links coupled with the rotating arm**

The gravity compensator based on the inverted slider crank mechanism is shown in Figure 3-6 [117].

Firstly, let us consider the balancing via an inverted slider crank mechanism without the gravitational forces of auxiliary links.



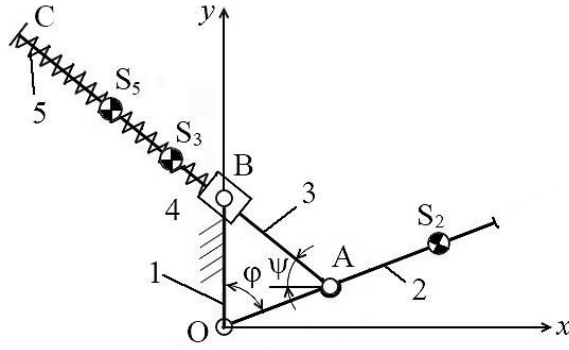


**Figure 3-6.** Gravity compensator based on the inverted slider crank mechanism.

The equation for a fully balanced system can be written as follows:

$$M_{sp} + M_G = 0 \quad (3-54)$$

where,  $M_{sp}$  is the moment produced by the elastic force of the spring;  $M_G$  is the moment produced by the gravity of the rotating link 2.

The moment produced by the elastic force of the spring can be written as follows:

$$M_{sp} = F_{sp} h \quad (3-55)$$

with

$$F_{sp} = -kx = -k(l_0 - l) \quad (3-56)$$

and

$$h = (l_{OA} l_{OB} / l_{AB}) \sin \varphi \quad (3-57)$$

where,  $F_{sp}$  is the elasticity force of the spring 5;  $h$  is its lever arm, i.e. the straight line perpendicular to the axis of the coupler 3 and passing through the center of the joint  $O$ ;  $\varphi$  is the rotating angle of the link 2;  $k$  is the stiffness coefficient of the spring,  $x$  is the deformation of the spring;  $l$  is the length of the spring at current angle  $\varphi$ ;  $l_0$  is the initial length of the spring,  $l_{OA}$  is the distance of the center of joint  $A$  from axis  $O$ ;  $l_{OB}$  is the distance of the centre of joint  $B$  from axis  $O$ ;  $l_{AB}$  is the distance between the centres of joints  $A$  and  $B$ .

Considering that the moment produced by the gravity of the rotating link 2 is the following:

$$M_G = m_2 g l_{OS_2} \sin \varphi \quad (3-58)$$

the balancing condition Eq. (3-54) can be rewritten as:

$$kl_{OA}l_{OB}(l_0 - l)/l_{AB} = m_2gl_{OS_2} \quad (3-59)$$

where,  $m_2$  is the mass of the rotating link 2;  $l_{OS_2}$  is the distance of gravity center of the rotating link 2 from axis  $O$ ;  $g$  is the gravitational acceleration.

This implies that when  $x = l_0 - l = l_{AB}$ , the complete balancing of gravitational forces can be reached by the choice of the stiffness coefficient of spring 5:

$$k = m_2gl_{OS_2}/l_{OA}l_{OB} \quad (3-60)$$

It is quite a simple solution since the masses of the coupler 3 and the spring 5 have been neglected. To improve the balancing accuracy, the masses of associated links must be taken into account.

First of all, it should be noted that the length of the link 3 is considerably large. This is due to the fact that the working zone of the spring 5 cannot exceed 30-40% of its initial length. Thus, the design of a gravity compensator with reasonable lengths  $l_{OA}$  and  $l_{OB}$  produces a spring that is fairly long. Therefore, in certain cases, it is advisable to take into account the mass of the link 3 and the spring 5. With regards to the rotating slider 4, its center of mass can be on the axis  $B$  and will not influence the balance of the system.

It is conspicuous that the masses of the associated link 3 can be balanced by adding counterweights or supplementary springs. However, this will complicate the design of the load balancer. Hence, this study examines the gravitational compensation via an inverted slider crank mechanism without supplementary means of balancing or cables with pulleys, i.e. without modification of the initial structure of the gravity compensator.

In Figure 3-7 that presents the active and reactions forces on the coupler 3 due to its mass and the spring's mass, four unknown bearing force components can be observed:  $R_{23}^x, R_{23}^y, R_{43}^x$  and  $R_{43}^y$ , which are the reactions of links  $j$  ( $j=2,4$ ) on coupler 3 in the  $x$  and  $y$  directions respectively. Since the directions of the reactions are unknown, we take them to the positive side [118]. After determining the value of reactions, it will help to direct the corresponding vectors correctly.

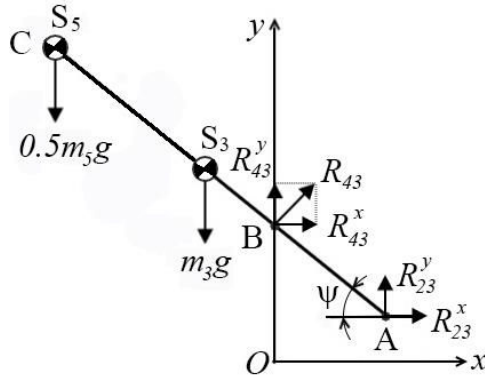


**Figure 3-7.** Active and reaction forces due to the gravitational forces of auxiliary links.

It should be noted that the spring 5 is attached to links 3 and 4. Therefore, the spring's mass  $m_5$  can be substituted by two concentrated spring  $m_{C5} = 0.5m_5$  and  $m_{B5} = 0.5m_5$ . The first  $m_{C5}$  is located at the end of the link 3 and the second  $m_{B5}$  is located at the axis  $B$  of the slider 4.

Thus, the moment with respect to the axis  $A$  can be written:

$$R_{43}l_{AB} - (m_3l_{AS_3} + 0.5m_5l_{AC})g \cos\psi = 0 \quad (3-61)$$

where,  $m_3$  is the mass of the coupler 3;  $m_5$  is the mass of the spring 5;  $l_{AS_3}$  is the distance of gravity center  $S_3$  of the coupler 3 from the joint center  $A$ ;  $l_{AC}$  is the distance of the axis  $C$  from the joint center  $A$ ;  $\psi$  is the angle defining the angular position of the coupler 3, determined from  $\Delta OAB$  (Figure 3-6):

$$\psi = \varphi - \pi/2 + \sin^{-1} \left[ \frac{l_{OB} \sin \varphi}{l_{AB}} \right] \quad (3-62)$$

with

$$l_{AB} = \sqrt{l_{OA}^2 + l_{OB}^2 - 2l_{OA}l_{OB} \cos \varphi} \quad (3-63)$$

From equation (3-61), the reaction  $R_{43}$  can be found:

$$R_{43} = \left[ (m_3l_{AS_3} + 0.5m_5l_{AC})g \cos\psi \right] / l_{AB} \quad (3-64)$$

Then, the reaction components:

$$R_{43}^x = R_{43} \sin\psi \quad (3-65)$$

and

$$R_{43}^y = R_{43} \cos \psi \quad (3-66)$$

The following reaction components can be found from the equilibrium equations on the coupler 3:

$$R_{23}^x = -R_{43}^x \quad (3-67)$$

and

$$R_{23}^y = (m_3 + 0.5m_5)g - R_{43}^y \quad (3-68)$$

Now, taking into account that  $R_{32}^x = -R_{23}^x$  and  $R_{32}^y = -R_{23}^y$ , the torque due to the gravity of the coupler 3 and the spring 5 can be determined:

$$\Delta M = R_{23}^y l_{OA} \sin \varphi - R_{23}^x l_{OA} \cos \varphi \quad (3-69)$$

or

$$\Delta M = l_{OA} \left[ R_{43} \sin(\psi - \varphi) + (m_3 + 0.5m_5)g \sin \varphi \right] \quad (3-70)$$

So, the balancing condition taking into account the added moment  $\Delta M$  can be written as:

$$M_{unb} = M_G + M_{sp} + \Delta M = \left( m_2 g l_{OS_2} - k l_{OA} l_{OB} + R_{23}^y l_{OA} \right) \sin \varphi - R_{23}^x l_{OA} \cos \varphi \quad (3-71)$$

where,  $M_{unb}$  is the unbalanced moment.

Assuming that the coupler 3 has the shape of a rod, its mass will be equal to:

$$m_3 = \rho_3 \pi r_3^2 l_3 \quad (3-72)$$

where,  $\rho_3$  is the material mass density and  $r_3$  is the rod radius.

Hence, given that the mass of the coupler 3 is symmetrically distributed, we get:

$$l_{AS_3} = 0.5l_3 \quad (3-73)$$

With regard to the spring 5, its mass can be expressed as [119]:

$$m_5 = \chi \sqrt{k} \quad (3-74)$$

with

$$\chi = \rho \pi L_w \sqrt{\frac{D^3 n}{2G}} \quad (3-75)$$

where,  $G$  is the Shear modulus calculated from the material's elastic modulus  $E$  and Poisson ratio  $\nu$  ( $G = E/2(1+\nu)$ ),  $D$  is the mean diameter of the helix,  $n$  is the number of active coils,  $\rho$  is the material mass density,  $L_w$  is the length of wire.

With added masses of the coupler 3 and the spring 5, the complete balancing of the rotating link 2 is impossible. As a result, an approximate solution must be considered.

In order to do so, the minimization of the root-mean-square value of unbalanced moment must be applied:

$$M_{unb}^{rms} = \sqrt{\sum_{i=1}^N (M_{Gi} + M_{spi} + \Delta M_i)^2} / N \quad (3-76)$$

where,  $N$  is the number of calculated positions of the linkage.

For the minimization of  $M_{unb}^{rms}$ , it is necessary to minimize the sum:

$$\sum_{i=1}^N (M_{Gi} + M_{spi} + \Delta M_i)^2 \rightarrow \min_k \quad (3-77)$$

or

$$\sum_{i=1}^N \left[ (m_2 g l_{OS_2} - k l_{OA} l_{OB} + R_{23i}^y l_{OA}) \sin \varphi_i - R_{23i}^x l_{OA} \cos \varphi_i \right]^2 \rightarrow \min_k \quad (3-78)$$

Eq. (3-78) can be rewritten as:

$$\sum_{i=1}^N \left[ (C_{1,i} + C_{2,i} \sqrt{k} + C_{3,i} k)^2 \right] \rightarrow \min_k \quad (3-79)$$

where,

$$C_{1,i} = m_2 g l_{OS_2} \sin \varphi_i + m_3 g l_{OA} \left[ \frac{l_{AS_3} \cos \psi_i \sin(\psi_i - \varphi_i)}{\sqrt{l_{OA}^2 + l_{OB}^2 - 2l_{OA}l_{OB} \cos \varphi_i}} + \sin \varphi_i \right] \quad (3-80)$$

$$C_{2,i} = 0.5 \chi l_{OA} g \left[ \frac{l_{AC} \cos \psi_i \sin(\psi_i - \varphi_i)}{\sqrt{l_{OA}^2 + l_{OB}^2 - 2l_{OA}l_{OB} \cos \varphi_i}} + \sin \varphi_i \right] \quad (3-81)$$

$$C_{3,i} = -l_{OA} l_{OB} \sin \varphi_i \quad (3-82)$$

The minimum of Eq. (3-79) can be reached when the partial derivative with respect to  $k$  is zero:

$$\partial \sum_{i=1}^N \left[ \left( C_{1,i} + C_{2,i} \sqrt{k} + C_{3,i} k \right)^2 \right] / \partial k = 0 \quad (3-83)$$

From Eq. (3-83), we obtain the following cubic equation:

$$z^3 + az^2 + bz + c = 0 \quad (3-84)$$

where

$$a = 1.5 \sum_{i=1}^N C_{2,i} C_{3,i} / 2 \sum_{i=1}^N C_{3,i}^2 \quad (3-85)$$

$$b = 0.5 \sum_{i=1}^N \left( C_{2,i}^2 + 2C_{1,i} C_{3,i} \right) / \sum_{i=1}^N C_{3,i}^2 \quad (3-86)$$

$$c = 0.5 \sum_{i=1}^N C_{1,i} C_{2,i} / \sum_{i=1}^N C_{3,i}^2 \quad (3-87)$$

$$z = \sqrt{k} \quad (3-88)$$

The solution of equation (3-84) with real coefficient can be expressed in algebraic form by means of Cardano's method.

For determination of roots, first of all, we shall calculate:

$$Q = (a^2 - 3b) / 9 \quad (3-89)$$

$$R = (2a^3 - 9ab + 27c) / 54 \quad (3-90)$$

When  $R^2 < Q^3$ , the cubic equation has three real roots, determined by the following expressions:

$$z_1 = -2\sqrt{Q} \cos(t) - a / 3 \quad (3-91)$$

$$z_2 = -2\sqrt{Q} \cos(t + 2\pi / 3) - a / 3 \quad (3-92)$$

$$z_3 = -2\sqrt{Q} \cos(t - 2\pi / 3) - a / 3 \quad (3-93)$$

$$t = a \cos \left( R / \sqrt{Q^3} \right) / 3 \quad (3-94)$$

When  $R^2 \geq Q^3$ , general cubic equation case has one real root and two real roots for the confluent case.

For determination the complex roots, it is necessary to calculate:

$$A = -\text{sign}(R)\sqrt[3]{|R| + \sqrt{R^2 - Q^3}} \quad (3-95)$$

$$B = \begin{cases} Q/A & (\text{if } A \neq 0) \\ 0 & (\text{if } A = 0) \end{cases} \quad (3-96)$$

The real root is:

$$z_1 = (A - B) - a/3 \quad (3-97)$$

In the case, when  $A=B$ , the complex roots become the real roots:

$$z_2 = -A - a/3 \quad (3-98)$$

After determination of  $z$ , we determine the stiffness of the spring from Eq. (3-88).

Let us now consider an illustrative example with error analysis.

### 3.3.3 Illustrative example with error analysis

Consider the gravity balancing of a rotating link with parameters:  $m_2 = 10\text{kg}$  ;  $l_{OS_2} = 0.3\text{m}$  ;  $\varphi_{initial} = 45^\circ$  and  $\varphi_{final} = 155^\circ$  .

The variation of the moment  $M_G$  produced by the gravity of the rotating link 2 is given in Figure 3-8.

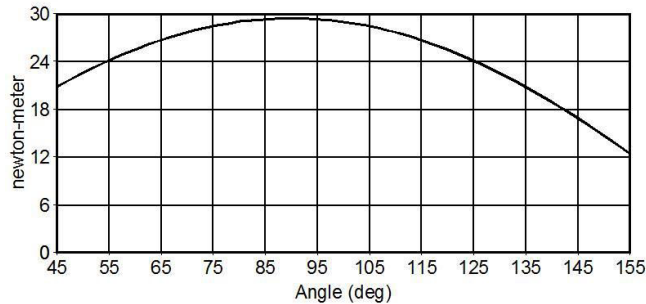


**Figure 3-8.** Moment produced by the gravity of the rotating link 2.

Let us now balance the rotating link 2 via the gravity compensator based on the inverted slider crank mechanism with the parameters:  $l_{OA} = l_{OB} = 0.2475\text{m}$  .

Firstly, it will be balanced without the masses of associated links 3, 4 and 5. Hence, we get  $k = 480\text{N/m}$  with  $F_{preload} = 91\text{N/m}$  . Thus, without the masses of the associated links, the system will be fully balanced.

Given that  $l_{BS_4} = 0$  ,  $l_3 = 1\text{m}$  ,  $l_{AS_3} = 0.5\text{m}$  ,  $\rho_3 = 7800\text{kg/m}^3$  ,  $r_3 = 0.008\text{m}$  , we get  $m_3 = 1.56\text{kg}$  .

With regard to the spring, we will apply the following parameters:  $G = 8.1 \cdot 10^{10} \text{ N/m}^2$ ,  $\rho = 7800 \text{ kg/m}^3$ ,  $D=0.04\text{m}$ ,  $n=100$  and  $L_w = 12.6\text{m}$ . Thus, we get  $m_5 = 1.34\text{kg}$ .

Consequently, with  $k = 480 \text{ N/m}$  and  $F_{preload} = 91 \text{ N/m}$ , taking into account the mass  $m_3$  of the associated coupler 3 and the mass of the spring 5, an unbalanced moment will be appeared (Figure 3-9).

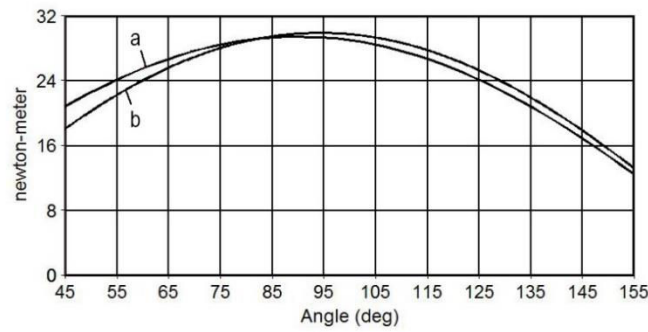


**Figure 3-9.** Moments produced by the gravity of the rotating link 2 (a) and by the gravity of the linkage with the spring (b).

On that account, we can see that there is more than 13% difference between the two studied cases.

Now considering the balancing, taking into account the masses of the coupler 3 and the spring 5 with the same parameters selected for the previous case, from Eq. (3-80) - (3-82), we obtain the following cubic equation:

$$z^3 + 0.91z^2 - 495.12z - 147.34 = 0 \tag{3-99}$$

With  $R^2 < Q^3$ , we have three real roots determined by (3-91) - (3-94) :  $z_1 = -22.56$ ,  $z_2 = 21.95$  and  $z_3 = -0.30$ . Taking  $z = z_2$ , we determine the stiffness of the spring  $k = 484 \text{ N/m}$ .

The simulation results are shown in Figure 3-10.

The obtained results show that in comparison with the previous case where the masses of auxiliary links are neglected, more than 40% reduction of the residual unbalance can be achieved.

Please keep in mind that for comparison, the absolute values of torques must be noted because the signs will change in the opposition movement.



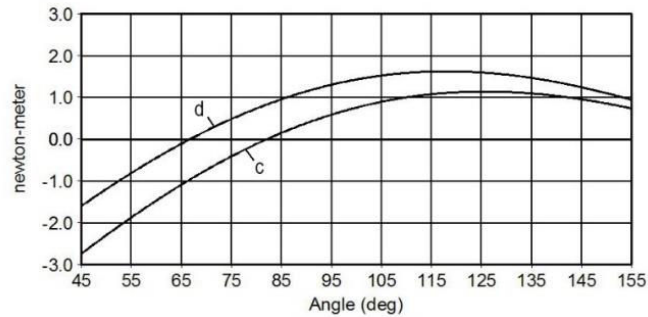


**Figure 3-10.** Residual moments without taking into account the masses of auxiliary links (c) and with them (d).

### 3.4 Summary

In this chapter, the design of gravity balancers via coupling of a rotating link and a two-link dyad is considered. It is known that a full gravity compensation of a rotating link cannot be achieved when a non-zero free length spring, i.e. conventional linear spring, is used. To use non-zero length springs, it is necessary to apply auxiliary mechanical systems. The first section deals with a simple and analytically tractable solution permitting to carry out quasi-perfect balancing of a rotating link by means of a non-zero length spring. In the proposed design the balancing spring is connected with the rotating link by means of an articulated dyad forming a four-bar linkage. Upon rotation of the output link of the four-bar mechanism moves the end of the spring and changes the length of the spring creating a variable balancing moment. An optimization method based on the geometric synthesis of four-bar mechanism and potential energy conservation has been developed, which allows one to control the optimal displacements of the spring providing a suitable balancing moment. The illustrative example has shown that the proposed design ensures gravity compensation for up to 98%.

The second section deals with a similar problem by coupling a rotating link to be balanced and a dyad with prismatic pair, forming with the rotating link a slider-crank mechanism. The particularity of the suggested structural concept is that the balancing spring is installed on the fixed frame, which allows one to reduce the errors due to the spring's weight. Upon rotation of the link moves the end of the spring and changes the length of the spring creating a variable balancing moment. A similar optimization method with some modifications devoted to the geometric synthesis was applied. The efficiency of the suggested mechanism design is illustrated via numerical simulations. By selecting three prescribed positions of the rotating link has been reached a quasi-exact gravity balancing. It has been shown that the maximum value of the unbalanced moment reduced from 63 Nm to 2.92 Nm (95.4%), and in the case of 120 prescribed positions of the rotating link, the maximum value reduced up to 1.87 Nm (97%).

In the last section, it is proposed an improved solution for reducing the error caused by neglecting the masses of the spring and associated links. It is based on the inverted slider crank mechanism considering the masses of the rocker and the spring. Firstly, it is shown that the errors caused by neglecting the masses of the associated links lead to a significant unbalanced moment. Then, it is proposed to use the minimization of the root-mean-square value of the unbalanced moment to reduce these errors. The

numerical simulations are shown that the error caused by neglecting the masses of the associated links is more than 13% of the moment to be balanced. The application of the suggested solution has reduced the residual moment up to 40%. Such an approach can be applied to other types of auxiliary linkages designed for gravity compensators.

# Design and optimization of a new robotic suit for load carriage via coupling cables and a rigid support

---

4.1	Design concept .....	86
4.2	Modelling of the robotic suite .....	89
4.3	Simulations, optimization and control of the robotic suite.....	93
4.4	Experimental validation of obtained results .....	102
4.5	Summary.....	104

---

*From the literature reviews in the first chapter, it can be seen that exoskeletons show impressive results in the rehabilitation, field works, and military. However, their rigid structures have led to a lot of drawbacks like additional inertia and an in compliant interface between them and users. Comparing to the exoskeleton, exosuit is a wearable suit made by soft material and actuated by cable or pneumatic force, which is inherently compliant and much lighter.*

*In this chapter, an exosuit has been designed for assisting people while carrying heavy loads. For this exosuit, polyethylene braid-style cables are used and attached to the user's body through anchors and attachment points, which function as auxiliary muscles to apply force on both upper arm and forearm. The weight of the cables is negligible and adds nearly zero inertia to users. One of the characteristics of the proposed exosuit is that it has two operation modes: passive and active modes.*

*The chapter is organized as follows. In the first part, the design concept of the exosuit is presented. Then, the kinematic and the dynamic models of the exosuit-human coupled system are developed. In the third section, the static, kinematic, and dynamic simulations of the coupled system, as well as the optimization of the distribution of cable attaching positions, are discussed. Finally, the experimental results carried out on a mannequin test bench are presented.*

## 4.1 Design concept

In this study, a soft robotic suit to assist users for carrying heavy loads is proposed. This soft robotic suit is planned to have three features: 1) lightweight: the mass of the suit adds little extra inertia hence user's movement will not be impeded while wearing the robotic suit; 2) compliant: the interface between user and suit is compliant so user will not be hurt due to the installation error or system failure; 3) passive mode: the robotic suit can work in a passive mode where no actuation forces are need.

### 4.1.1 Development of the robotic suit's rigid frame

The rigid frame of the robotic suit consists of five parts: a main frame which fixed on the user's body, two upper arm bracelets which fixed with the user's upper arm, and two forearm bracelets which fixed with the user's forearm. The whole rigid frame is illustrated in Figure 4-1.



**Figure 4-1.** Rigid frame of the robotic suit.

In the main frame of the robotic suit, an adjustable plastic belt is at the bottom of the frame, and when users wear the suit, it fastens on the user's waist as a fixing component of the suit. Two shoulder pads are linked with the belt through two adjustable curved beams which can adapt to users with different height, and between these two beams, six horizontal beams are fixed between them to increase the whole structural strength. In order to create a comfortable interface between the shoulder pad, soft foam materials are stuck at the back of the shoulder pads.

All the four bracelets have a similar structure which consist of two rings a curve pad linked with the rings. The rings are adjustable which can adapt the size of the user's arms. The pads can avoid force concentration since they increase the contact surface between the bracelet and the user's arm. Similar to the should pad, soft foam materials

are also used at the interface between the bracelet and the user's arm for enhancing comfortability.

It should be also noticed that on all the bracelets and shoulder pads, there are some pins combined with some small rings on them, and these are the cable anchors and cable attachment points. We define an anchor is where the cable starts from, the cable is fixed with the small ring. And an attachment point is where the cable only passes through the small ring. For the shoulder pads and upper arm bracelets, the pins are fixed on them, and for the forearm bracelets, the pins are inserted into the groove on the rings which allow the pins have a translational movement along the rings. Thus, the pronation/supination movement of the forearm will not change the position of the anchors and attachment points on the forearm bracelets.

### **4.1.2 Coupling of cables with the rigid frame**

When humans want to move their arms, their muscles contract for generating tension forces; then the forces are transmitted to the skeletons through tendons hence moments will be generated on the articulations for moving their limbs.

In the proposed robotic suit, the cables are used for similar functionality as the human muscles where the cable tension is the muscle's contract force. The cables can transmit forces on the user's arm through arm bracelets and with accurate control of the tensions of the cables, a desirable assistive performance can be obtained by users during load carriage.

The cables for the robotic suit are the polyethylene braid-style cables fabricated by Caperlan which is originally used for fishing. The diameter of the cable is only 0.4mm and the weight is extremely light. The cable can hold up a load up to 34kg, while in the meantime only have a tiny deformation.

Figure 4-2 illustrates a 3D model where a user wears the proposed robotic suit where cables are coupled with the rigid frame and the batteries, control system and motors are mounted on the rigid frame. For each of the user's arm, two cables are started from the anchors on forearm and upper arm, respectively; then pass through the attachment points on the arm and shoulder and then through the inside of the hollow beam which links the shoulder pad and the belt; finally end at spool on the motor which is mounted on the belt.

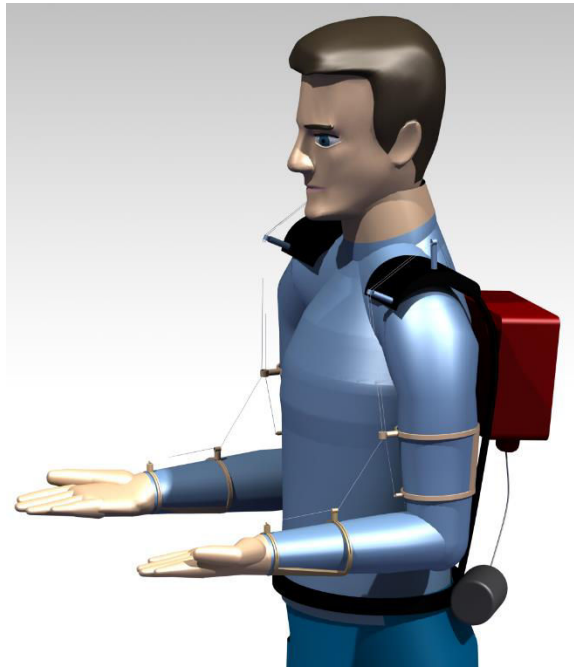


**Figure 4-2.** 3D model of the robotic suit.

### **4.1.3 Robotic suit operation**

When humans want to move a load from one place to another place, normally the transportation can be separated into three phases. The first phase is to let the hands approach the load, then grab it and hold it with a comfortable posture. Then the phase is to hold the load and walk to the final destination where we want to put the load. The last phase is a discharge process in which we adjust our arms to adapt to the place where we want to put the load at, for example, a shelf.

#### *(a) Passive mode*

It can be seen that during the second phase of the load transportation, one stays at a quasi-fixed posture, and the moments generated on the arm's joints are mainly due to gravity and stay relatively constant. Therefore, in this phase, we can let all the cables in tension and stop the movement of the cables, then the movement of user's arm will be constrained and the moment induced by the gravity will be transmitted on the shoulder. Thus, the fatigue of the muscle on the arms due to holding load will be relieved.

Instead of letting the motors generating torque to hold the position of the cable which needs a lot of energy if the distance from the start point and destination is too far, a cable winding and locking mechanism (shown in Figure 4-3) was designed. This mechanism includes a cable spool, a torsional spring and a ratchet mechanism. The cable spool links with the torsional spring and the ratchet. The torsional spring can provide a suitable passive moment for the spool to keep the cable always in tension while users moving their arms. And the ratchet mechanism is used as a locking mechanism to stop the movement of the cable. When wearers pick up the load and hold it in a comfortable position, the locking mechanism can be engaged by pressing the controller on their hands. Then the pawl moves down and enters into the gap between two teeth of the ratchet. Consequently, the spool is stopped from moving and the

passively generated cable tension can be used for compensating the gravity of the load. In contrast, when the user is not carrying loads, the pawl will lift up and the spool can freely rotate.

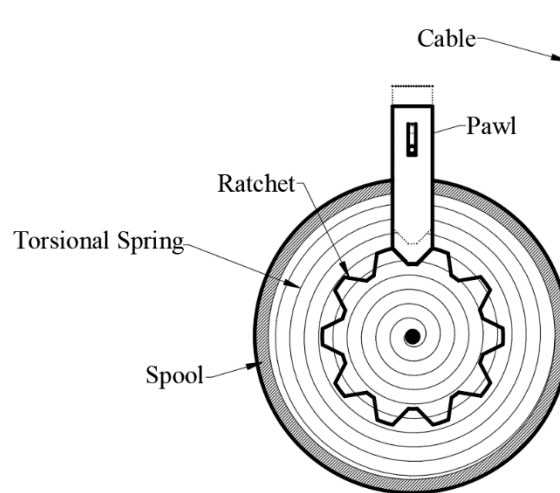


**Figure 4-3.** Cable locking mechanism.

*(b) Active mode*

Unlike the second phase of the load carriage where user's arms stay at a fixed posture and only constant forces are needed for compensating the gravitational effect, in the first and the third phase of the load carriage, wearers need to hold the load and move it to the expected position. Therefore, in these phases, variable forces will be required since the dynamic effect will occur and the forces utilized to compensate the gravitational effect will vary as the user changing their arms postures.

In the proposed design, four DC motors are linked the cable spools providing active forces to the four cables respectively. The torques of the motors are controlled through an on-board closed-loop controller. The pose data obtained by the potentiometers mounted on the joints of the arm can be used by the on-board controller.

For the safety of the users, when robotic suit works in active mode, the maximum force provided to the cable is limited to 150N for all the cables. Additionally, there is also a safety button for cutting off the power source if any emergency happens.

## **4.2 Modelling of the robotic suite**

### **4.2.1 Kinematic and geometric modelling**

A planar diagram of a user wearing the exosuit system is shown in Figure 4-4. In this diagram, two cables start from the anchors on the forearm and upper arm respectively and end at the cable winding and locking mechanisms fixed on the hip. The cable arrangements are as following: cable 1 starts form anchor on point 1, pass through attachment points on point 2, point 4, point 5, point 6, point 7, point 8; cable 2 starts form anchor on point 3, pass through attachment points on point 4, point 5, point 6, point 7, point 8. It is assumed that the deformation of the cable is very tiny and negligible.

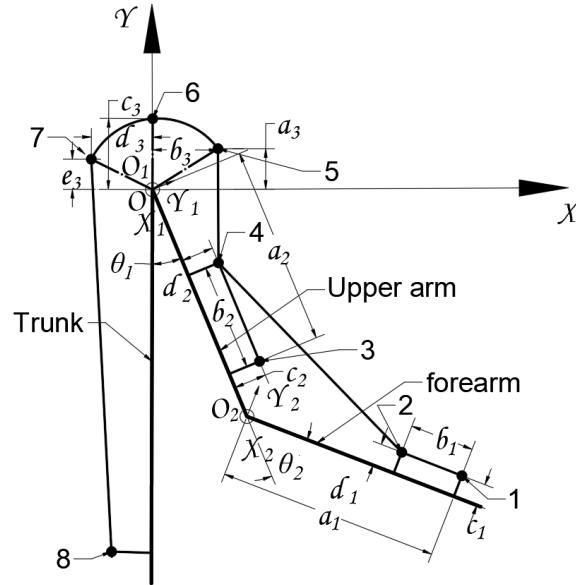


**Figure 4-4.** Planar diagram of the distribution of anchors and attachment points while used wearing the robotic suit.

As shown in Fig. 4-4, two local coordinate systems  $X_1O_1Y_1$  and  $X_2O_2Y_2$  are fixed on the upper arm and forearm respectively. The general coordinate of point  $i$  on the global coordinate system can be calculated by:

$$\mathbf{p}_i = \begin{bmatrix} x_i \\ y_i \\ 1 \end{bmatrix} = \begin{cases} {}^0\mathbf{Trans} \cdot \mathbf{p}_i^1 \\ {}^0\mathbf{Trans} \cdot {}^1\mathbf{Trans} \cdot \mathbf{p}_i^2 \end{cases} \quad (4-1)$$

where,

$${}^0\mathbf{Trans} = \begin{bmatrix} \cos(3\pi/2 + \theta_1) & -\sin(3\pi/2 + \theta_1) & 0 \\ \sin(3\pi/2 + \theta_1) & \cos(3\pi/2 + \theta_1) & 0 \\ 0 & 0 & 1 \end{bmatrix}$$

$${}^1\mathbf{Trans} = \begin{bmatrix} \cos \theta_2 & -\sin \theta_2 & l_{ar} \\ \sin \theta_2 & \cos \theta_2 & 0 \\ 0 & 0 & 1 \end{bmatrix}$$

and  $\mathbf{p}_i^1$  and  $\mathbf{p}_i^2$  stand for the local general coordinates of point  $i$  in local coordinate systems  $X_1O_1Y_1$  and  $X_2O_2Y_2$  respectively,  $l_{tr}$  is the length of the trunk and  $l_{ar}$  is the length of the upper arm.

Thus, the global coordinate of point  $i$  is:

$$\mathbf{c}_i = \begin{bmatrix} x_i \\ y_i \end{bmatrix} \quad (4-2)$$



For both of the two cables, they all have a fixed length through attachment points 5, 6, 7, and 8 since all these points are fixed on the user's trunk. Let's define this fixed length as  $l_0$ . And as shown in Figure 4-4, the local general coordinates of point 1, 2, 3, and 4 are  $\mathbf{p}_1^1 = [a_1, c_1, 1]$ ,  $\mathbf{p}_2^1 = [a_1 - b_1, d_1, 1]$ ,  $\mathbf{p}_3^2 = [a_2, c_2, 1]$ ,  $\mathbf{p}_4^2 = [a_2 - b_2, d_2, 1]$ , and the global coordinate of point 5 is  $\mathbf{cs} = [b_3, a_3]$ . Then the lengths of cable 1 and cable 2 can be calculated by:

$$\begin{cases} l_1 = f_1(\theta_1, \theta_2) \\ l_2 = f_2(\theta_1) \end{cases} \quad (4-3)$$

Then, using the time derivative of Eq. (4-3), the relationship between the cable velocity and the angular velocity of the user's joints can be obtained by:

$$\begin{bmatrix} \dot{l}_1 \\ \dot{l}_2 \end{bmatrix} = \mathbf{J}_v \begin{bmatrix} \dot{\theta}_1 \\ \dot{\theta}_2 \end{bmatrix} \quad (4-4)$$

where  $\dot{l}_1$  and  $\dot{l}_2$  denote the cable velocities.

Due to the limitation of the space, the detailed information of function  $f_1(\theta_1, \theta_2)$ ,  $f_2(\theta_1)$  and matrix  $\mathbf{J}_v$  can be found in Appendix A.

#### 4.2.2 Dynamic modeling

The user carrying the load while wearing the robotic suit can be in analogy with a coupled system including a 2-DOF planar mechanical structure with the load at the end effector and cables attached on the manipulator for exerting forces.

The general dynamic equations of the coupled system can be obtained from the Lagrangian formulation where the generalized coordinate is  $\mathbf{q} = [\theta_1, \theta_2]^T$ . Lagrange's equation can be written in the form of kinetic energy  $K$ , potential energy  $V$  and generalized forces or torques  $\mathbf{Q}$  in the following form:

$$\frac{d}{dt} \left( \frac{\partial K(\mathbf{q}, \dot{\mathbf{q}})}{\partial \dot{\mathbf{q}}} \right) - \frac{\partial K(\mathbf{q}, \dot{\mathbf{q}})}{\partial \mathbf{q}} + \frac{\partial V(\mathbf{q})}{\partial \mathbf{q}} = \mathbf{Q} \quad (4-5)$$

The kinetic energy of the coupled system combines three parts: kinetic energy of the upper arm  $K_1$ , kinetic energy of the forearm  $K_2$ , and kinetic energy of the load  $K_3$ . They can be calculated by:

$$K_1 = \frac{1}{2} I_{ua} \dot{\theta}_1^2 + \frac{1}{2} m_{ua} l_{cua}^2 \dot{\theta}_1^2 \quad (4-6)$$

$$K_2 = \frac{1}{2} I_{fa} (\dot{\theta}_1 + \dot{\theta}_2)^2 + \frac{1}{2} m_{fa} \left[ l_{ua}^2 \dot{\theta}_1^2 + l_{cfa}^2 (\dot{\theta}_1 + \dot{\theta}_2)^2 + 2l_{ua} l_{cfa} \cos \theta_2 (\dot{\theta}_1^2 + \dot{\theta}_1 \dot{\theta}_2) \right] \quad (4-7)$$

$$K_3 = \frac{1}{2} m_{load} \left[ l_{ua}^2 \dot{\theta}_1^2 + l_{load}^2 (\dot{\theta}_1 + \dot{\theta}_2)^2 + 2l_{ua}l_{load} \cos \theta_2 (\dot{\theta}_1^2 + \dot{\theta}_1\dot{\theta}_2) \right] \quad (4-8)$$

where  $I_{ua}$  and  $I_{fa}$  are the moment of inertias of upper arm and forearm respectively;  $m_{ua}$ ,  $m_{fa}$  and  $m_{load}$  are the masses of upper arm, forearm and load respectively;  $l_{ua}$  is the lengths of upper arm;  $l_{cua}$  is the distances between the center of mass of upper arm to the shoulder joint,  $l_{cfa}$  and  $l_{cload}$  are the distances between the centers of mass of forearm and load to the elbow joint.

In this study, the elastic and damping effects of cable are neglected and each cable is assumed to be a force element. Therefore, the potential energy of the system is only due to the gravitational effect and the total potential energy is:

$$V = -m_{ua}gl_{cua}(\cos \theta_1 - 1) + m_{fa}g \left[ l_{ua}(1 - \cos \theta_1) + l_{cfa}(1 - \cos(\theta_1 + \theta_2)) \right] + m_{load}g \left[ l_{ua}(1 - \cos \theta_1) + l_{cload}(1 - \cos(\theta_1 + \theta_2)) \right] \quad (4-9)$$

where  $g$  is the gravity acceleration.

In the coupled system, the generalized torques are induced by the cable tension trough anchors and attachment points on the user's arm. It is obvious that the torques have a relationship with the geometrical distribution of the anchors and attachment points. The moments on the elbow and shoulder joint generated by cable 1 and 2 can be calculated by:

$$\begin{aligned} M_{shoulder}^{cable1} &= [\mathbf{v}_{O_1}^* \times \mathbf{v}_{12} + \mathbf{v}_{O_2}^* \times (\mathbf{v}_{21} + \mathbf{v}_{24}) + \mathbf{v}_{O_4}^* \times (\mathbf{v}_{42} + \mathbf{v}_{45})] \cdot \mathbf{T}_1 \\ M_{elbow}^{cable1} &= [\mathbf{v}_{O_2}^* \times \mathbf{v}_{12} + \mathbf{v}_{O_2}^* \times (\mathbf{v}_{21} + \mathbf{v}_{24})] \cdot \mathbf{T}_1 \\ M_{shoulder}^{cable2} &= [\mathbf{v}_{O_3}^* \times \mathbf{v}_{34} + \mathbf{v}_{O_4}^* \times (\mathbf{v}_{43} + \mathbf{v}_{45})] \cdot \mathbf{T}_2 \\ M_{elbow}^{cable2} &= 0 \end{aligned} \quad (4-10)$$

where,

$$\begin{aligned} \mathbf{v}_{ij}^* &= \mathbf{c}_j - \mathbf{c}_i \\ \mathbf{v}_{ij} &= \frac{\mathbf{c}_j - \mathbf{c}_i}{|\mathbf{c}_j - \mathbf{c}_i|} \end{aligned}$$

and the total moments on shoulder and elbow joints induced by the cable tensions can be calculated by:

$$\begin{bmatrix} M_{shoulder}^{cable} \\ M_{elbow}^{cable} \end{bmatrix} = \begin{bmatrix} M_{shoulder}^{cable1} + M_{shoulder}^{cable2} \\ M_{elbow}^{cable1} + M_{elbow}^{cable2} \end{bmatrix} = \mathbf{J}_M \begin{bmatrix} T_1 \\ T_2 \end{bmatrix} \quad (4-11)$$

where,

$$\mathbf{J}_M = \begin{bmatrix} \mathbf{v}_{o_2,1}^* \times \mathbf{v}_{12} + \mathbf{v}_{o_2,2}^* \times (\mathbf{v}_{21} + \mathbf{v}_{24}) + \mathbf{v}_{o_2,4}^* \times (\mathbf{v}_{42} + \mathbf{v}_{45}) & \mathbf{v}_{o_2,3}^* \times \mathbf{v}_{34} + \mathbf{v}_{o_2,4}^* \times (\mathbf{v}_{43} + \mathbf{v}_{45}) \\ \mathbf{v}_{o_3,1}^* \times \mathbf{v}_{12} + \mathbf{v}_{o_3,2}^* \times (\mathbf{v}_{21} + \mathbf{v}_{24}) & 0 \end{bmatrix}$$

Through substituting Eq. (4-6) - (4-9) into Eq. (4-5), the general dynamic equation of the coupled system in terms of generalized coordinates can be obtained as the following form:

$$\mathbf{M}(\mathbf{q})\ddot{\mathbf{q}} + \mathbf{C}(\mathbf{q}, \dot{\mathbf{q}})\dot{\mathbf{q}} + \mathbf{G}(\mathbf{q}) = \mathbf{J}_M [T_1 \quad T_2]^T \quad (4-12)$$

where  $\mathbf{M}(\mathbf{q})$  is the inertia matrix of the system,  $\mathbf{C}(\mathbf{q}, \dot{\mathbf{q}})$  is the matrix of Coriolis and centripetal terms,  $\mathbf{G}(\mathbf{q})$  is the vector of gravity terms. The detailed form of Eq. (4-12) can be found in Appendix A.

### 4.3 Simulations, optimization, and control of the robotic suite

#### 4.3.1 Static simulations and optimization

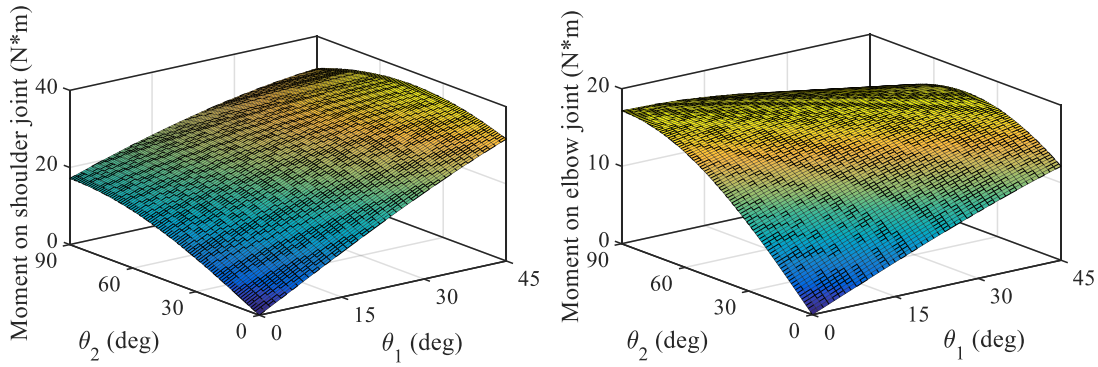
When people carry an object at a relatively fixed position, their arms undertake the load generally due to the gravitational effect of the arm. The gravity of object and arm generate moments on the shoulder and elbow joints which must be compensated by our muscle force. The moments on the shoulder and elbow joints induced by the gravitational force is  $\mathbf{G}(\mathbf{q})$  term in Eq. (4-12) and it can be calculated by:

$$\begin{aligned} M_{shoulder}^{gravity} &= m_{ua} g l_{cua} \sin \theta_1 + m_{fa} g [l_{ua} \sin \theta_1 + l_{cfa} \sin (\theta_1 + \theta_2)] + m_{load} g [l_{ua} \sin \theta_1 + l_{cload} \sin (\theta_1 + \theta_2)] \\ M_{elbow}^{gravity} &= (m_{fa} l_{cfa} + m_{load} l_{cload}) g \sin (\theta_1 + \theta_2) \end{aligned} \quad (4-13)$$

The average body segment parameters of an adult male with 172.68cm height and 63.97kg weight are given in Table 4-1[120]. Using these parameters, the gravity moments on waist, shoulder and elbow joint when carrying a 10kg load with different postures ( $\theta_1 \in [0^\circ, 45^\circ]$ ,  $\theta_2 \in [0^\circ, 90^\circ]$ ) are shown in Figure 4-5. It is shown that when carrying the load with different postures, the gravitational moments on the joints also vary and these moments must be compensated by the muscle force.

**Table 4-1.** Body segment parameters of an adult male.

	Mass (kg)	Length (m)	Location of COM (m)
Upper Arm	2.07	0.364	0.182
Forearm	1.7	0.299	0.149



(a) Gravitational moment on shoulder joint (b) Gravitational moment on elbow joint

**Figure 4-5.** Gravitational moment on the shoulder(a) and elbow(b) joint when carrying a 10kg load with different postures.

When a user wears the exosuit which is in passive mode, the cable locking mechanism is engaged and the gravitational effect of the load and arm can be compensated by cables and distributed on the shoulder. According to Eq. (4-11), the cable tensions for compensating the gravitational effect can be solved by:

$$\begin{bmatrix} T_1^{gravity} \\ T_2^{gravity} \end{bmatrix} = \mathbf{J}_M^{-1} \begin{bmatrix} M_{shoulder}^{gravity} \\ M_{elbow}^{gravity} \end{bmatrix} \quad (4-14)$$

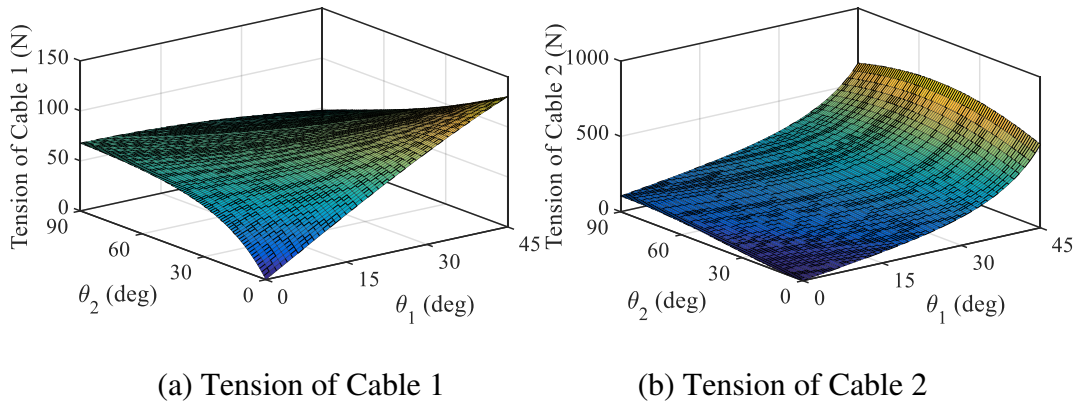
and the force applied on the shoulder by cables is:

$$\mathbf{F}_{shoulder}^{gravity} = \mathbf{v}_{54} (T_1^{gravity} + T_2^{gravity}) \quad (4-15)$$

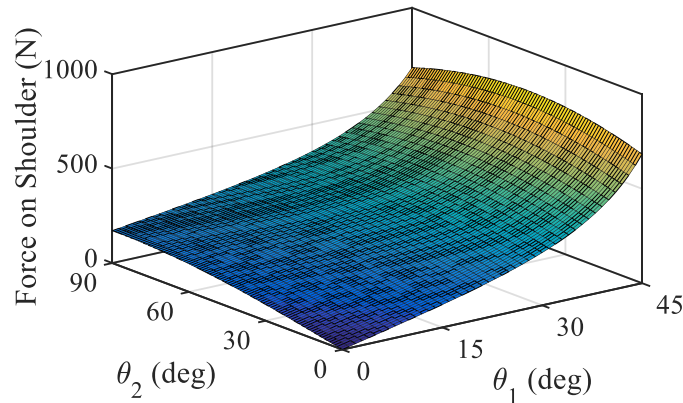
It can be seen that the elements in the matrix  $\mathbf{J}_M$  are determined by the geometrical distribution of anchors and attachment points. To investigate the cable tensions during the usage of the exosuit in passive mode, at first, we chose the initial positions of anchor and attachment points as following:  $a_1=0.3m$ ,  $b_1=0.1m$ ,  $c_1=0.08m$ ,  $d_1=0.08m$ ,  $a_2=0.26m$ ,  $b_2=0.1m$ ,  $c_2=0.1m$ ,  $d_2=0.1m$ ,  $a_3=0.65m$ ,  $b_3=0.1m$ ,  $c_3=0.1m$ ,  $d_3=0.1m$  and  $e_3=0.1m$ .

Figure 4-6 shows the cable tensions when the user carries a 10kg load with different arm postures, where the maximum tensions are 130N and 711N for cable 1 and 2 respectively. It should be noticed that, for the maximum tension in cable 2, the limit of the max tolerable tension has already been passed. Besides, for some postures, the tension of cable 2 is negative which is not permissible.

Another thing has to be concerned with is the force exerted on the shoulder by cables, since a large portion of force has been redistributed on the shoulder. Figure 4-7 shows the force on the shoulder while the user carrying a 10kg load with different postures. It can be seen the maximum force on the shoulder reaches up to 1355N, and this amount of force will be harmful for users.



**Figure 4-6.** Cable tensions when carrying a 10kg load with different postures.



**Figure 4-7.** Force on the user's shoulder when carrying a 10kg load with different postures.

It is obvious that the initial locations of the anchors and attachment points are not suitable for our robotic suit since the large cable tension and the large pressure on the shoulder. Therefore, in order to have a suitable arrangement of anchors and attachment points, their locations must be optimized.

Genetic algorithm (GA) is a kind of mathematical algorithm which is inspired by the process of natural selection. Nowadays, GA is widely and commonly used for solving multi-parameter optimization problems.

In GA, a population of candidate solutions (individuals) to an optimization problem is evolved toward better solutions. Like the creature, each individual has a set of properties (chromosomes) which can be mutated and altered. Normally, the GA starts from a population of individuals which are randomly generated, and the population in each iteration is called a generation. In each generation, there is an objective function to evaluate the fitness of each individual in the population. The more fit individuals are stochastically selected from the current population, and each individual's genome is modified (recombined and mutated) to form a new generation. The new generation of candidate solutions is then used in the next iteration of the algorithm. Commonly, when the maximum number of generation is or a satisfactory fitness level is reached, the GA will be terminated [121].

In the optimization, we take GA as our optimization algorithm and the parameters which are going to be optimized are  $a_1, b_1, c_1, d_1, a_2, b_2, c_2, d_2, a_3, b_3, c_3, d_3,$  and  $e_3$  (as shown in Figure 4-4). For the possible postures of the user, we choose the arm configurations as  $\theta_1 \in [0^\circ, 15^\circ, \dots, 45^\circ]$  and  $\theta_2 \in [0^\circ, 10^\circ, \dots, 90^\circ]$  which gives us 40 possible postures. In this optimization, we are going to minimize the total cable tensions and force exerted on the shoulder when the user carrying a 10kg load with these 40 possible postures.

Another thing has to be concerned is the constraints. In our problem, there is two kinds of constraints which are:

- (1) For all the configurations, cables must be always in tension i.e. cable tensions are always positive;
- (2) The space constraints of the positions of anchors and attachment points.

Hence the problem in this optimization can be concluded as:

$$\min_{a_1, b_1, \dots, e_3} \left( \sum_{\theta_1} \sum_{\theta_2} (T_1^{gravity} + T_2^{gravity} + F_{shoulder}^{gravity}) + P \right) \quad (4-16)$$

subject to:  $0.2 \leq a_1 \leq 0.3$ ;  $0.01 \leq b_1 \leq 0.1$ ;  $0.08 \leq c_1 \leq 0.13$ ;

$0.08 \leq d_1 \leq 0.13$ ;  $0.16 \leq a_2 \leq 0.26$ ;  $0.01 \leq b_2 \leq 0.1$ ;

$0.1 \leq c_2 \leq 0.15$ ;  $0.1 \leq d_2 \leq 0.15$ ;  $0.55 \leq a_3 \leq 0.7$ ;

$-0.1 \leq b_3 \leq 0.1$ ;  $0.05 \leq c_3 \leq 0.15$ ;  $-0.1 \leq d_3 \leq 0.1$ ;

$0.05 \leq e_3 \leq 0.15$ .

where P is a very large value to penalize the goal function when any of the cable tension is negative for all configurations. The optimization procedure can be seen in Figure 4-8.

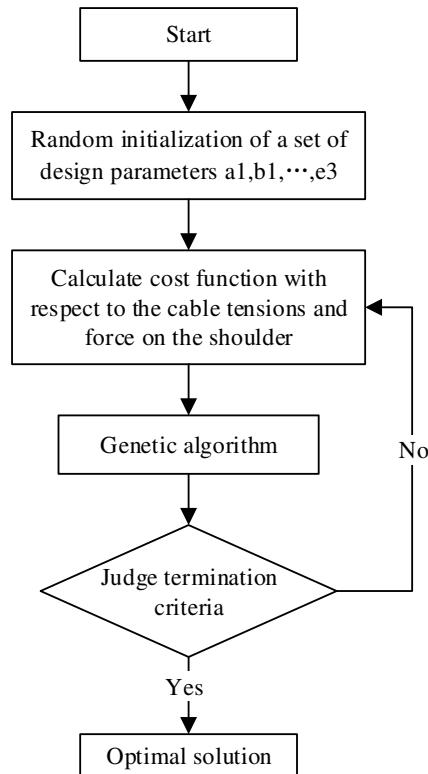


**Figure 4-8.** Optimization procedure.

The obtained optimal parameters are the followings:  $a_1=0.23m$ ,  $b_1=0.1m$ ,  $c_1=0.11m$ ,  $d_1=0.08m$ ,  $a_2=0.26m$ ,  $b_2=0.01m$ ,  $c_2=0.14m$ ,  $d_2=0.15m$ ,  $a_3=0.7m$ ,  $b_3=-0.1m$ ,  $c_3=0.15m$ ,  $d_3=0m$  and  $e_3=0.05m$ . With these parameters, the cable tensions with respect to different postures are shown in Figure 4-9. It can be seen that after optimization the cable tensions have been drastically reduced, with maximum values of 65N and 114N for cable 1 and cable 2 respectively. Meanwhile, as shown in Figure 4-10, the force exerted on the shoulder has also been generally diminished, with the maximum value of 304N. Therefore, after optimization, the exosuit is more suitable and comfortable to wear.

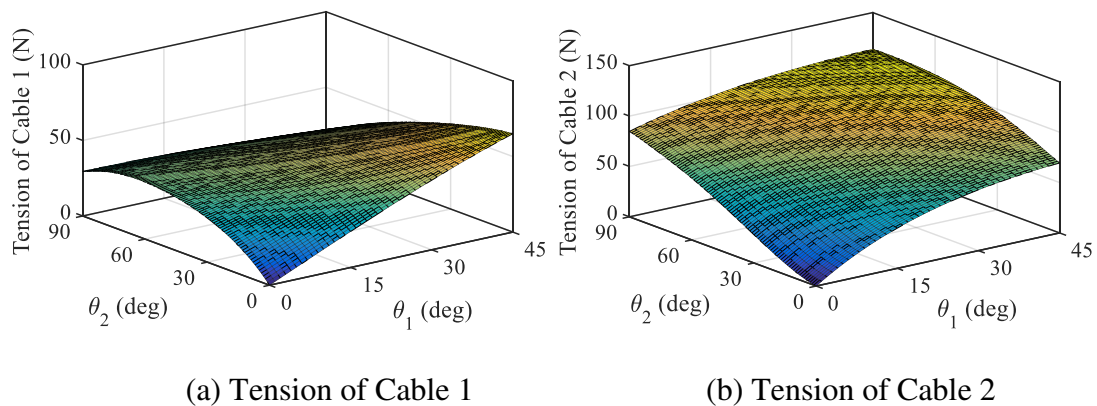


**Figure 4-9.** Cable tensions when carrying a 10kg load with different postures after optimization.

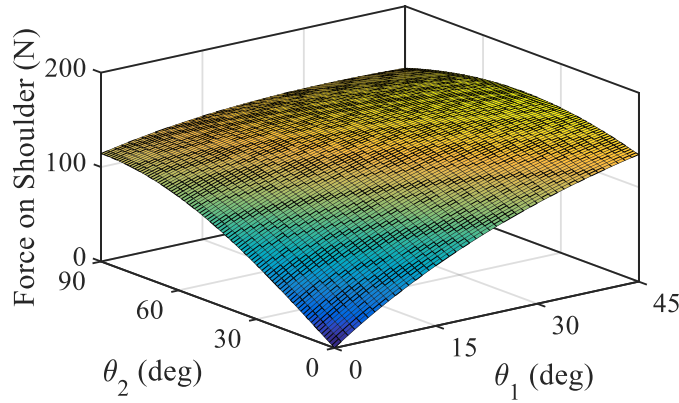


**Figure 4-10.** Force on the user’s shoulder when carrying a 10kg load with different postures after optimization.

### 4.3.2 Workspace analysis

Unlike the traditional exoskeleton in which the actuation forces are transmitted through rigid links to the user, in the proposed robotic suit, cables are used as the transmission media. Therefore, limited by the characteristic of the cable, only tension forces can be transmitted.

While the determination of the workspace of the exosuit, the physical limitation of the cable must be considered. Hence, we can define the workspace of the exosuit as a set of joint angles  $[\theta_1^i, \theta_2^i]$  which fulfill the following condition:

$$T_k^{gravity}(\theta_1^i, \theta_2^i) \geq 0 \quad (k = 1 \text{ and } 2) \quad (4-17)$$

For investigating the workspace of the proposed robotic suit, the arm configurations which satisfy the condition described in Eq. (4-17) were found taking the optimal positions of the anchors and attachment point which was obtained in the previous part.

Figure 4-11 shows all the possible arm configuration of the exosuit. It can be seen that the workspace comprises most part of the real configurations of the human arm except for some part when the upper arm is in extension (the humerus is rotated out of the plane of the torso so that it points backward) or upper arm has large flexion angle.



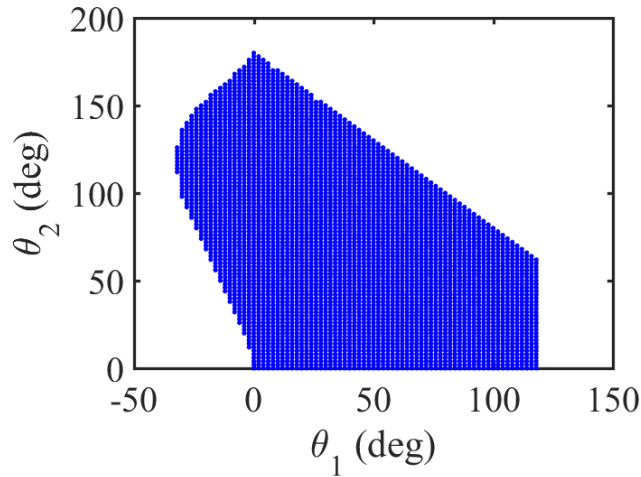


**Figure 4-11.** Workspace of the propose exosuit.

### 4.3.3 Dynamic simulations and controller design

When users want to pick up the load on the ground or put the load on a high shelf, their posture must be changed in order to adjust the vertical level of the load. Therefore, unlike the robotic suit works in passive mode, a controller must be needed for providing the different actuating force with respect to different postures. In addition, the dynamic effect of the user's arm and load must be taken into consideration.

In the proposed design, a closed loop control based on a PD controller and a feedforward term for gravity compensation is utilized for controlling the active force. Potentiometers are mounted on the user's arms for the measurement of elbow and shoulder joint angles. It should be noticed that, for the controlled output forces, only positive values can be provided since only tension forces can exist in the cables. The final controlled active force can be expressed as the following:

$$\mathbf{T}_{\text{active}} = \max \left\{ \mathbf{J}_M^{-1}(\boldsymbol{\theta}) \left[ \mathbf{K}_p (\boldsymbol{\theta}_d - \boldsymbol{\theta}) + \mathbf{K}_d (\dot{\boldsymbol{\theta}}_d - \dot{\boldsymbol{\theta}}) + \mathbf{G}(\boldsymbol{\theta}_d) \right], [0 \ 0]^T \right\} \quad (4-18)$$

where  $\boldsymbol{\theta}_d$  and  $\dot{\boldsymbol{\theta}}_d$  are the desired joint angles and joint velocities;  $\mathbf{K}_p$  and  $\mathbf{K}_d$  are the diagonal matrices consist of proportional and derivative gains of the PD controller respectively.

A block diagram of the proposed controller is shown in Figure 4-12. It can be seen that a prescribed desired state of the system is given as the input. A feedforward loop which is comprised of the gravity compensation to eliminate the effect of gravitational force. A feedback loop consists of a PD controller which uses the measured real state of the system to generate appropriate dynamic forces which actuate the system to the desired state.

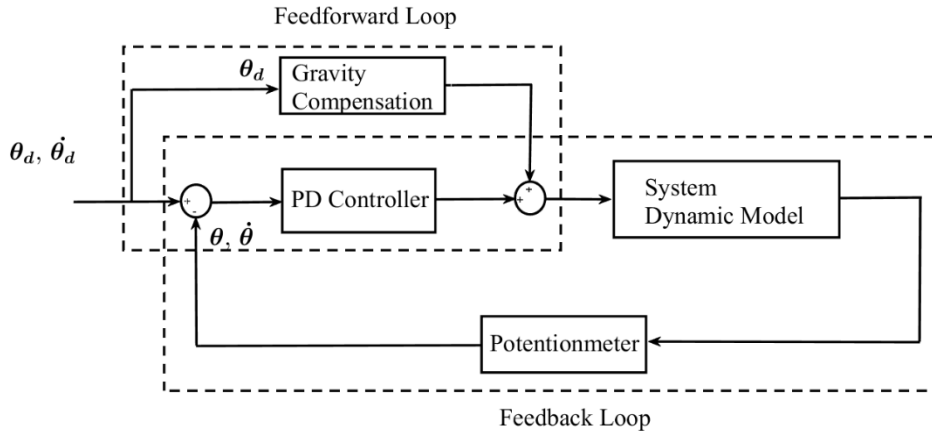


**Figure 4-12.** Block diagram of the PD controller with gravity compensation.

Additionally, in order to let simulation model be more realistic to the working environment, an extra term has been added on the system dynamic model representing nonlinear external disturbances (e.g., vibration during walking, etc.). These disturbances are modeled as random white noises in the proposed model.

For generating a smooth trajectory between the initial position and final desired position, a trajectory generation method based on sinusoidal function has been utilized. The trajectory of a joint can be represented by the following equations:

$$q(t) = \begin{cases} q_i + \frac{q_f - q_i}{2} \left[ \sin\left(\frac{t}{\tau}\pi - \frac{\pi}{2}\right) + 1 \right] & (t \leq \tau) \\ q_f & (t > \tau) \end{cases} \quad (4-19)$$

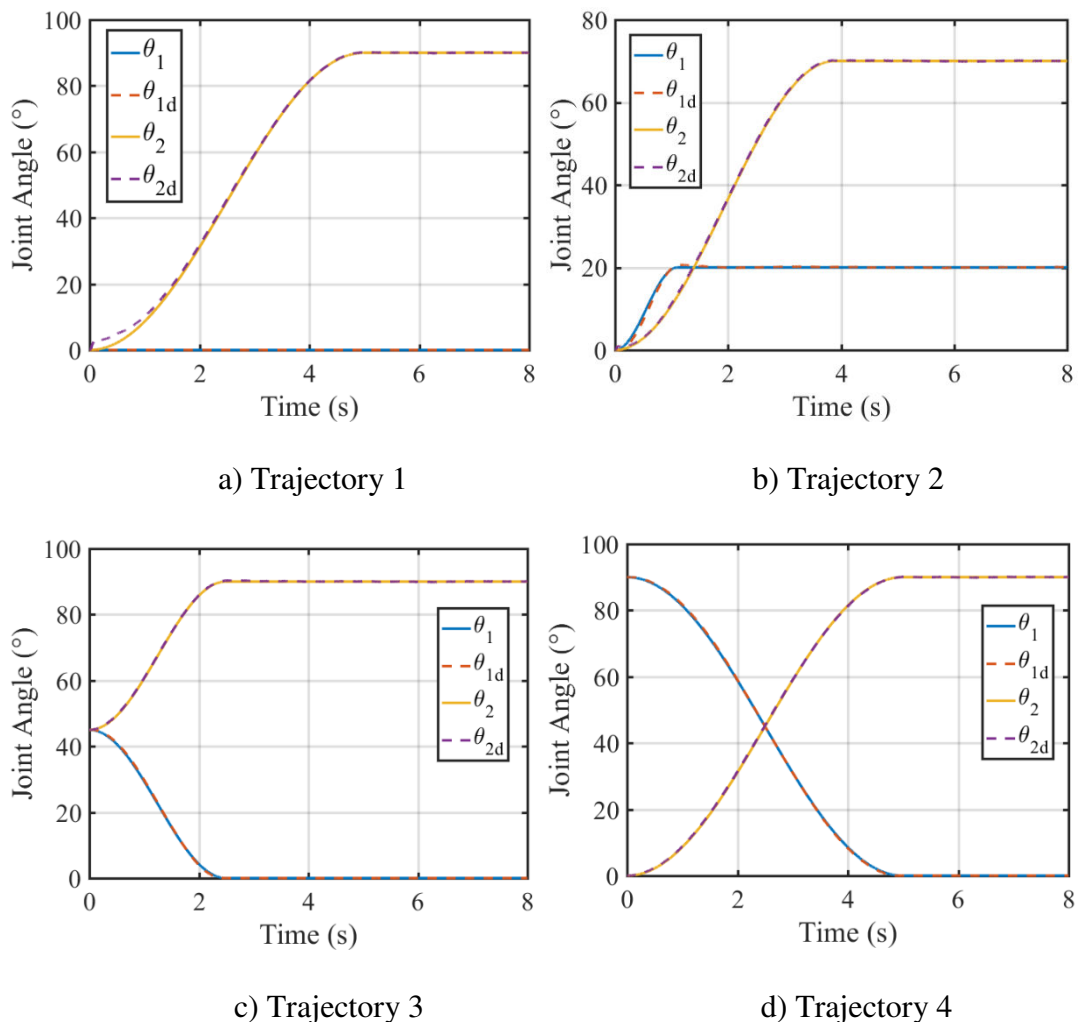
where  $q_i$  is the initial position,  $q_f$  is the final desired position and  $\tau$  is the duration of the sinusoidal trajectory.

Based on the dynamic model described in section 4.3, a Simulink model of the proposed system has been built, and the detailed information of this model can be found in Appendix B. Dynamic simulations of the system have been carried out via the Simulink model for validating the effectiveness of the controller and the exosuit's operation in active mode. And for demonstrating the system having the capability of coping with various trajectories, four different trajectories have been chosen based on previously proposed trajectory generation method. The parameters of these trajectories are shown in Table 4-2.

**Table 4-2.** Parameters of the trajectories.

	$q_{i1}$ (deg)	$q_{f1}$ (deg)	$\tau_1$ (s)	$q_{i2}$ (deg)	$q_{f2}$ (deg)	$\tau_2$ (s)
<b>1</b>	0	0	0	0	90	5
<b>2</b>	0	20	1.11	0	70	3.89
<b>3</b>	45	0	2.5	45	90	2.5
<b>4</b>	90	0	5	0	90	5

In Figure 4-13, the solid lines show the variations of joint angles during simulation and the dash lines shows the desired input trajectories to follow. It can be noticed that, for all four trajectories, the robotic suit shows high tracking performance with the help of the proposed PD controller. The robot suit follows the prescribed trajectories quite accurately even under the external random disturbances.

**Figure 4-13.** Comparison of the actual and desired trajectories.

The cable tensions (which is also the active force in robotic suit system) during the different trajectory trackings are shown in Figure 4-14. It can be seen that the cable

tension fluctuates during the simulations, which is a response to the external disturbance controlled by PD controller. In most of the situations, the cable tension is under 120N which is a quite safe value since the cable can hold the tension up to 340N.

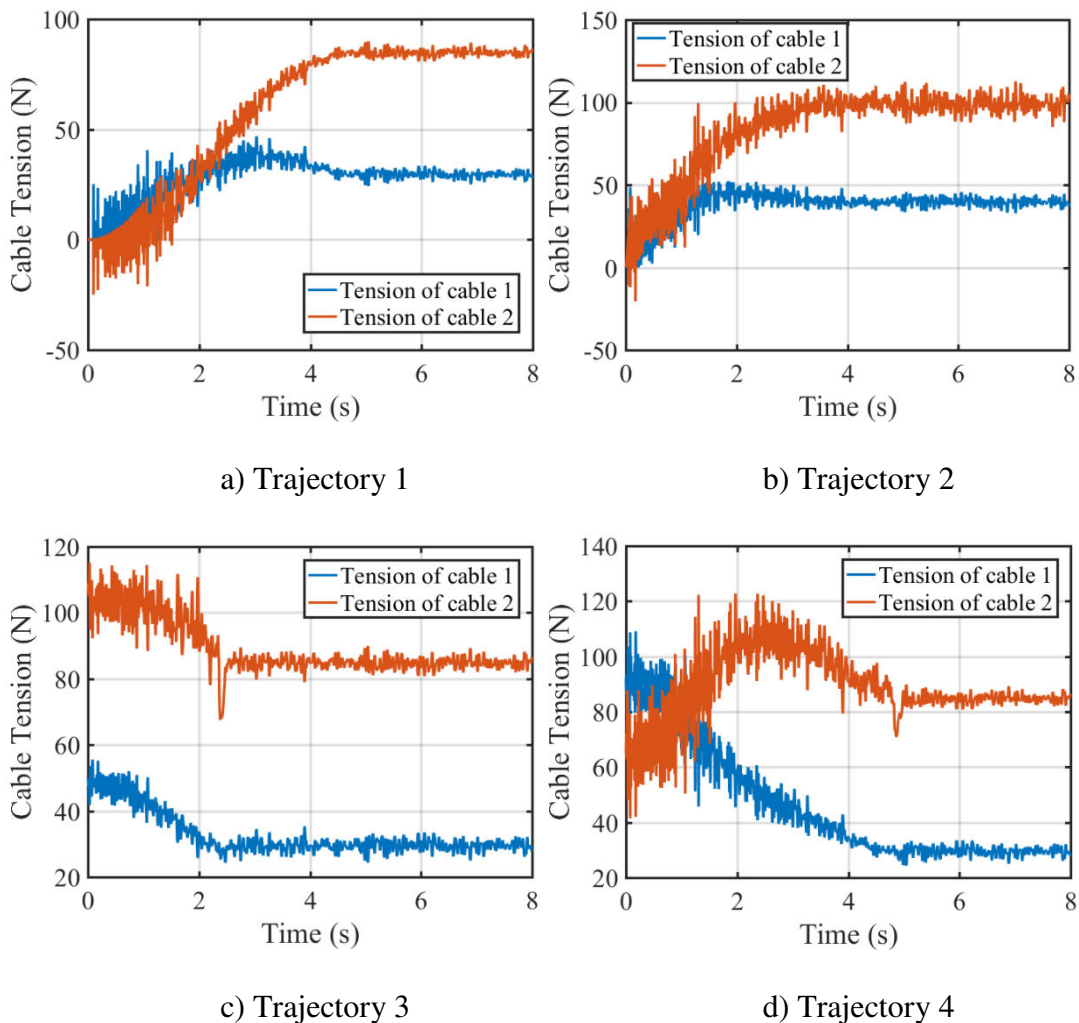


**Figure 4-14.** Cable tensions for the tested trajectories.

#### 4.4 Experimental validation of obtained results

In order to evaluate the performance of proposed passive exosuit, a testbench was fabricated as shown in Figure 4-15. The test bench was converted from a mannequin where spherical joints were added on the elbow joints and shoulder joints.



**Figure 4-15.** Mannequin test bench (a) and the added joints (b, c).

To test the performance of the exosuit when a user is in different postures, several postures have been chosen in this experiment. For the shoulder extension angle, we chose  $0^\circ$  and  $30^\circ$ , and for the forearm flexion angle  $0^\circ$ ,  $30^\circ$ ,  $60^\circ$ , and  $90^\circ$  were chosen. And for each posture, we put no load, 5kg load, and 10kg load respectively. Then the cable tensions were measured.

When the experiments were conducted with different postures and different load, with the help of the exosuit, the mannequin test bench can hold the load steadily in the designated postures. The change of the cable tensions with respect to the change of forearm flexion angle when shoulder extension angle is  $0^\circ$  and  $30^\circ$  are shown in Figure 4-16 and Figure 4-17 respectively.

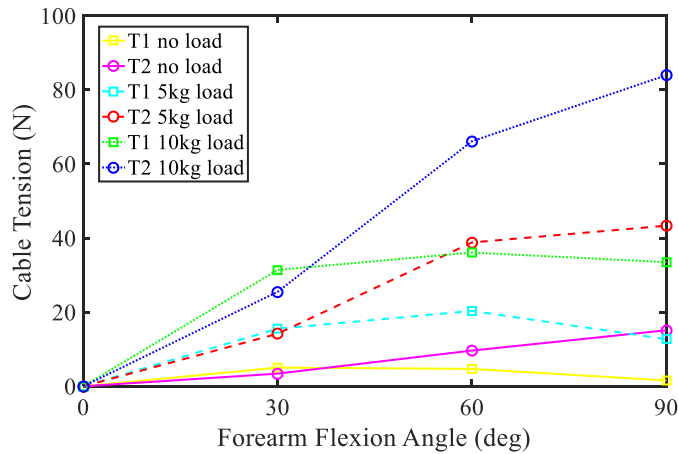


**Figure 4-16.** Cable tensions with respect to the change of forearm flexion angle (shoulder extension angle is 0°).

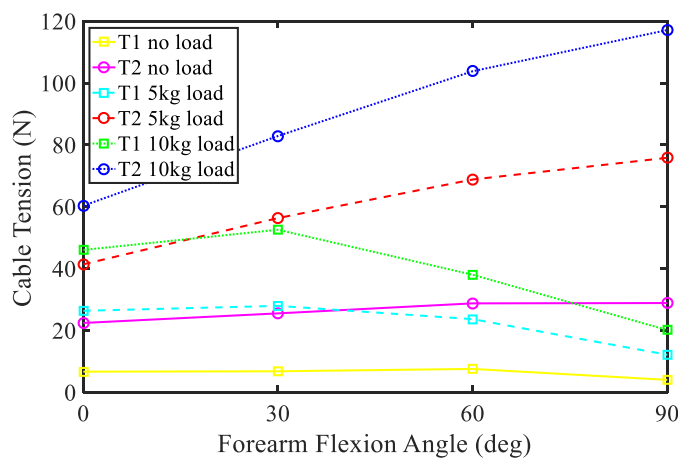


**Figure 4-17.** Cable tensions with respect to the change of forearm flexion angle (shoulder extension angle is 30°).

#### 4.5 Summary

In this chapter, a robotic suit has been proposed which intends to assist its user in the carriage of heavy load. The proposed robotic suit presents a symbiosis of two systems: a rigid support frame and a cable system. The cable system is coupled with the rigid support frame providing assistive force to its users during load carriage and it is made up of high-intensity polyethylene cables, which are very light and add almost zero inertia to users. A cable locking mechanism has been designed in order to keep cables in tension and to stop the movement of the cables.

The robotic suit has two operation modes: passive and active modes. When wearers hold the load at a fixed posture, the cable locking mechanism is engaged to stop the movement of the cable and the robotic suit works in the passive mode where no energy is needed. When users change their postures while holding the load, the robotic suit works in the active mode providing variable assistive forces with respect to the movement.

The kinematic and dynamic models of the robotic suit system have been built. Static simulation has been carried out via the built model and an optimization of the position of the anchors and attachment points of the robotic suit has been made based on genetic algorithm for minimizing the cable tension and force exerted on the shoulder. The workspace of the robotic suit has been analyzed, and dynamic simulations of the robotic suit have been carried out with the design of a PD controller. All the simulations showed that the robot suit had good performances during working in both passive and active modes.

In order to evaluate the performance of the robotic suit in a more realistic environment and validate the simulation results, a mannequin test bench has been fabricated and tested. The test results showed that with the help of the robotic suit, the mannequin can hold different weights of loads steadily in different postures.





# Design and optimization of a mechanical system coupling hand operated balanced manipulator with cobot

---

5.1	Design concept of coupling HOBM with cobot .....	108
5.2	Dynamic analysis of the coupled system and methods for reducing oscillations in the final phase of the trajectories.....	111
5.3	Dynamic analysis for determining admissible trajectories of the cobot taking into account the inertia effect of the HOMB .....	119
5.4	Summary.....	134

---

*In this chapter, a coupled system including a hand-operated balanced manipulator (HOBM) and an industrial collaborative robot (cobot) is presented. The aim of such cooperation is to manipulate heavy payloads with less powerful robots. In another term, in the coupled system for handling of heavy payloads by a HOBM, an operator is replaced by cobot. The advantages of the coupled HOBM and cobot are disclosed and the optimal design of the cooperative workspace is discussed. The Behavior of the coupled system in a static mode when the velocities of the HOBM are limited does not present any special problems. In this mode, the inertial forces are significantly lower than the gravitational one. The payload is completely balanced by the HOBM and the cobot assumes the prescribed displacements without any perturbation.*

*However, in the dynamic mode, the HOBM with massive links creates additional loads on the cobot due to the inertia effect, which can be significant. The present study considers a method for determination of static and dynamic effects of the HOBM on the cobot. Dynamic analysis of the coupled system is performed and methods for reducing the oscillation of the HOBM at the final phase of the prescribed trajectories are proposed. The additional load exerted on the cobot by the inertia effects of the HOBM is studied and the admissible trajectory of the coupled system is determined. The obtained results have been validated by industrial tests.*

## **5.1 Design concept of coupling HOBM with cobot**

### **5.1.1 Statement of the problem**

Workers in industries such as manufacturing and assembly, frequently manipulate heavy objects. However, manual processing is often repetitive and becomes tedious, it reduces efficiency and leads to back pains, injuries, and musculoskeletal disorders. It is obvious that traditional robot installations can offer several benefits compared to manual operation: improved repeatability, increased precision, and speed. However, industrial robots still have many weaknesses compared to humans. For example, currently, industrial robots have a limited ability to perceive their surroundings, which requires costly safety arrangements in order to avoid serious injury. These safety arrangements are particularly important and expensive when working with installations of large and powerful industrial robots. It is obvious that serial industrial robots have a poor payload-to-weight ratio. For a six-degrees-of-freedom general-type serial robot, it is less than 0.15 [122]. For example, a robotic arm handling an object of 50 *kg* must have a weight of at least 350 *kg*. The purchase, installation, and operation of such a robot are quite expensive. In addition, the heaviness of the robot and of the payload complicates the dynamics of the system, making it difficult to move accurately and quickly. This becomes especially noticeable during assembly processes when heavy parts must be installed on a surface with guiding pins. In such a case, the robotic arm has to move smoothly and any sudden movement may damage the mechanical surface of the part. Such a task is not easy to achieve. Thus, autonomous manipulation does not always provide expected reliability and flexibility.

### **5.1.2 Proposed coupled system**

When robots operate in a relatively slow movement, most of their actuation forces are used for compensating the gravitational effect of the payload. Hence, if the gravity of the payload can be compensated by another system, the requirement of the maximum torque of the robot will be much lower since only the dynamic part of the required torque need to be provided. In this chapter, we intend to propose a coupled system including a hand-operated balanced manipulator for compensating the gravity of the payload and a lightweight collaborative robot for guiding the movement of the payload. The combination of the motion programming of the cobot and the simplicity of the HOBM may make the system far better than the application of an individual robot arm.

HOBM is a handling system with a simple mechanical actuator in which the manipulated object in any position of the workspace is balanced. Such a state of constant balance allows displacements of heavy objects to be achieved manually. The advantages of these manipulators relatively to industrial robots are the simplicity of their construction and their low cost. They have a great weight-carrying capacity and a very large workspace. The implantation of HOBM in the existing production line is very simple without the need for important additional surfaces, special auxiliary devices or essential reorganization of the production layout. The use of such manipulators includes a mode of operation when mechanical devices and humans cooperate to hold and move objects. Although the HOBM already compensate the gravity of the payload and the physical burdens of the operator are relived, however, during some repetitive

operations like pick-and-place, the accumulative physical activities are still considerable and may lead to musculoskeletal disorders.

In the proposed system, the operator is replaced by a lightweight cobot UR10. The utilization of UR10 brings a lot of advantages. For example, it allows human intervention to control and guide the payload, and such cooperation becomes much more efficient since it does not exclude the possibility of having a human in the workspace of a robot. Thus, it can reduce costs for space and safety measures as shared space is possible. Additionally, compared to the industrial robots, UR10 is much cheaper and much lighter, hence the robot can be easily moved for adapting different working environments and different tasks.

The proposed coupled system combining a HOBM and a cobot is shown in Figure 5-1. The HOBM is connected with the end effector of the cobot through a cable-pulley system and a pneumatic cylinder is mounted on the HOBM which provides the balancing force for compensating the gravity of the payload.

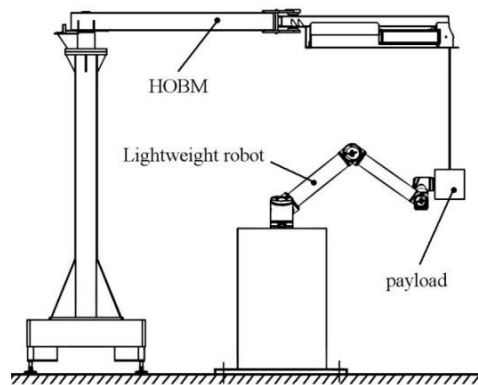


**Figure 5-1.** Lightweight cobot and HOBM cooperation for handling of heavy parts.

### 5.1.3 Optimal design of the collaborative workspace of the coupled system

When designing coupled systems, it is necessary to keep in mind that they consist of two units with different characteristics. However, some of their parameters can be modified during the cooperation of these units. One of the first is to consider structural compliance, i.e. any movement of the payload carried out by means of a cobot must be accompanied by a HOBM. If there is a discrepancy between the movements of these two units, the coupled system will be blocked.

The proximal arm (arm 1) of the HOBM used in the coupled system is able to rotate over 360 degrees for providing the largest workspace (Figure 5-2a). It can be seen that the vertical axis of the HOBM is installed on a heavy platform which can ensure the static balance of the HOBM. However, in the coupled system with joint workspace, the HOBM uses only a small portion of its reachable space since the workspace of the UR10 is relatively small comparing to the HOBM. Hence, during the real application, only half of the workspace of the HOBM is utilized. Thus, the design of the HOBM can be modified to be adapted to the new conditions of coupling.

The rotational range of the proximal arm of the HOBM is constrained to 180°. Additionally, the vertical axis of the HOBM can be brought closer to the cobot, and the

static balance can be saved with a counterweight on the opposite side of the coupled system workspace (Figure 5-2b). In our case, the vertical axis is moved 0.15m closer to the cobot and after calculation for maintaining the static balance, a 200-kg counterweight need to be placed on the other side of the platform.

Such an arrangement is more optimal in terms of the cooperative workspace as the platform of the HOBM has fewer impediment to the workers. Practical implementation of such modifications may look as shown in Figure 5-3.

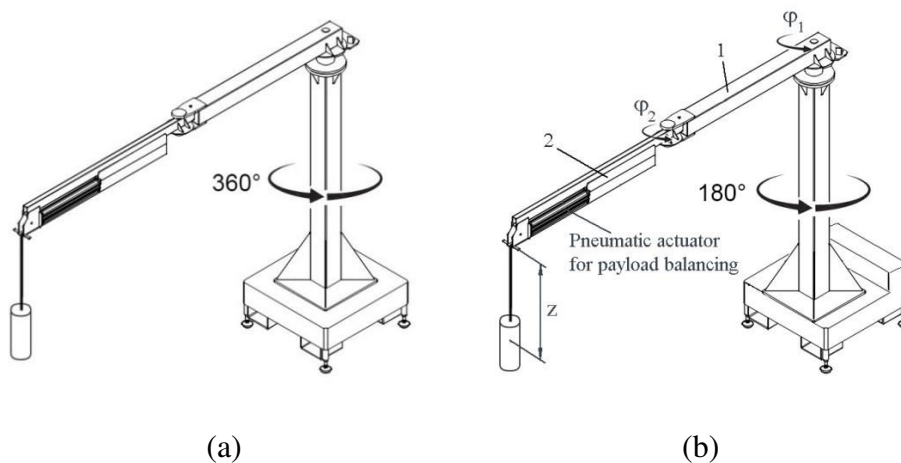


**Figure 5-2.** Workspace of the HOBM before (a) and after (b) modification for cooperating with cobot.

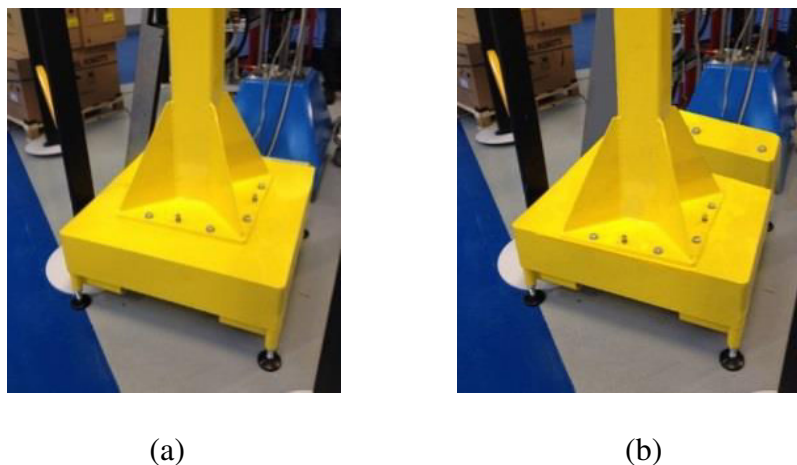


**Figure 5-3.** Frame of the usual HOBM (a) and its modified version (b) for balancer - lightweight robot cooperation.

It should also be noted that the cooperative workspace of the coupled system must be collision and singularity free. Let's illustrate with an example. Figure 5-4 presented a coupled system in which the HOBM is in the singular configuration. In the case of the conventional usage of the HOBM, this configuration does not present any inconvenience, since the operator will not move the payload in the radial direction. He will remove the load from the singular position of the manipulator and then perform the necessary movements. However, in a coupled system, it is indispensable to take this into account when planning a trajectory of the cobot, since such a movement cannot be

performed. Thus, it is necessary to avoid not only the singular configurations of the cobot but also of the HOBM. Therefore, the moving range of the distal arm of the HOBM is limited that it cannot pass the singularity position.

Figure 5-5 shows the workspace of the HOBM after the previous modifications where the vertical axis of the HOBM is situated at the original point.

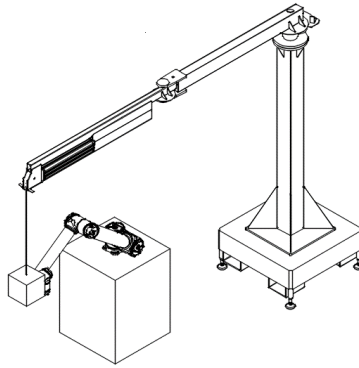


**Figure 5-4.** Coupled system in which the HOBM is in the singular configuration.

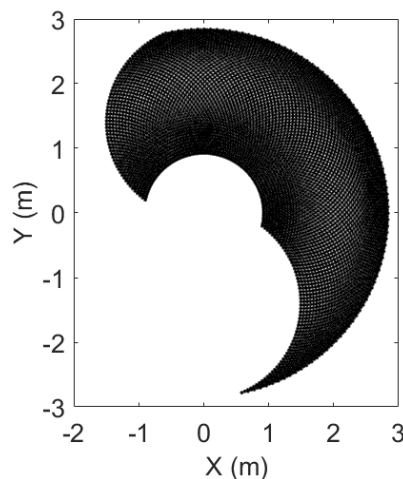


**Figure 5-5.** Workspace of the HOBM after modification.

## ***5.2 Dynamic analysis of the coupled system and methods for reducing oscillations in the final phase of the trajectories***

### **5.2.1 Dynamic modelling and oscillation analysis of the coupled system in the final phase of generated trajectories**

The dynamic performance of the coupled system is quite complicated since the system is formed by two units and they are flexibly linked through the cable-pulley system. Thus, the coupled system has some phenomena which will not occur when the two devices work independently. For example, when cobot is moving through a prescribed trajectory, after the cobot stop moving, the HOBM will still move due to inertial effect. Hence the HOBM will oscillate and exert noticeable forces on the cobot which may

lead to the damage of the cobot. Therefore, it is necessary to investigate the dynamic behavior of the coupled system.

In order to carry out the dynamic analysis of the HOBM-cobot coupled system, a dynamic model of the system has been developed via multi-body dynamic simulation software ADAMS (Figure 5-6). The 3D geometric model of the HOBM (without cable-pulley system) and the UR10 was firstly built in CATIA and then imported in ADAMS. In order to simulate the flexibility of the cable, the cable-pulley system was modeled by using the Cable toolkit in ADAMS.

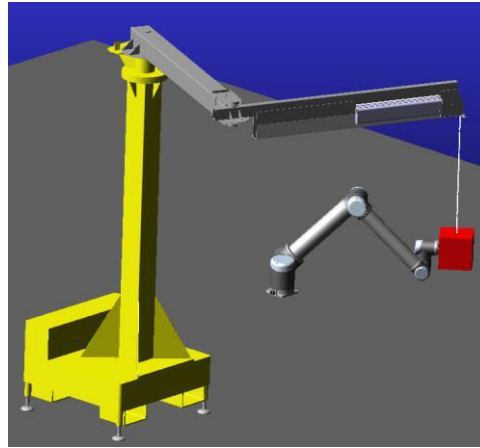


**Figure 5-6.** ADAMS model of the coupled system.

For performing the oscillation analysis of the coupled system, the motion of the robot must be prescribed at first. In this analysis, the cobot is assumed to perform a pick-and-place task with a payload of 30 kg and the prescribed path is part of a circle. This means that, for all six joints of UR10, only the first joint has motion and the rest of the joints have constant angles. The constant angles of the UR10 are  $\theta_2=-45^\circ$ ,  $\theta_3=90^\circ$ ,  $\theta_4=-225^\circ$ ,  $\theta_5=90^\circ$ , and  $\theta_6=0^\circ$ . And the first joint of the UR10 follows a trapezoidal profile (Figure 5-7) in joint space which is often used in robot trajectory planning. Usually, a trapezoidal trajectory consists of three phases: acceleration phase, constant speed phase, and deceleration phase. The motion of the first joint of UR10 can be formulized as following:

$$\theta_1(t) = \begin{cases} \theta_1^i + \frac{1}{2}t^2\alpha & (0 \leq t \leq \tau) \\ \theta_1^i + (t - \frac{\tau}{2})\omega & (\tau \leq t \leq t_f - \tau) \\ \theta_1^f - \frac{1}{2}(t_f - t)^2\alpha & (t_f - \tau \leq t \leq t_f) \end{cases} \quad (5-1)$$

where  $\theta_1^i = -40^\circ$  is the initial angle,  $\theta_1^f = 40^\circ$  is the final angle,  $\tau$  is the time for acceleration and deceleration,  $t_f$  is the total time of the trajectory,  $\omega$  is the constant speed in the second phase, and  $\alpha$  is the absolute value of acceleration.

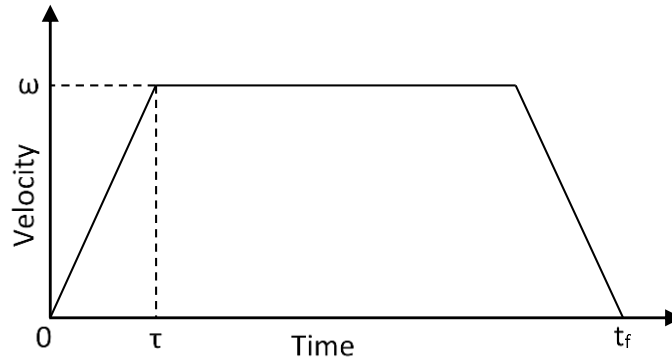


**Figure 5-7.** Trapezoidal trajectory

It should be noticed that the dynamic effects of the coupled system highly rely on the velocity and acceleration of the motion. Therefore, in order to investigate the dynamic effects of the coupled system in a wide range, eight different trajectories were chosen based on the motion function Eq. (5-1), and the parameters of the trajectories are shown in Table 5-1. It can be seen that the first four trajectories are as the reference trajectories with different constant velocities and accelerations, and the last four trajectories have the same constant velocities with the previous ones but have more significant accelerations and decelerations.

**Table 5-1.** Parameters of the trajectories.

Trajectory	1	2	3	4	5	6	7	8
$t_f (s)$	12.15	10	6.08	5	10	8.24	5	4.13
$\omega(\text{deg}/s)$	9.41	11.43	18.8	22.86	9.41	11.43	18.8	22.86
$\alpha(\text{deg}/s^2)$	2.58	3.8	10.31	15.24	6.27	9.25	25.1	36.82

The total simulation time is 20 seconds. Oscillations of the proximal arm of the HOBM and the distal arm of the HOBM are shown in Figure 5-8 and Figure 5-9 respectively. It can be seen that the trajectories with larger acceleration and deceleration have a more significant oscillation after stopping the cobot. The reason for the occurrence of this oscillation is: the cobot is linked with HOBM through a cable and when the cable is parallel to the rotational axes of the HOBM, the cable force will not cause the movement of the HOBM since no moment with respect to the rotational axes is generated by the cable. However, when the cobot start to move, the cable is no longer parallel to the rotational axes of the HOBM, moments will be generated by the cable which lead the movement of the HOBM; after the cobot stops, the arms of the HOBM will still rotate because of its inertia and the directions of the moment induced by the cable will be changed as the movement of the HOBM which leads to the oscillation. If the cobot deaccelerates in a very short time, because of the HOBM still remains in a state with high velocity and the moment generated by the cable is limited by the cable force, a large oscillation will occur.

Another thing has to be concerned is the forces exerted on the cobot induced by the inertia effect of the HOMB which are shown in Figure 5-10. Similar to the movement

of the HOBM, the force becomes more significant as the cobot has large acceleration and deceleration movements. It is because that when the cable is perpendicular to the ground, it exerts a force which is quantitatively equal to the gravity of the payload but in the opposite direction. However, as the oscillation occurs or the HOBM does not strictly follow the movement of the cobot, the force exerted by the cable is no longer collinear with the gravity, which leads to an extra load on the cobot.

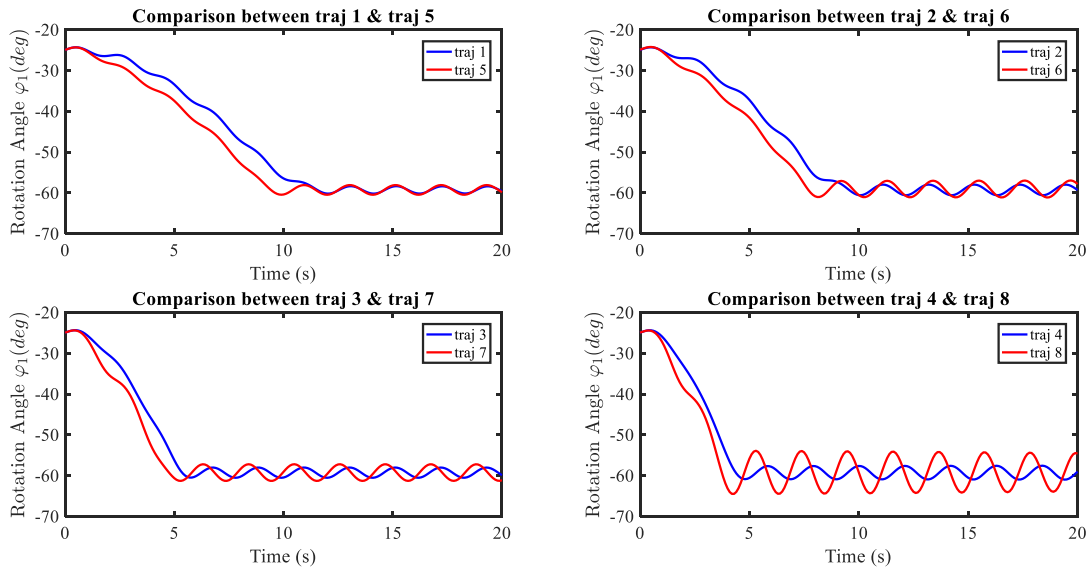


Figure 5-8. Oscillation of the proximal arm of the HOBM

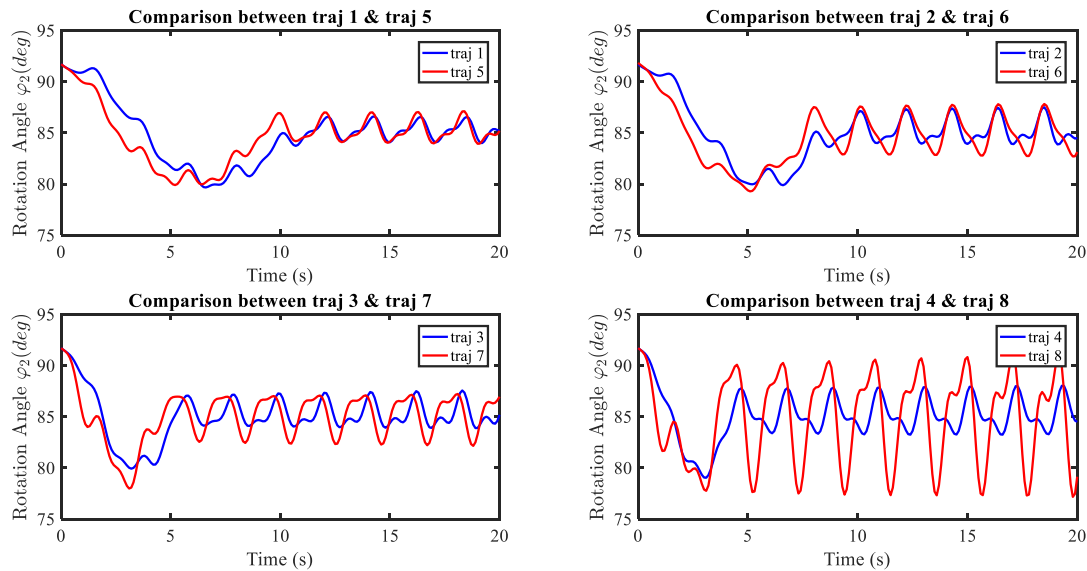
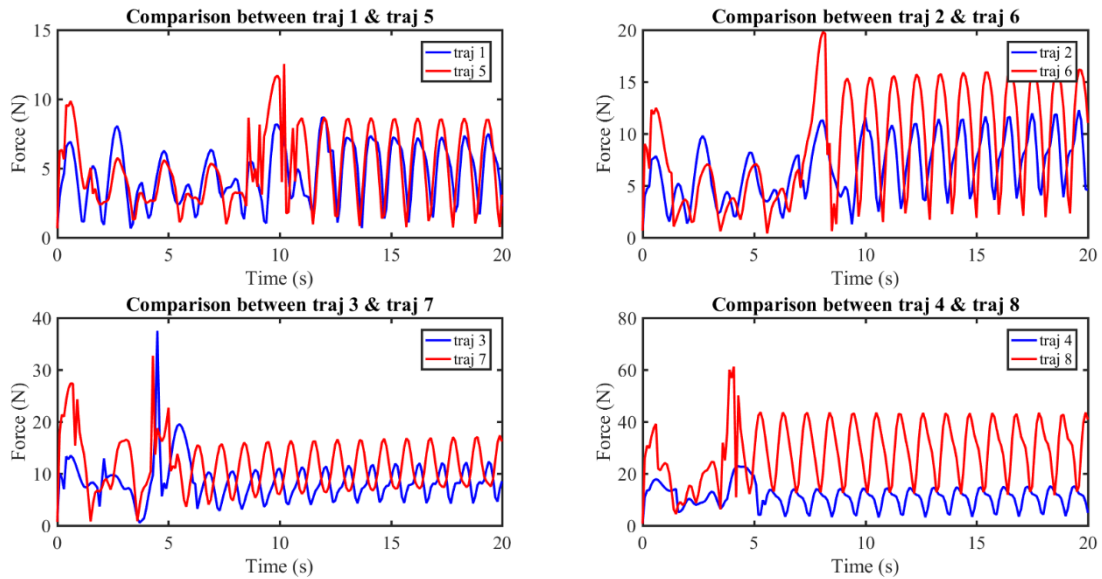


Figure 5-9. Oscillation of the distal arm of the HOBM





**Figure 5-10.** Force applied on the cobot due to the inertia effect of the HOBM

### 5.2.2 Redaction of oscillations in the final phase of generated trajectories by introducing a rigid vertical axis

From dynamic simulations of the coupled system, it can be seen that the oscillations of the HOBM in the final phase of the trajectories will exert extra loads on the cobot and in some severe situations, the cobot may engage launch the emergency stop for the its safety while being subjected to large external force.

The simplest method for reducing the oscillations of the HOBM is to constrain its movement by linking the cobot and HOBM through a rigid link. In this case, the HOBM will strictly follow the motion of the cobot which means no oscillation will occur.

For applying this solution, a rigid telescopic axis (Figure 5-13) has been designed for connecting the HOBM and UR10. The rigid axis is comprised of two hollow cylindrical links where the inner diameter of one of the links is equal to the outer diameter of the other one. Hence the translational movement of the two links is allowed as well as the rotational movement about the vertical axis when the payload is manipulated by the cobot. Each of the links is jointed with the end effector of the HOBM and of UR10 respectively.

However, although the oscillations in the final phase of the trajectory can be eliminated due to the rigid connection, it should be noticed that the cobot will be still affected by the inertia of the HOBM since they are rigidly connected.

In order to investigate the inertial effect of the HOBM on the cobot after the rigid connection, simulations were carried out by adding the vertical axis in the previously built ADAMS model. For the simulations, the same trajectories were used as shown in Table 5-1 and the comparisons of the forces applied on the cobot before and after the implementation of the rigid axis are shown in Figure 5-12. It can be seen that, although the force exerted on the cobot after its movement is zero since the oscillation is no longer occurs, however, the force is still significant during the acceleration and

deceleration phases. Especially for the trajectories with large acceleration and deceleration, the maximum exerted forces are much larger than the cases without implementation of the rigid axis.

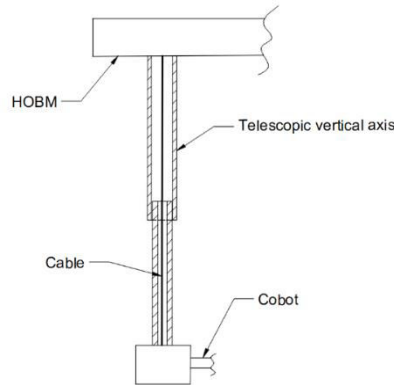


Figure 5-11. The rigid axis connecting cobot and HOBM.

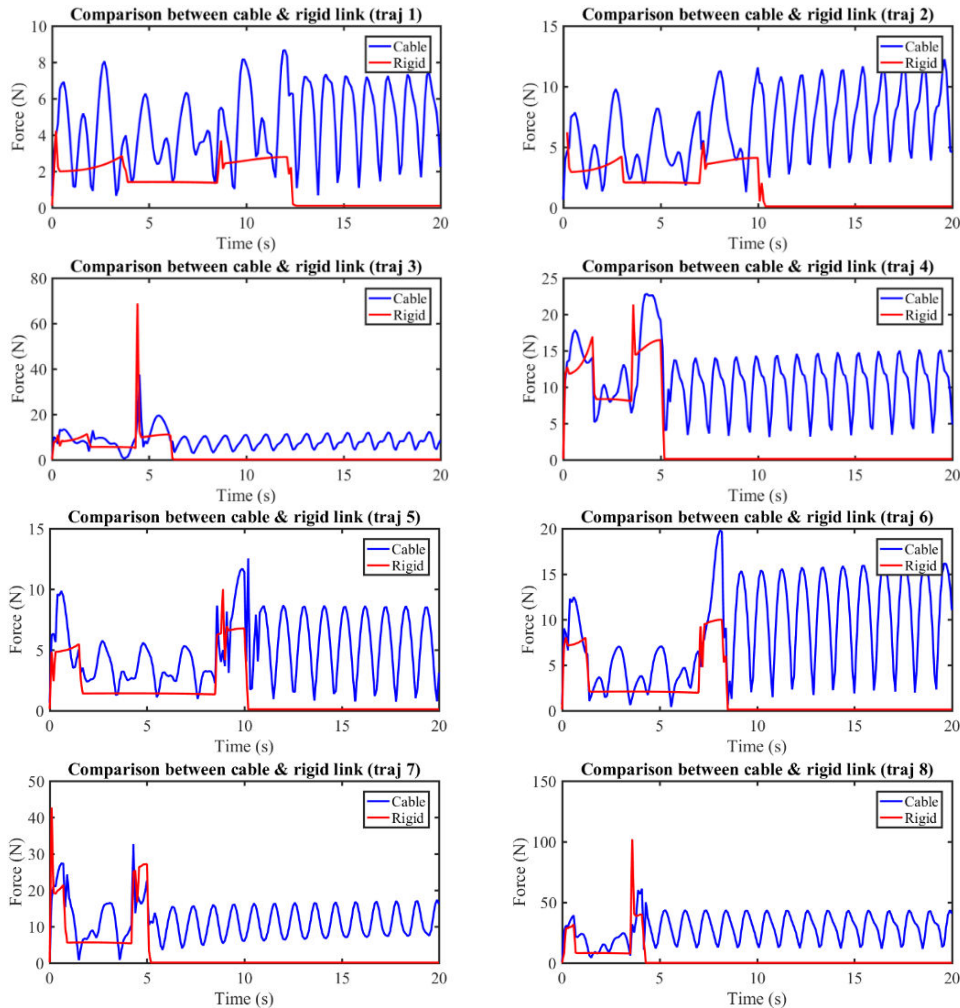


Figure 5-12. Comparison of the force applied on the cobot due to the inertia effect of the HOBM before and after the implementation of the rigid axis

Thus, when a telescopic axis is implemented on the coupled system, it is necessary to take into account the limited acceleration of the cobot in order to limit the inertial effects of the HOBM on the cobot.

### **5.2.3 Reduction of oscillations in the final phase of generated trajectories by introducing damping moments**

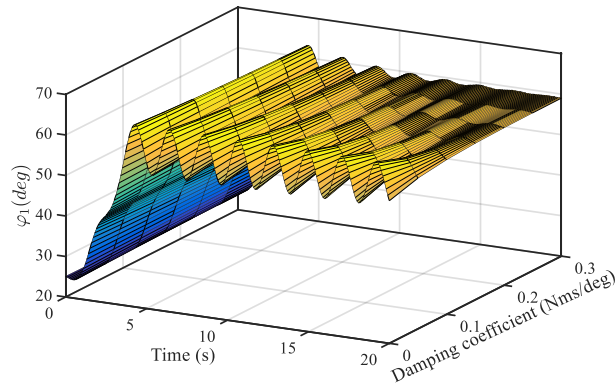
Apart from the application of rigidly linking the cobot and HOBM by the vertical axis, another promising method for reducing the oscillation of the HOBM in the final phase of the trajectory is to introduce damping moments on the joints of HOBM.

The damping moments are generated by two rotary dampers installed on the joints of HOBM. The dampers will generate damping moments which impede the movements of the HOBM. Therefore, after introducing the damping moments on HOBM's joints, its oscillations in the final phase of the trajectory will decrease.

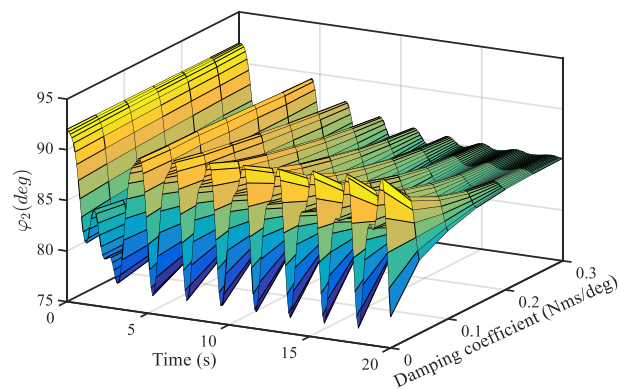
In order to investigate the effect of the damping moments in the reduction of the oscillation, simulations have been conducted based on the ADAMS model presented in section 5.2.1. While performing the simulations, the damping coefficients on the two joints are the same. For evaluation of the influence of the damping coefficients different values were applied. It has been assumed that the damping moments are linearly related to the joints' rotational velocities. With regards to the trajectory, in these simulations, the most intense one in Table 5-1 has been chosen which is trajectory 8.

Figure 5-13 shows the oscillations of the two arms of the HOBM after introducing damping moments. It can be seen clearly that the oscillations of the arms gradually decrease and the reduction is more significant with higher the damping coefficient.

Although the damping moments show good performance in terms of the reduction of the oscillation, however, it should be noticed the force applied on the cobot by the HOBM is still large during the moving phase of the cobot. The force applied on the cobot after introducing damping moments is shown in Figure 5-14. It can be seen that the force in the final phase of the trajectory is decreased due to the reduction of the oscillation. And the reduction is more obvious with higher damping coefficient. However, during the phase where the cobot is moving, the force still remains significant.



(a) proximal arm



(b) distal arm

**Figure 5-13.** Oscillations of the rotating arms of the HOBM after introducing damping moments.

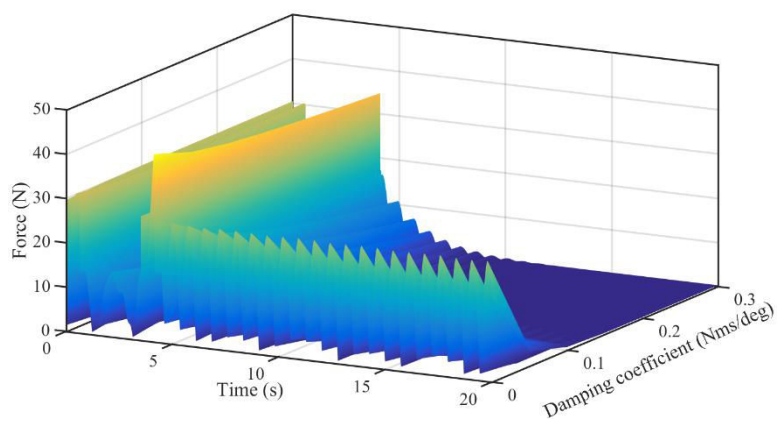


**Figure 5-14.** Force applied on the cobot after introducing damping moments

### 5.3 Dynamic modeling of the HOBM-cobot coupled system for determining admissible trajectories of the cobot

From the simulation results in the previous section, it can be seen that the inertia of the HOBM has a great impact on the cobot. Although after introducing a rigid telescopic axis and damping moments, the oscillation of the HOBM in the final phase of the trajectory has been reduced. However, the force exerted by HOBM in the motion phase of the cobot is still noticeable and this force highly depends on the acceleration of the cobot.

Therefore, in this section, a dynamic model of the coupled system was built via Matlab and for preventing the damage on cobot caused by HOBM, the admissible trajectory of the cobot was determined taking into account the inertia effect of the HOBM.

#### 5.3.1 Dynamic modeling of the cobot UR10

Let us first build the dynamic model of the cobot UR10 having six degrees-of-freedom. Figure 5-15 shows the coordinate systems of each joint of the cobot UR10 according to the Denavit–Hartenberg notation.

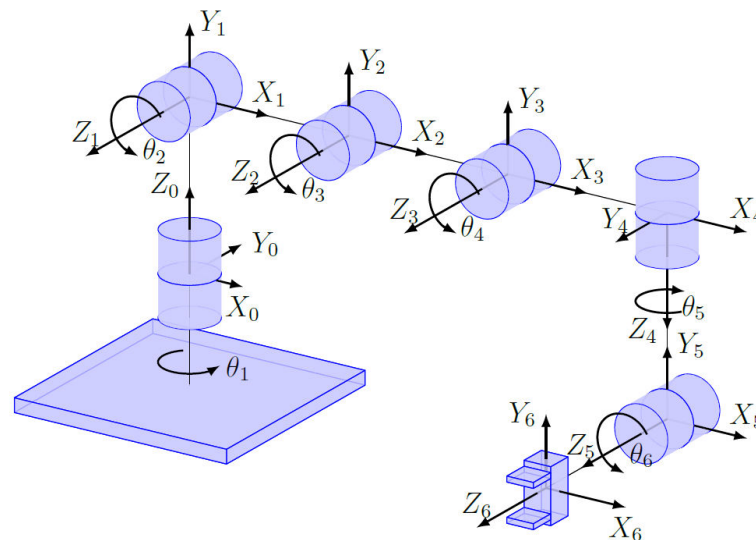


**Figure 5-15.** The Denavit–Hartenberg parameterization of the cobot UR10.

Let us now consider the derivation of the velocity term for a point on a link of a robot. Using  $p_i$  to represent a point on any link  $i$  of the robot relative to frame  $i$ , we can express the position of the point by multiplying the vector with the transformation matrix representing its frame:

$$\mathbf{p}_i = {}^0\mathbf{A}_i \mathbf{r}_i \quad (5-2)$$

where  ${}^0\mathbf{A}_i = {}^0\mathbf{A}_1 {}^1\mathbf{A}_2 \dots {}^{i-1}\mathbf{A}_i$  is the transformation between the base of the robot and point on any link  $i$ ;  $\mathbf{r}_i$  represents the coordinates of point  $i$  relative to frame  $i$ ;  $\mathbf{p}_i$  is the matrix that represents the same coordinates relative to the fixed frame.

Here we will use the Denavit-Hartenberg transformation matrices  ${}^{i-1}\mathbf{A}_i$  :

$${}^{i-1}\mathbf{A}_i = \begin{bmatrix} \cos \theta_i & -\sin \theta_i \cos \alpha_i & \sin \theta_i \sin \alpha_i & a_i \cos \theta_i \\ \sin \theta_i & \cos \theta_i \cos \alpha_i & -\cos \theta_i \sin \alpha_i & a_i \sin \theta_i \\ 0 & \sin \alpha_i & \cos \alpha_i & d_i \\ 0 & 0 & 0 & 1 \end{bmatrix} \quad (5-3)$$

where  $\theta_i$ ,  $\alpha_i$ ,  $a_i$  and  $d_i$  are the DH parameters of the robot.

The DH parameters for cobot UR10 are shown in Table 5-2.

**Table 5-2.** Denavit-Hartenberg parameters of UR10

Joint $i$	$\theta_i$ (rad)	$a_i$ (m)	$d_i$ (m)	$\alpha_i$ (rad)
1	$\theta_1$	0	0.1273	$\pi/2$
2	$\theta_2$	-0.612	0	0
3	$\theta_3$	-0.572	0	0
4	$\theta_4$	0	0.163941	$\pi/2$
5	$\theta_5$	0	0.1157	$-\pi/2$
6	$\theta_6$	0	0.0922	0

The derivative of an  ${}^{i-1}\mathbf{A}_i$  matrix for a revolute joint with respect to its joint variable  $\theta_i$  is:

$$\frac{\partial ({}^{i-1}\mathbf{A}_i)}{\partial \theta_i} = \begin{bmatrix} -\sin \theta_i & -\cos \theta_i \cos \alpha_i & \cos \theta_i \sin \alpha_i & -a_i \sin \theta_i \\ \cos \theta_i & -\sin \theta_i \cos \alpha_i & \sin \theta_i \sin \alpha_i & a_i \cos \theta_i \\ 0 & 0 & 0 & 0 \\ 0 & 0 & 0 & 0 \end{bmatrix} \quad (5-4)$$

However, this matrix can be broken into a constant matrix  $\mathbf{Q}_i$  [123] and the  ${}^{i-1}\mathbf{A}_i$  matrix such that

$$\frac{\partial \mathbf{A}_i}{\partial \theta_i} = \mathbf{Q}_i {}^{i-1}\mathbf{A}_i \quad (5-5)$$

Using  $q_i$  to represent the joint variables ( $\theta_1, \theta_2, \dots$ , for revolute joints), and extending the same differentiation principle to the  ${}^0\mathbf{A}_i$  matrix, differentiated with respect to only one variable  $q_i$  gives

$$\mathbf{U}_{ij} = \frac{\partial {}^0\mathbf{A}_i}{\partial q_j} = \frac{\partial ({}^0\mathbf{A}_1 {}^1\mathbf{A}_2 \dots {}^{i-1}\mathbf{A}_i)}{\partial q_j} = {}^0\mathbf{A}_1 {}^1\mathbf{A}_2 \dots \mathbf{Q}_j {}^{j-1}\mathbf{A}_j \dots {}^{i-1}\mathbf{A}_i \quad (5-6)$$

Please note that since  ${}^0\mathbf{A}_i$  is differentiated only with respect to one variable  $q_i$  there is only one  $\mathbf{Q}_j$ . Higher order derivatives can be formulated similarly from

$$\mathbf{U}_{ijk} = \frac{\partial \mathbf{U}_{ij}}{\partial q_k} \quad (5-7)$$

Since the velocity of the point is a function of the velocities of all the joints  $\dot{q}_1, \dot{q}_2, \dots, \dot{q}_6$ . Therefore, by differentiating Eq. (5-2) with respect to all the joint variables  $q_j$  yields the velocity of the point:

$$\mathbf{V}_i = \frac{d(\mathbf{p}_i)}{dt} = \sum_{j=1}^i \left( \frac{\partial ({}^0\mathbf{A}_i)}{\partial q_j} \frac{dq_j}{dt} \right) \cdot \mathbf{r}_i = \sum_{j=1}^i \left( \mathbf{U}_{ij} \frac{dq_j}{dt} \right) \cdot \mathbf{r}_i \quad (5-8)$$

Since  $\mathbf{V}_i$  has three components of  $\dot{x}_i, \dot{y}_i, \dot{z}_i$ , it can be written as

$$\mathbf{V}_i \mathbf{V}_i^T = \begin{bmatrix} \dot{x}_i \\ \dot{y}_i \\ \dot{z}_i \end{bmatrix} \begin{bmatrix} \dot{x}_i & \dot{y}_i & \dot{z}_i \end{bmatrix} = \begin{bmatrix} \dot{x}_i^2 & \dot{x}_i \dot{y}_i & \dot{x}_i \dot{z}_i \\ \dot{y}_i \dot{x}_i & \dot{y}_i^2 & \dot{y}_i \dot{z}_i \\ \dot{z}_i \dot{x}_i & \dot{z}_i \dot{y}_i & \dot{z}_i^2 \end{bmatrix} \quad (5-9)$$

and

$$\text{Trace}(\mathbf{V}_i \mathbf{V}_i^T) = \text{Trace} \left( \begin{bmatrix} \dot{x}_i^2 & \dot{x}_i \dot{y}_i & \dot{x}_i \dot{z}_i \\ \dot{y}_i \dot{x}_i & \dot{y}_i^2 & \dot{y}_i \dot{z}_i \\ \dot{z}_i \dot{x}_i & \dot{z}_i \dot{y}_i & \dot{z}_i^2 \end{bmatrix} \right) = \dot{x}_i^2 + \dot{y}_i^2 + \dot{z}_i^2 \quad (5-10)$$

The total kinetic energy of link  $i$  can be obtained by:

$$K_i = \frac{1}{2} \text{Trace} \left( \sum_{p=1}^i \sum_{r=1}^i \mathbf{U}_{ip} \mathbf{I}_i \mathbf{U}_{ir}^T \dot{q}_p \dot{q}_r \right) \quad (5-11)$$

where  $\mathbf{I}_i$  is the Pseudo Inertia Matrix[123].

The potential energy of the system is the sum of the potential energies of each link and can be written as

$$P = \sum_{i=1}^n P_i = \sum_{i=1}^n \left[ -m_i \mathbf{g}^T ({}^0\mathbf{A}_i \mathbf{r}_i) \right] \quad (5-12)$$

where  $\mathbf{g}$  is the gravity matrix and  $\mathbf{r}_i$  is the location of the center of mass of a link relative to the frame representing the link  $i$ . Obviously, the potential energy must be a scalar

quantity, and thus  $\mathbf{g}^T$ , which is a (1x4) matrix, multiplied by the position vector ( ${}^0\mathbf{A}_i\mathbf{r}_i$ ), which is a (4x1) matrix, yields a single scalar quantity. Please also note that the values in the gravity matrix are dependent on the orientation of the reference frame.

The Lagrangian is then

$$L = K - P = \frac{1}{2} \sum_{i=1}^n \sum_{p=1}^i \sum_{r=1}^i \text{Trace}(\mathbf{U}_{ip} \mathbf{I}_i \mathbf{U}_{ir}^T \dot{q}_p \dot{q}_r) - \sum_{i=1}^n [-m_i \mathbf{g}^T ({}^0\mathbf{A}_i \mathbf{r}_i)] \quad (5-13)$$

The Lagrangian can now be differentiated in order to form the dynamic equations of motion by the following:

$$\tau_i = \frac{d}{dt} \left( \frac{\partial L}{\partial \dot{q}_i} \right) - \frac{\partial L}{\partial q_i} \quad (5-14)$$

By substituting Eq. (5-13) into Eq. (5-14), the final dynamic equations of motion for the cobot can be summarized as follows:

$$\tau_i = \sum_{j=1}^n D_{ij} \ddot{q}_j + \sum_{j=1}^n \sum_{k=1}^n D_{ijk} \dot{q}_j \dot{q}_k + D_i \quad (5-15)$$

where

$$D_{ij} = \sum_{p=\max(i,j)}^n \text{Trace}(\mathbf{U}_{pj} \mathbf{I}_p \mathbf{U}_{pi}^T)$$

$$D_{ijk} = \sum_{p=\max(i,j,k)}^n \text{Trace}(\mathbf{U}_{pj} \mathbf{I}_p \mathbf{U}_{pi}^T)$$

$$D_i = \sum_{p=i}^n (-m_p \mathbf{g}^T \mathbf{U}_{pi} \mathbf{r}_p)$$

In Eq. (5-15), the first part is the angular acceleration-inertia terms, the second part is the Coriolis and centrifugal terms, and the last part is the gravity term.

The mass-inertia properties of the cobot UR10 is shown in Table 5-3.

The dynamic model of the cobot UR10 was created by using the described relationships. The obtained expressions are very voluminous and they cannot be presented in the manuscript.



**Table 5-3.** Mass-inertia characteristics of UR10

Link $i$	$m_i$ (kg)	$l_i$ (m)	$r_{S_i} [x_{S_i}, y_i, z_{S_i}]$ (m)	$I_{x_i}$ (kgm <sup>2</sup> )	$I_{y_i}$ (kgm <sup>2</sup> )	$I_{z_i}$ (kgm <sup>2</sup> )
1	1.35	0.038	[0, 0.0116, 0.0786]	$4.62 \times 10^{-3}$	$5.40 \times 10^{-3}$	$4.88 \times 10^{-3}$
2	3.82	0.612	[0, 0.251, 0.0844]	$1.20 \times 10^{-1}$	$8.08 \times 10^{-1}$	$6.96 \times 10^{-1}$
3	2.04	0.572	[0, 0.258, 0.0566]	$8.03 \times 10^{-3}$	$2.96 \times 10^{-1}$	$2.90 \times 10^{-1}$
4	0.32	0.164	[0, 0.009, 0.0463]	$5.35 \times 10^{-4}$	$4.79 \times 10^{-4}$	$4.07 \times 10^{-4}$
5	0.32	0.116	[0, 0.010, 0.0464]	$5.37 \times 10^{-4}$	$4.82 \times 10^{-4}$	$4.06 \times 10^{-4}$
6	0.07	0.092	[0, 0, 0.0126]	$5.72 \times 10^{-5}$	$5.95 \times 10^{-5}$	$6.57 \times 10^{-5}$

### 5.3.2 Dynamic modelling of the HOBM

Since the arms of the HOBM have only rotational movements about the vertical axis, hence it can be seen as a two-link serial manipulator as shown in Figure 5-16.

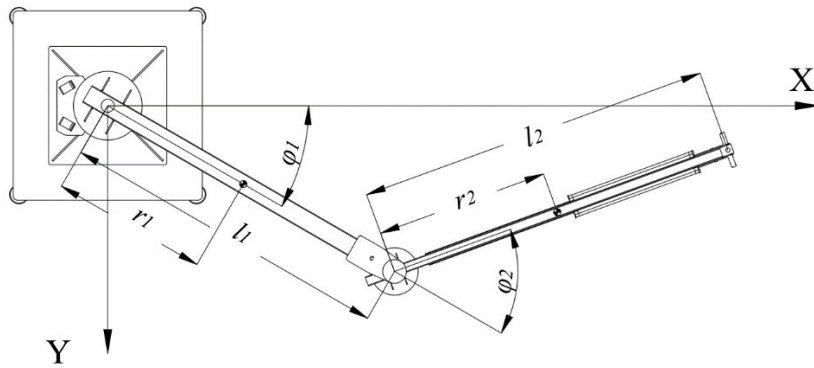


**Figure 5-16.** Representation of the HOBM

According to the geometrical relationship, the coordinates of the end effector of the HOBM in the horizontal plane can be obtained by:

$$\begin{cases} x = l_1 \cos \varphi_1 + l_2 \cos(\varphi_1 + \varphi_2) \\ y = l_1 \sin \varphi_1 + l_2 \sin(\varphi_1 + \varphi_2) \end{cases} \quad (5-16)$$

where  $\varphi_1$  and  $\varphi_2$  are the rotational angles of the arms of HOBM, and  $l_1$  and  $l_2$  are the length of the arms of HOBM as shown in Figure 5-16.

Then the Jacobian matrix of the HOBM is:

$$\mathbf{J}_{HOBM} = \begin{bmatrix} -l_1 \sin \varphi_1 - l_2 \sin(\varphi_1 + \varphi_2) & -l_2 \sin(\varphi_1 + \varphi_2) \\ l_1 \cos \varphi_1 + l_2 \cos(\varphi_1 + \varphi_2) & l_2 \cos(\varphi_1 + \varphi_2) \end{bmatrix} \quad (5-17)$$

The kinetic energy of link 1 and link 2 of the HOBM are:

$$T_1 = \frac{1}{2} m_1 r_1^2 \dot{\phi}_1^2 + \frac{1}{2} I_1 \dot{\phi}_1^2 \quad (5-18)$$

$$T_2 = \frac{1}{2} I_2 (\dot{\phi}_1 + \dot{\phi}_2)^2 + \frac{1}{2} m_2 \left\{ \left[ -l_1 \dot{\phi}_1 \sin \varphi_1 - l_2 (\dot{\phi}_1 + \dot{\phi}_2) \sin (\varphi_1 + \varphi_2) \right]^2 + \left[ l_1 \dot{\phi}_1 \cos \varphi_1 + l_2 (\dot{\phi}_1 + \dot{\phi}_2) \cos (\varphi_1 + \varphi_2) \right]^2 \right\} \quad (5-19)$$

where  $m_i$ ,  $I_i$ , and  $r_i$  ( $i=1, 2$ ) denote the link  $i$ 's mass, moment of inertia, and distance from the center of mass to the pivot respectively.

And the total kinetic energy of the HOBM is:

$$T = T_1 + T_2 \quad (5-20)$$

Because the arms of the HOBM have no vertical movement which means that no matter how the rotational angle of the HOBM, the gravitational potential energy always stays the same, i.e.

$$\frac{\partial V}{\partial \varphi_i} = 0 \quad (i = 1, 2) \quad (5-21)$$

According to Lagrange's equation, the dynamic equation of the HOBM can be obtained by:

$$\tau_i = \frac{d}{dt} \left( \frac{\partial T}{\partial \dot{\phi}_i} \right) - \frac{\partial T}{\partial \varphi_i} + \frac{\partial V}{\partial \varphi_i} \quad (i = 1, 2) \quad (5-22)$$

Combining Eq. (5-18) – (5-22), the dynamic equation of the HOBM can be rewritten as:

$$\tau_1^{HOBM} = \left[ m_1 r_1^2 + m_2 (l_1^2 + r_2^2 + 2l_1 r_2 \cos \varphi_2) + I_1 + I_2 \right] \ddot{\phi}_1 + \left[ m_2 (r_2^2 + l_1 r_2 \cos \varphi_2) + I_2 \right] \ddot{\phi}_2 - m_2 l_1 r_2 \sin \varphi_2 \dot{\phi}_2^2 - 2m_2 l_1 r_2 \sin \varphi_2 \dot{\phi}_1 \dot{\phi}_2 \quad (5-23)$$

$$\tau_2^{HOBM} = \left[ m_2 (r_2^2 + l_1 r_2 \cos \varphi_2) + I_2 \right] \ddot{\phi}_1 + (m_2 r_2^2 + I_2) \ddot{\phi}_2 + m_2 l_1 r_2 \sin \varphi_2 \dot{\phi}_1^2 \quad (5-24)$$

The physical characteristics of the HOBM are shown in Table 5-4.

**Table 5-4.** Mass-inertia characteristics of the HOBM

Link $i$	$m_i$ (kg)	$l_i$ (m)	$r_{S_i}$ (m)	$I_{S_i}$ (kgm <sup>2</sup> )
1	30.97	1.4	0.57	9.28
2	23.56	1.5	0.74	5.21
3	2.13	0.6	0.3	0.06

### 5.3.3 Loads of inertial forces on the cobot for the HOBM with a vertical rigid axis

The behavior of the coupled system in a static mode, when the velocities of links the HOBM are limited, does not present any special problem. In this mode, the inertial forces are significantly lower than the gravitational ones. The payload is completely balanced by the HOBM and the cobot assumes low loads. However, when increasing the accelerations, the inertia forces also increase and, respectively, the efficiency of gravitational balancing decreases. Therefore, the HOBM with massive links creates additional loads on the cobot. Let's consider the inertial forces of the HOBM exerted on the UR10.

In the coupled system, the payload is moved by the cobot. Thus, knowing the vector  $\theta$  of joint angles of the cobot, the vector  $\dot{\mathbf{x}}$  of Cartesian velocities of its end effector can be determined from:

$$\dot{\mathbf{x}}_{cobot} = \mathbf{J}_{cobot} \dot{\theta} \quad (5-25)$$

where,  $\mathbf{J}_{cobot}$  is the Jacobian matrix of the cobot.

The displacements and velocities of the payload are the input parameters for the HOBM. Hence,

$$\dot{\phi} = \mathbf{J}_{HOBM} \dot{\mathbf{x}}_{cobot} \quad (5-26)$$

where,  $\phi$  is the vector of joint angles of the HOBM.

Thus, knowing the vector  $\phi$  of joint angles, the inertial forces and moments of the HOBM can be determined and the loads  $\tau_{HOBM}$  due to these forces and moments in the joints will also be established by using Eq. (5-23) -(5-24).

Now, the force-torque vector  $\mathbf{F}_{HOBM}$  acting on the payload due to the HOBM can be expressed by the relationship:

$$\mathbf{F}_{HOBM} = \mathbf{J}_{HOBM}^{-T} \tau_{HOBM} \quad (5-27)$$

It should also be noticed that, although the gravity of the payload is compensated by the HOBM, the inertia effect of the payload should still be taken into account especially

when it has large acceleration. In the dynamic model, the payload is considered as a point mass and its inertial force can be determined by:

$$\mathbf{F}_{payload}^{inertia} = m_{payload} \mathbf{a}_{payload} \quad (5-28)$$

where  $\mathbf{a}_{payload}$  is the acceleration vector of the payload.

Hence, the total load on the end effector of the cobot is:

$$\mathbf{F}_{total} = \mathbf{F}_{HOBM} + \mathbf{F}_{payload} \quad (5-29)$$

For validating the correctness of the dynamic model of the HOBM-cobot coupled system after introducing the rigid telescopic axis, a Simulink model has been built via Matlab and simulation results have been compared with the results of the ADAMS model. The mass of the payload is 30kg and the trajectory parameters are the same as the trajectory 8 shown in Table 5-1.

Figure 5-17 shows the comparison of forces exerted on the cobot simulated by ADAMS and Matlab models. It can be seen that the difference between the two models in the acceleration phase is very small, and the larger difference in the constant speed phase is due to the Coriolis and centripetal effect of the payload.

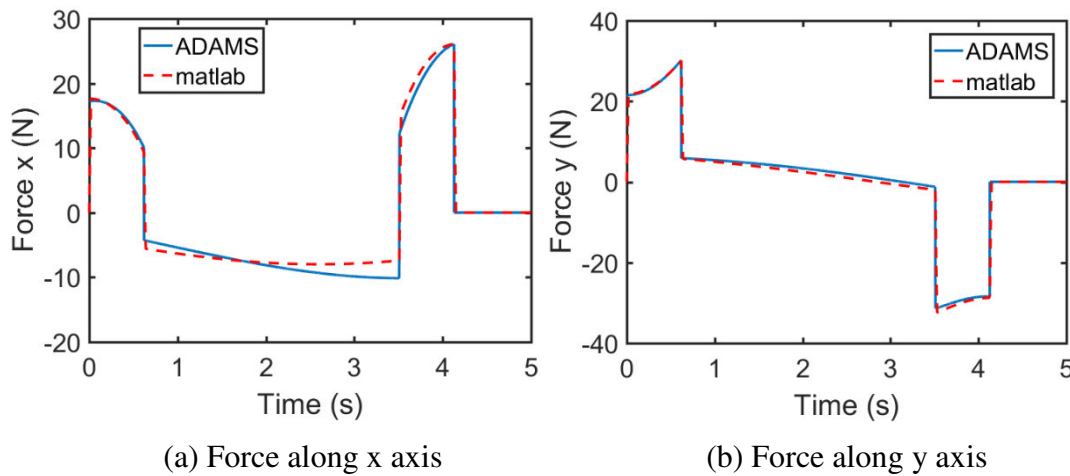


**Figure 5-17.** Comparison between the ADAMS and Matlab models

### 5.3.4 Loads of inertial forces on the cobot after introducing damping moments

Unlike the case where HOBM and cobot are linked with a rigid telescopic axis, while cobot and HOBM are only link through the cable, the coordinates of the end effectors of HOBM and cobot in x-y plane can be different.

Let us define the vector points from the end effector of HOBM to the end effector of cobot as:

$$\mathbf{r} = \mathbf{x}_{cobot} - \mathbf{x}_{HOBM} \quad (5-30)$$

where  $\mathbf{x}_{HOBM}$  is the Cartesian coordinate of the HOBM's end effector.

When the coordinates of the end effectors of HOBM and cobot in x-y plane are not the same, the force generated by the cable is no longer parallel to the z axis. Hence the cable force will generate torques which lead to the oscillation of the HOBM's links. Figure 5-18 shows the forces applied on the end effector of HOBM when the cable is not parallel to the z axis. It can be seen that the cable force  $\mathbf{F}_{cable}$  can be decomposed into three components along the local frame of the distal arm of the HOBM. The components  $F_{cable}^y$  and  $F_{cable}^x$  will lead to the torques on the first and second joints of the HOBM, respectively.

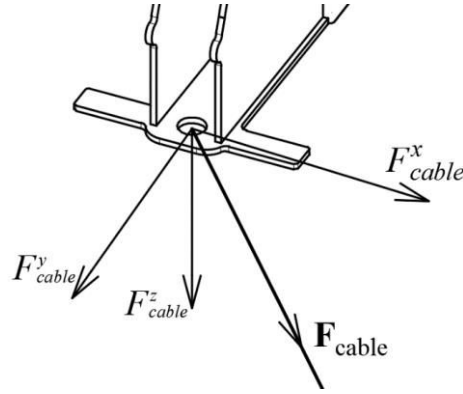


**Figure 5-18.** Forces applied on the end effector of HOBM

The cable force applied on the end effector of HOBM can be obtained by:

$$\mathbf{F}_{cable} = \frac{m_{payload} \mathbf{g} \mathbf{r}}{|\mathbf{r}|} \quad (5-31)$$

Then, the torques applied on the joints of HOBM induced by the cable force is:

$$\boldsymbol{\tau}_{cable}^{HOBM} = \mathbf{J}_{HOBM} \mathbf{F}_{cable} \quad (5-32)$$

After introducing damping moments on the joints of the HOBM, due to the effect of dissipation, the oscillation of the HOBM in the final phase of the trajectory will be reduced. In simulations, it is assumed that the damping moments have a linear relationship with joint velocities:

$$\boldsymbol{\tau}_{damping}^{HOBM} = \mathbf{c} \dot{\boldsymbol{\phi}} \quad (5-33)$$

where  $\mathbf{c}$  is a diagonal matrix indicating the damping coefficients.

Thus, the total torques applied on the HOBM is:

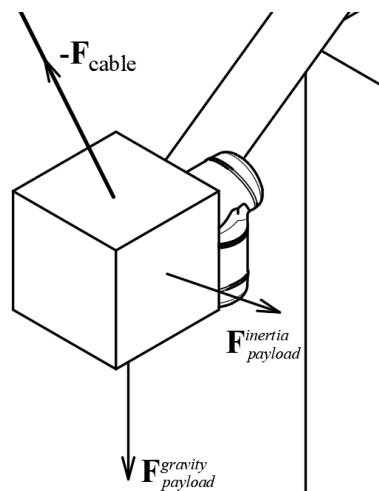
$$\boldsymbol{\tau}^{HOBM} = \boldsymbol{\tau}_{damping}^{HOBM} + \boldsymbol{\tau}_{cable}^{HOBM} \quad (5-34)$$

By substituting Eq. (5-34) into Eq. (5-23)-(5-24), the dynamic equation of the coupled system after introducing damping moments is achieved. Then, by solving the dynamic

equation, the joint angles of the HOBM can be obtained and also the Cartesian coordinates of the end effector of the HOBM.

The forces applied on the end effector of the cobot are shown in Figure 5-19. It can be seen that there are three forces applied on its end effector: cable force, gravitational and inertial forces of the payload. Hence, the total load on the cobot's end effector is:

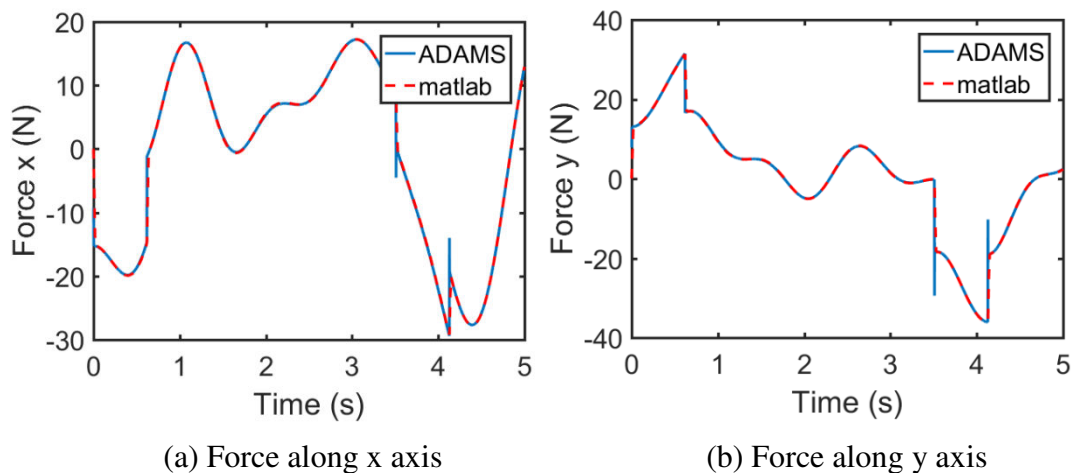
$$\mathbf{F}_{total} = -\mathbf{F}_{cable} + \mathbf{F}_{payload}^{gravity} + \mathbf{F}_{payload}^{inertia} \quad (5-35)$$

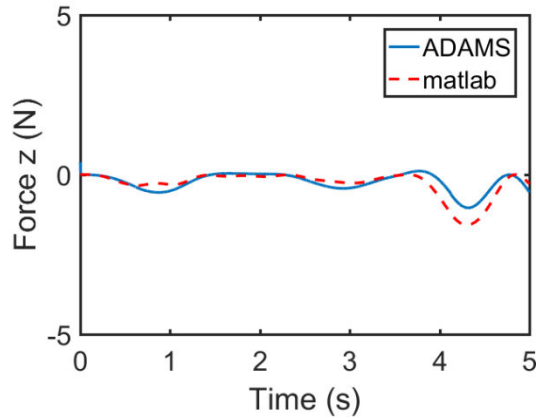


**Figure 5-19.** Forces applied on the end effector of the cobot

For validating the accuracy of the dynamic model of the HOBM-cobot coupled system after introducing damping moments, a Simulink model has been developed via Matlab and simulation results are compared with the results of the ADAMS model. The mass of the payload is 30kg, the damping coefficients for the two joints of HOBM are both 0.2 Nms/deg and the trajectory parameters are the same as the trajectory 8 shown in Table 5-1.

The comparison of forces exerted on the cobot simulated by ADAMS model and Matlab model is shown in Figure 5-20. It can be seen from the figure that, for the forces along all three axes, the results from the ADAMS model and Matlab model are very close.





(c) Force along z axis

**Figure 5-20.** Comparison between the ADAMS and Matlab models.

### 5.3.5 Determination of admissible trajectory of the cobot while payload and HOBM are connected via a vertical rigid axis

The HOBM-cobot coupled system has the advantage that the gravity of the payload is compensated by the HOBM which allows the cobot to manipulate heavy load. However, despite the gravity of the payload was already compensated, noticeable forces are still applied on the cobot due to the payload's large mass with large acceleration and deceleration.

In addition, although by connecting the payload and HOBM through a rigid axis, the oscillation of the HOBM after the cobot stops its movement was eliminated. However, due to the significant inertia of the links of the HOBM, extra forces will be exerted on the cobot especially in the acceleration and deceleration phases.

These forces caused by the inertia effect of the HOBM and payload will create supplementary torques in the joints of the cobot which must be compensated by the motors of the cobot. After rigidly connecting the cobot with the HOBM, the dynamic equations describing the input torques of the cobot with the HOBM action can be expressed as:

$$\boldsymbol{\tau} = \boldsymbol{\tau}_{cobot} + \mathbf{J}_{cobot}^T \mathbf{F}_{total} \quad (5-36)$$

where,  $\boldsymbol{\tau}_{cobot}$  can be calculated by the dynamic equation of the cobot presented as Eq. (5-15).

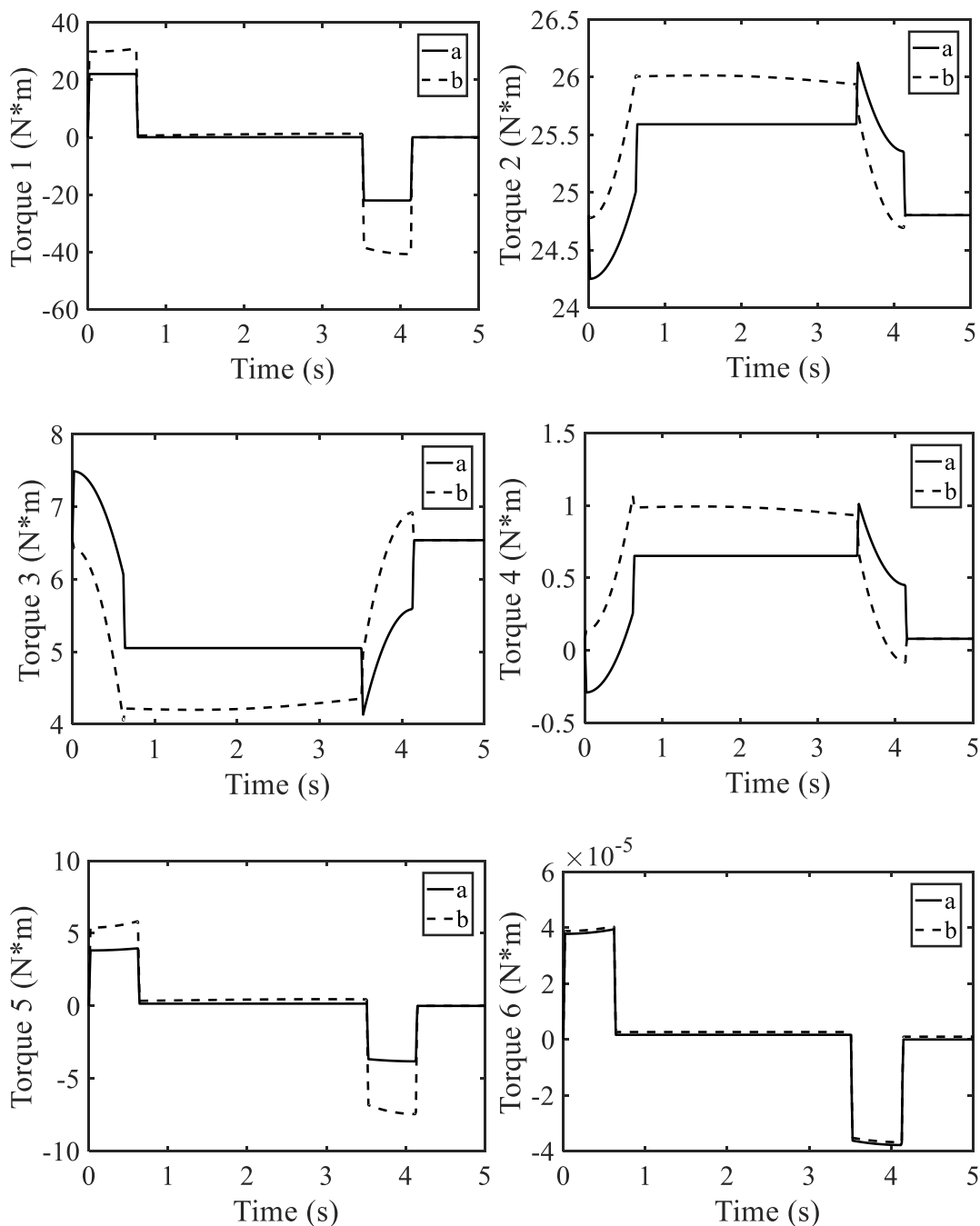


**Figure 5-21.** Input torques of the cobot: (a) without HOBM (b) taking into account inertial forces of the HOBM.

For investigating the inertial effect of the HOBM on the cobot, simulations via Matlab have been conducted before and after taking the inertial forces of the HOBM into consideration. The mass of the payload is 30kg and the trajectory parameters are same as the trajectory 8 shown in Table 5-1. Figure 5-21 shows the input torques of the cobot’s motors with and without taking the inertial forces of the HOBM into consideration. It can be seen that the inertial forces of the HOBM added great impedances during the acceleration and deceleration phases. Hence, during the determination of the trajectory, the maximum acceleration must be determined in order to let the required input torques lower than the maximum torques of the motors.



The maximum acceleration of the trajectory can be defined as the following: find  $\max\{\alpha\}$  subject to  $\max\{\mathbf{T}_{input}\} \leq \mathbf{T}_{max}$ , where  $\alpha$  is the angular acceleration of the trajectory,  $\mathbf{T}_{input}$  is the vector of input torques of the cobot's joints,  $\mathbf{T}_{max}$  is the vector of maximum torques of the motors of cobot.

The maximum torques of the motors of cobot UR10 are shown in Table 5-5. With these constraints of the motor torques, Figure 5-22 shows the maximum angular acceleration of the trajectory with respect to the payload mass when the HOBM and cobot are connected via a telescopic axis. It can be seen from the figure that the increase of the payloads mass leads to the reduction of the maximum acceleration of the executed trajectory.

**Table 5-5.** Maximum torques of the motors of cobot UR10

Joint No.	Maximum Torque (N*m)
1	330
2	330
3	150
4	56
5	56
6	56

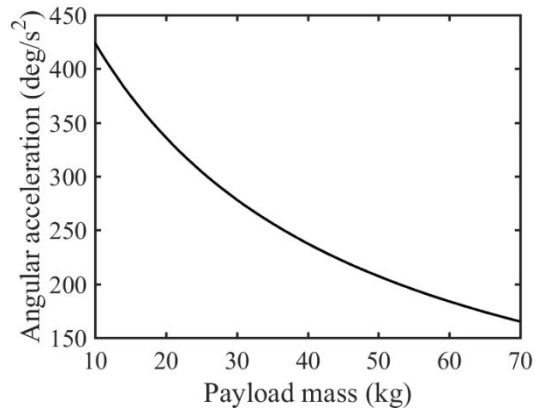


**Figure 5-22.** Maximum angular acceleration of the trajectory with respect to the payload mass when the HOBM and cobot are connected via a telescopic axis

### 5.3.6 Determination of admissible trajectory of the cobot after introducing damping moments on the HOBM

From the previous section, it can be seen that, due to the inertial effect of the HOBM, the maximum admissible acceleration has been restricted. That is due to the inertial forces induced by the HOBM become quite significant when the cobot operates at a high acceleration.

Apart from by rigidly connecting the cobot and the HOBM, another way for reducing the oscillation of the HOBM in the final phase of the trajectory is to introduce damping moments the joints of HOBM. However, as shown in the Section 5.2.3, although the oscillation in the final phase of the trajectory has been reduced after introducing damping moments, the forces applied on cobot in the moving phase of the trajectory is still considerable.

Similar to the previous section, after introducing damping moments on the HOBM, the dynamic equations describing the input torques of the cobot with the HOBM action can be obtained by substituting Eq. (5-35) into Eq. (5-36).

In order to investigate how the damping moments of the HOBM affect the load applied on the cobot, simulations via Matlab have been conducted for three cases: (a) no damping moments, (b) damping coefficients are  $0.4\text{ Nms/deg}$  and (c) damping coefficients are  $0.8\text{ Nms/deg}$ . The mass of the payload is 30kg and the trajectory parameters are same as the trajectory 8 shown in Table 5-1. Figure 5-23 shows the input torques of the cobot's motors with different damping coefficients. It can be seen that, for most of the motors of the cobot, the maximum values of the input torques have reduced after introducing damping moments on HOBM's joints. However, the input torques in the acceleration phase and deceleration phase is still quite significant which need to be taken into consideration in the trajectory planning.

For finding the maximum admissible acceleration of the trajectory, the same approach in the previous section is adopted, i.e. finding the maximum acceleration under the constraints of maximum motor torques. And the maximum torques of the cobot is also the same as shown in Table 5-5.

The maximum angular acceleration of the trajectory with respect to the payload mass before and after introducing damping moments is shown in Figure 5-24. It can be seen from the figure that the damping moments on the HOBM's joints only leads to a little improvement on the maximum acceleration when the payload is heavy. That is due to the total force applied by the HOBM through the cable is equal to the gravity of the payload. Hence, when the payload is light, the forces applied on the cobot is mainly due to the inertial force of the payload. Additionally, comparing to the case when the cobot and the HOBM are rigidly connected, the maximum admissible acceleration is much higher since the inertial effect of the HOBM is not directly applied on the cobot.

5.3 Dynamic modeling of the HOBM-cobot coupled system for determining admissible trajectories of the cobot

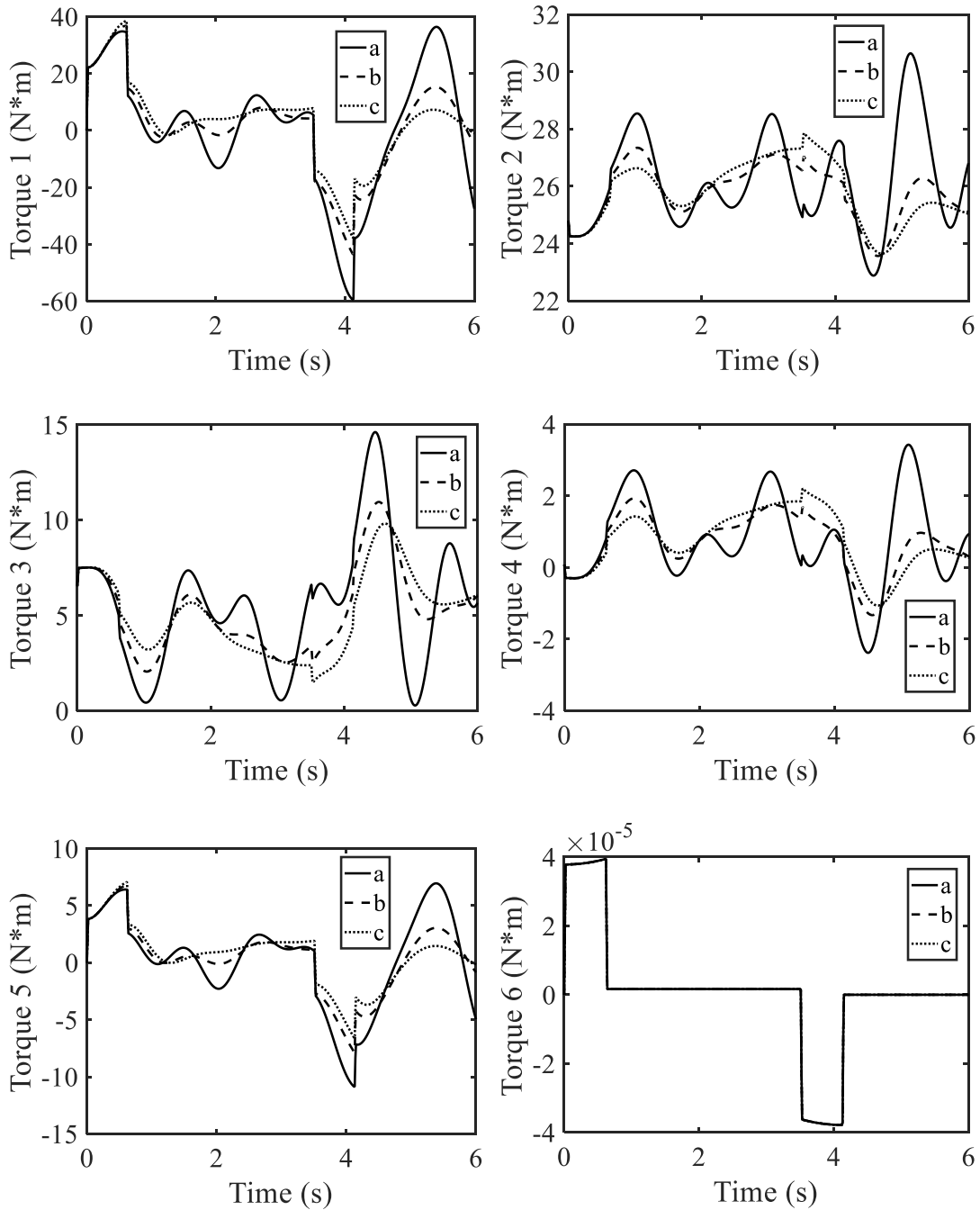


**Figure 5-23.** Input torques of the cobot: (a) no damping moments, (b) damping coefficients are 0.4 Nms/deg and (c) damping coefficients are 0.8 Nms/deg .

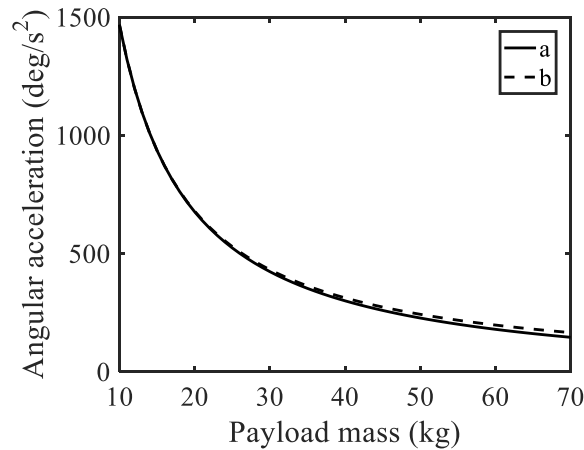


**Figure 5-24.** The maximum angular acceleration of the trajectory with respect to the payload mass: (a) no damping moment and (b) damping coefficients are  $0.8\text{ Nms/deg}$

## 5.4 Summary

Manual handling of loads involves the use of the human body to lift and carry loads. Most manufacturing systems require some manual handling tasks. When performed incorrectly or excessively, these tasks may expose workers to fatigue and injury. A variety of techniques and tools exist for automatic handling of heavy loads. Among them, collaborative robots and hand-operated balanced manipulators cooperation is an effective way. In this case, the operator controlling the HOBM is replaced by a cobot. Taking into account the great capabilities of the cobots, which allow human intervention to control and guide the payload, such cooperation is efficient since it does not exclude the possibility of having a human in the workspace of a robot.

This chapter presented the design and dynamic analysis of the HOBM-cobot coupled system. In the first section, the design concept of the coupled system has been proposed and optimization of the coupled system has been conducted in order to achieve a collision and singularity free workspace.

In the second section, the CAD model of the coupled system has been developed and simulations were carried out via ADAMS software. Simulation results showed that, in the final phase of the trajectory, oscillations of the links of the HOBM occurred due to its inertial effects. For reducing the oscillations, two solutions were proposed. The first is carried out by introducing a rigid telescopic axis linking HOBM and payload. And the second is carried out by introducing damping moments on the joints of HOBM. After implementing these methods, simulation results showed that the oscillation of the HOBM was effectively suppressed. However, the forces exerted on the cobot due to the inertial effect of the HOBM and payload are still significant.

For preventing inertial forces of the HOBM and payload being harmful to the cobot, in the last section, the admissible trajectories of the cobot taking into account the inertial effect of HOBM and after introducing damping moments were determined. The dynamic model of the cobot and HOBM has been developed for obtaining the cobot's input torques taking the inertial effect of HOBM and payload into consideration. The

maximum accelerations of the trajectory were determined for the payloads weighing from 10kg to 70kg. Results showed that, when the HOBM and cobot are rigidly connected through a telescopic axis, the inertial effect of the HOBM has a great impact on the maximum acceleration of the cobot. And the damping moments on the HOBM only leads to a little improvement of the maximum acceleration when the payload is relatively heavy.

The simulation results have been validated by experimental tests carried out in “Saunier Duval”.



---

## Conclusion and future works

---

### Conclusion

The work presented in this thesis deals with the design principles, which are based on the coupling of two mechanical structures. The criteria for optimal design and the types of combined units are different. Taking into consideration the coupling properties of given mechanical units the tasks are considered. The design and optimization of four main parts are considered: single actuator walking robots, gravity balancers, a robotic suit for load carriage and a handling system coupling manipulators with manual control and automatic weight balancing with cobot.

One of the effective ways to design a walking robot with reduced degrees of freedom is to use leg mechanisms intended to simulate the walking gait of a human. Such a walking robot has been designed by using of four-bar mechanisms. In order to let the four-bar mechanism generate the desired trajectory, a mechanism synthesis based on the Genetic Algorithm has been developed. The proposed geometric synthesis of the four-bar linkage allows one to find the lengths of links that ensure the reproduction of prescribed points of the given trajectory. The suggested walking robot consist of a moving frame connected with two synthesized four-bar linkages. The actuator of the walking robot mounted on its moving frame allows one moves both legs. Simulation results showed that the robot is capable to walk steadily both forward and backward at different constant speeds. However, such a robot can only generate a fixed gait pattern. Therefore, a one degree of freedom robot with adjustable slider-crank mechanism has been then proposed. The variations of the step length are carried out by changing the offset of the slider guide. The simulations have been carried out for four given combinations of adjustable parameters, and results showed that the robot has a steady walking cycle for all examined cases. To design a single actuator robot, which has the ability of both walking on the plane surface and climbing up the stairs, the robot must generate a tilted gait for reaching higher\lower stair. Thus, a similar walking robot including cam and pantograph mechanisms has been then discussed. The adjustable parameters are the angle between the cam mechanism and the robot body, as well as the fixed point position of the pantograph mechanism. Simulations were performed via ADAMS software. The obtained results showed that the change of fixed point position of the pantograph mechanism can significantly change the speeds of walking and climbing stairs, and it also can change the power consumption. On the other hand, the variation of the angle between cams and main body allows one to climb stairs, and the angle can be adjusted to adapt the slope of stairs.

In the thesis, the design and optimization of gravity balancers via coupling of a rotating link and a two-link dyad have been considered. It is known that a full gravity compensation of a rotating link cannot be achieved when a non-zero free length spring, i.e. conventional linear spring, is used. To use non-zero length springs, it is necessary to apply auxiliary mechanical systems. A simple and analytically tractable solution permitting to carry out quasi-perfect balancing of a rotating link by means of a non-zero length spring has been proposed. In the suggested design the balancing spring is connected with the rotating link by means of an articulated dyad forming a four-bar

linkage. Upon rotation of the output link of the four-bar mechanism moves the end of the spring and changes the length of the spring creating a variable balancing moment. An optimization method based on the geometric synthesis of four-bar mechanism and potential energy conservation has been developed, which allows one to control the optimal displacements of the spring providing a suitable balancing moment. The illustrative example has shown that the proposed design ensures gravity compensation up to 98%. A similar problem by coupling a rotating link to be balanced and a dyad with prismatic pair, forming with the rotating link a slider-crank mechanism has been then discussed. The particularity of the suggested design concept is that the balancing spring is installed on the fixed frame, which allows one to reduce the errors due to the spring's weight. The efficiency of the suggested mechanism design has been illustrated via numerical simulations. By selecting three prescribed positions of the rotating link has been reached a quasi-exact gravity balancing. It has been shown that the maximum value of the unbalanced moment reduced from 63 Nm to 2.92 Nm (95.4%), and in the case of 120 prescribed positions of the rotating link, the maximum value reduced up to 1.87 Nm (97%). In the next study, an improved solution for reducing the error caused by neglecting the masses of the spring and associated links has been proposed. In the inverted slider crank mechanism, considering the masses of the rocker and the spring, the balancing has been carried out. Firstly, it has been shown that the errors caused by neglecting the masses of the associated links lead to a significant unbalanced moment. Then, it was proposed to use the minimization of the root-mean-square value of the unbalanced moment to reduce these errors. The numerical simulations showed that the error caused by neglecting the masses of the associated links is more than 13% of the moment to be balanced. The application of the suggested solution has reduced the residual moment up to 40%. It was noticed that such an approach can be applied to other types of auxiliary linkages designed for gravity compensators.

The proposed robotic suit, which intends to assist its user in the carriage of heavy load, is a symbiosis of two systems: a rigid support frame and a cable system. The cable system coupled with the rigid support frame provides assistive force to its users during load carriage. It has two operation modes: passive and active modes. When wearers hold the load at a fixed posture, the cable locking mechanism is engaged to stop the movement of the cable and the robotic suit works in the passive mode where no energy is needed. When users change their postures while holding the load, the robotic suit works in the active mode providing variable assistive forces with respect to the movement.

The kinematic and dynamic models of the robotic suit system have been built. Static simulations have been carried out via built models and an optimization of the position of the anchors and attachment points of the robotic suit has been made based on genetic algorithm for minimizing the cable tension and force exerted on the shoulder. The workspace of the robotic suit has been analyzed, and dynamic simulations of the robotic suit have been carried. All simulations showed that the robot suit had good performances during working in both passive mode and active modes.

In order to evaluate the performance of the robotic suit in a more realistic environment, a mannequin test bench has been fabricated and tested. The test results showed that with the help of the robotic suit, the mannequin can hold different weights of loads steadily in different postures.



---

The last chapter of the thesis proposed a handling system coupling manipulators with manual control and automatic weight balancing with cobot. Manual handling of loads involves the use of the human body to lift and carry loads. Most manufacturing systems require some manual handling tasks. When performed incorrectly or excessively, these tasks may expose workers to fatigue and injury. A variety of techniques and tools exist for automatic handling of heavy loads. Among them, collaborative robots and hand-operated balanced manipulators cooperation is an effective way. In this case, the operator controlling the HOBM is replaced by a cobot. Taking into account the great capabilities of the cobots, which allow human intervention to control and guide the payload, such cooperation is efficient since it does not exclude the possibility of having a human in the workspace of a robot.

The thesis presented the design and dynamic analysis of the HOBM-cobot coupled system. The design concept of the coupled system has been proposed and optimization of the coupled system has been conducted in order to achieve a collision and singularity free workspace. The CAD model of the coupled system has been also developed and simulations were carried out via ADAMS software. Simulation results showed that, in the final phase of the trajectory, oscillations of the links of the HOBM occurred due to its inertial effects. For reducing the oscillations, two methods were proposed. The first is carried out by introducing a rigid telescopic axis linking HOBM and payload. The second is carried out by introducing damping moments on the joints of HOBM. After implementing these methods, simulation results showed that the oscillation of the HOBM was effectively reduced. However, the forces exerted on the cobot due to the inertial effect of the HOBM and payload are still significant. For preventing inertial forces of the HOBM and payload being harmful to the cobot, the admissible trajectories of the cobot taking into account the inertial effect of HOBM with damping moments were determined. The dynamic model of the cobot and HOBM has been developed for obtaining the cobot's input torques taking the inertial effect of HOBM and payload into consideration. The maximum accelerations of the trajectory were determined for the payloads from 10kg to 70kg. Results showed that, when the HOBM and cobot are rigidly connected through a telescopic axis, the inertial effect of the HOBM has a great impact on the maximum acceleration of the cobot. However, the damping moments on the HOBM only leads to a little improvement of the maximum acceleration when the payload is relatively heavy. The simulation results have been validated by experimental tests carried out in "Saunier Duval".

### **Future works**

This thesis generally focuses on the design of systems by coupling different mechanical structures and several examples in different fields are presented. In the last part of this manuscript, I would like to indicate some points which could be promising in the future work.

Firstly, for the walking robots with single actuator, it could be valuable to add an elastic unit on the walking mechanism for passively conserving and releasing energy. It can be seen from the first two walking robots that their energy consumptions in the propelling phase can be divided into positive and negative energy consumption which is due to the displacement of the center of gravity in the vertical axis. Therefore, by adding an elastic unit to compensate this effect will lead to a more energy-efficient walking robot.

Secondly, with respect to the robotic suit for load carriage, experiments were only conducted while the suit was working in the passive mode. In future, it is very worthwhile to test the robotic suit while working in the active mode and in the meantime to design a more sophisticated controller based on the tests in the real application. Additionally, with respect to the ergonomics, it is also valuable to improve the interface between cable attachment points and user for achieving better comfort.

Finally, for the cobot-HOBM coupled system, although this kind of system increased the payload capacity. However, compare to conventional industrial robots, the workspace of the coupled system is still quite small due to the limitation of the cobot. Hence, it could be very promising to install the system on a moving platform which can significantly increase its workspace.

---

---

## Bibliography

---

---

- [1] J. Horakova, "The (Short) Robot Chronicle (On the 20 th Century Cultural History of Robots)," in *Proc. Int. Workshop Robotics in the Alpe-Adria-Danube Region (RAAD)*, 2006.
- [2] H. O. Lim and A. Takanishi, "Biped walking robots created at Waseda University: WL and WABIAN family," *Philosophical Transactions of the Royal Society A: Mathematical, Physical and Engineering Sciences*, vol. 365, no. 1850, pp. 49–64, 2007.
- [3] I. KATO and H. Tsuik, "The Hydraulically powered Biped Walking Machine With a High Carrying Capacity," in *Proc. 4 th Int. Sys. on External Control of Human Extremities*, 1972.
- [4] A. M. M. Omer, R. Ghorbani, Hun-ok Lim, and Atsuo Takanishi, "Semi-passive dynamic walking for biped walking robot using controllable joint stiffness based on dynamic simulation," in *2009 IEEE/ASME International Conference on Advanced Intelligent Mechatronics*, 2009, pp. 1600–1605.
- [5] K. Hashimoto, K. Hattori, T. Otani, H.-O. Lim, and A. Takanishi, "Foot placement modification for a biped humanoid robot with narrow feet.," *The Scientific World Journal*, vol. 2014, 2014.
- [6] M. Vukobratovic, D. Hristic, and Z. Stojiljkovic, "Development of active anthropomorphic exoskeletons," *Medical and biological engineering*, vol. 12, no. 1, pp. 66–80, 1974.
- [7] M. Vukobratović, *Legged locomotion robots and anthropomorphic mechanisms : a monograph*. Beograd: Mihailo Pupin Institute, 1975.
- [8] M. Vukobratović and J. Stepanenko, "On the stability of anthropomorphic systems," *Mathematical Biosciences*, vol. 15, no. 1–2, pp. 1–37, Oct. 1972.
- [9] K. J. Waldron and R. B. McGhee, "The Adaptive Suspension Vehicle," *IEEE Control Systems Magazine*, pp. 7–12, 1986.
- [10] M. H. Raibert, H. B. Brown, and M. Chepponis, "Experiments in Balance with a 3D One-Legged Hopping Machine," *The International Journal of Robotics Research*, vol. 3, no. 2, pp. 75–92, Jun. 1984.
- [11] R. R. Playter and M. H. Raibert, "Control Of A Biped Somersault In 3D," in *Proceedings of the IEEE/RSJ International Conference on Intelligent Robots and Systems*, 1992, vol. 1, pp. 582–589.
- [12] M. Raibert, M. Chepponis, and H. Brown, "Running on four legs as though they were one," *IEEE Journal on Robotics and Automation*, vol. 2, no. 2, pp. 70–82,

- 1986.
- [13] J. Hodgins, “Legged robots on rough terrain: experiments in adjusting step length,” in *Proceedings. 1988 IEEE International Conference on Robotics and Automation*, 1988, pp. 824–826.
- [14] T. McGeer, “Passive Dynamic Walking,” *The International Journal of Robotics Research*, 1990.
- [15] S. H. Collins and A. Ruina, “A Bipedal Walking Robot with Efficient and Human-Like Gait,” in *Proceedings of the 2005 IEEE International Conference on Robotics and Automation*, 2005, pp. 1983–1988.
- [16] W. Saab, W. S. Rone, and P. Ben-Tzvi, “Robotic Modular Leg: Design, Analysis, and Experimentation,” *Journal of Mechanisms and Robotics*, vol. 9, no. 2, Mar. 2017.
- [17] Y. Sakagami, R. Watanabe, C. Aoyama, S. Matsunaga, N. Higaki, and K. Fujimura, “The intelligent ASIMO: system overview and integration,” in *IEEE/RSJ International Conference on Intelligent Robots and System*, 2002, vol. 3, pp. 2478–2483.
- [18] K. Hirai, M. Hirose, Y. Haikawa, and T. Takenaka, “The development of Honda humanoid robot,” in *Proceedings. 1998 IEEE International Conference on Robotics and Automation*, 1998, vol. 2, pp. 1321–1326.
- [19] K. Kaneko *et al.*, “Design of prototype humanoid robotics platform for HRP,” in *IEEE/RSJ International Conference on Intelligent Robots and System*, 2002, vol. 3, pp. 2431–2436.
- [20] K. Kaneko *et al.*, “Humanoid robot HRP-4 - Humanoid robotics platform with lightweight and slim body,” in *2011 IEEE/RSJ International Conference on Intelligent Robots and Systems*, 2011, pp. 4400–4407.
- [21] R. Playter, K. Blankespoor, J. Bondaryk, A. Rizzi, A. Saunders, and M. Raibert, “Building man and beast at Boston Dynamics,” in *Proceedings of the North America Conference on AUVSI Unmanned Systems*, 2012, p. 2:1041-1046.
- [22] “PLANTIGRADE MACHINE.” [Online]. Available: <http://en.tcheb.ru/1>. [Accessed: 25-May-2016].
- [23] H. Funabashi, Y. Takeda, I. Kawabuchi, and M. Higuchi, “Development of a walking chair with a self-attitude-adjusting mechanism for stable walking on uneven terrain,” in *Proc. 10th International Conference on the theory of machines and mechanisms*, 1999, pp. 1164–1169.
- [24] Y. Wu, M. Higuchi, Y. Takeda, and K. Sugimoto, “Development of a Power Assist System of a Walking Chair (Proposition of the Speed-Torque Combination Power Assist System),” *Journal of Robotics and Mechatronics*, vol. 17, no. 2, pp. 189–197, Apr. 2005.

- [25] E. Ottaviano, M. Ceccarelli, and C. Tavolieri, “Kinematic and Dynamic Analyses of a Pantograph-Leg for a Biped Walking Machine,” in *Climbing and Walking Robots*, Berlin, Heidelberg: Springer Berlin Heidelberg, 2005, pp. 561–568.
- [26] C. Liang, M. Ceccarelli, and Y. Takeda, “Operation Analysis of a One-DOF Pantograph Leg Mechanisms,” in *Proceedings of the RAAD 2008*, 2008.
- [27] R. P. Williams, L.-W. Tsai, and S. Azarm, “Design of a Crank-and-Rocker Driven Pantograph: A Leg Mechanism for the University of Maryland’s 1991 Walking Robot,” 1991.
- [28] W. B. Shieh, L. W. Tsai, and S. Azarm, “Design and optimization of a one-degree-of-freedom six-bar leg mechanism for a walking machine,” *Journal of Robotic Systems*, 1997.
- [29] P. Simionescu and I. Tempea, “Kinematic and kinetostatic simulation of a leg mechanism,” in *Proc. 10th International Conference on the theory of machines and mechanisms*, 1999.
- [30] J. Klann, “Walking device,” Patent US 6 478 314, 1998.
- [31] J. Klann, “Walking device,” Patent US 6 260 862, 1998.
- [32] N. G. Lokhande and V. B. Emche, “Mechanical Spider by Using Klann Mechanism,” *International Journal of Mechanical Engineering and Computer Applications*, 2013.
- [33] T. Rooney *et al.*, “Artificial active whiskers for guiding underwater autonomous walking robots,” in *CLAWAR 2011*, 2011.
- [34] “The Walking Beast.” [Online]. Available: <http://moltensteelman.com/thewalkingbeast.html>. [Accessed: 16-Oct-2018].
- [35] T. Jansen, *The great pretender*. 010 Publishers, 2007.
- [36] D. Giesbrecht, C. Q. Wu, and N. Sepehri, “Design and Optimization of an Eight-bar Legged Walking Mechanism Imitating a Kinetic Sculpture, ‘wind beast,’” *Transactions of the Canadian Society for Mechanical Engineering*, vol. 36, no. 4, pp. 343–355, Dec. 2012.
- [37] S. Nansai, M. R. Elara, and M. Iwase, “Dynamic Analysis and Modeling of Jansen Mechanism,” *Procedia Engineering*, vol. 64, pp. 1562–1571, Jan. 2013.
- [38] S.-W. Kim and D.-H. Kim, “Design of Leg Length for a Legged Walking Robot Based on Theo Jansen Using PSO,” *Journal of Korean Institute of Intelligent Systems*, vol. 21, no. 5, pp. 660–666, Oct. 2011.
- [39] L. Patnaik and L. Umanand, “Kinematics and dynamics of Jansen leg mechanism: A bond graph approach,” *Simulation Modelling Practice and*

- Theory*, vol. 60, pp. 160–169, Jan. 2016.
- [40] G. Devol, “Programmed article transfer,” Patent US 2 988 237, 1954.
- [41] N. Ulrich and V. Kumar, “Passive mechanical gravity compensation for robot manipulators,” in *Proceedings. 1991 IEEE International Conference on Robotics and Automation*, 1991.
- [42] V. Arakelian and S. Briot, *Balancing of Linkages and Robot Manipulators*, vol. 27. Cham: Springer International Publishing, 2015.
- [43] V. Arakelian, “Gravity compensation in robotics,” *Advanced Robotics*, 2016.
- [44] G. G. Lowen, F. R. Tepper, and R. S. Berkof, “Balancing of linkages-an update,” *Mechanism and Machine Theory*, 1983.
- [45] V. Arakelian, M. Dahan, and M. Smith, “A Historical Review of the Evolution of the Theory on Balancing of Mechanisms,” in *International Symposium on History of Machines and Mechanisms Proceedings HMM 2000*, Dordrecht: Springer Netherlands, 2000, pp. 291–300.
- [46] W. S. Newman and N. Hogan, “Time Optimal Control of Balanced Manipulators,” *Journal of Dynamic Systems, Measurement, and Control*, vol. 111, no. 2, pp. 187–193, Jun. 1989.
- [47] T. Laliberté, C. M. Gosselin, and M. Jean, “Static balancing of 3-DOF planar parallel mechanisms,” *IEEE/ASME Transactions on Mechatronics*, 1999.
- [48] A. Bayer and G. Merk, “Industrial robot with a weight balancing system,” Patent EP 2 301 727, 2011.
- [49] E. F. Fukushima *et al.*, “Teleoperated buggy vehicle and weight balanced arm for mechanization of mine detection and clearance tasks,” in *Proc. of the IARP International workshop on Robotics and Mechanical Assistance in Humanitarian Demining (HUDEM2005)*, 2005.
- [50] L. Bruzzone and G. Bozzini, “A statically balanced SCARA-like industrial manipulator with high energetic efficiency,” *Meccanica*, vol. 46, no. 4, pp. 771–784, Aug. 2011.
- [51] R. Yamamoto, A. Hirakawa, and O. Horikawa, “Load balancer with automatic lifting force compensation,” *ABCM Symposium Series in Mechatronics*, vol. 4, pp. 580–589, 2010.
- [52] C. Baradat, V. Arakelian, S. Briot, and S. Guegan, “Design and Prototyping of a New Balancing Mechanism for Spatial Parallel Manipulators,” *Journal of Mechanical Design*, 2008.
- [53] N. Lauzier, C. Gosselin, T. Laliberté, and P. Tremblay, “Adaptive gravity compensation of decoupled parallel and serial manipulators using a passive

- hydraulic transmission,” *Proceedings of the Institution of Mechanical Engineers, Part C: Journal of Mechanical Engineering Science*, 2009.
- [54] M. A. Lacasse, G. Lachance, J. Boisclair, J. Ouellet, and C. Gosselin, “On the design of a statically balanced serial robot using remote counterweights,” in *Proceedings - IEEE International Conference on Robotics and Automation*, 2013.
- [55] C. Baradat, V. Arakelian, and S. Briot, “Design of a Torque-Minimizing Mechanism for the Delta Parallel Robot,” in *20th Canadian Congress of Applied Mechanics: CANCAM 2005*, 2005.
- [56] S. Brudniok, G. Schreiber, and J. Maischberger, “Method and handling system for automated movement of a gravity-compensated load,” Patent EP 2 508 308, 2012.
- [57] S. Patarinski, “Robot-balancing manipulator cooperation for handling of heavy parts,” in *Proceedings of 15th International Symposium Industrial Robot*, 1985, pp. 649–656.
- [58] T. ARAI, “Construction System of Heavy Parts by the Coordinated control between a Crane and a Robot,” in *Proc. 9th Int. Symp. on Automation and Robotics in Construction*, 1992, vol. 2, pp. 879–886.
- [59] S. K. Agrawal and A. Fattah, “Theory and Design of an Orthotic Device for Full or Partial Gravity-Balancing of a Human Leg During Motion,” *IEEE Transactions on Neural Systems and Rehabilitation Engineering*, vol. 12, no. 2, pp. 157–165, Jun. 2004.
- [60] S. Krut, M. Benoit, E. Dombre, and F. Pierrot, “MoonWalker, a lower limb exoskeleton able to sustain bodyweight using a passive force balancer,” in *2010 IEEE International Conference on Robotics and Automation*, 2010, vol. 19, no. 6, pp. 2215–2220.
- [61] Y. Ikeuchi, J. Ashihara, Y. Hiki, H. Kudoh, and T. Noda, “Walking assist device with bodyweight support system,” in *2009 IEEE/RSJ International Conference on Intelligent Robots and Systems*, 2009, pp. 4073–4079.
- [62] G. Carwardine, “Improvement in elastic force mechanisms,” Patent UK 377251, 1932.
- [63] G. Endo, H. Yamada, A. Yajima, M. Ogata, and S. Hirose, “A weight compensation mechanism with a non-circular pulley and a spring: Application to a parallel four-bar linkage arm,” *SICE Journal of Control, Measurement, and System Integration*, vol. 3, no. 2, pp. 130–136, 2010.
- [64] I. Ebert-Uphoff and K. Johnson, “Practical considerations for the static balancing of mechanisms of parallel architecture,” *Proceedings of the Institution of Mechanical Engineers, Part K: Journal of Multi-body Dynamics*, 2002.

- 
- [65] J. Wang and C. M. Gosselin, "Passive mechanisms with multiple equilibrium configurations," *Transactions of the Canadian Society for Mechanical Engineering*, 2004.
- [66] V. Arakelian and M. Dahan, "Equilibrage optimal des mécanismes pour manipulateur," in *Actes du 12e Congrès Français de Mécanique*, 1995, pp. 373–376.
- [67] I. Simionescu and L. Ciupitu, "Static balancing of the industrial robot arms. Part I: discrete balancing," *Mechanism and Machine Theory*, vol. 35, no. 9, pp. 1287–1298, 2000.
- [68] J. Hervé, "Device for counter-balancing the forces due to gravity in a robot arm," Patent FR 2 565 153, 1985.
- [69] R. Dzhavakhyan and N. Dzhavakhyan, "Balanced manipulator," Patent SU 1 521 579, 1989.
- [70] S. Segla, C. M. Kalker-Kalkman, and A. L. Schwab, "Statical balancing of a robot mechanism with the aid of a genetic algorithm," *Mechanism and Machine Theory*, vol. 33, no. 1–2, pp. 163–174, Jan. 1998.
- [71] L. Ciupitu and I. Simionescu, "Zero-free-length elastic systems for static balancing," in *New Advances in Mechanisms, Mechanical Transmissions and Robotics*, Springer, Cham, 2017, pp. 59–67.
- [72] S. K. Banala *et al.*, "Gravity-balancing leg orthosis and its performance evaluation," *IEEE Transactions on Robotics*, vol. 22, no. 6, pp. 1228–1239, Dec. 2006.
- [73] J. Herder, "Development of a statically balanced arm support: ARMON," in *9th International Conference on Rehabilitation Robotics, 2005. ICORR 2005.*, 2005, pp. 281–286.
- [74] S. K. Banala, S. H. Kim, S. K. Agrawal, and J. P. Scholz, "Robot assisted gait training with active leg exoskeleton (ALEX)," *Proceedings of the 2nd Biennial IEEE/RAS-EMBS International Conference on Biomedical Robotics and Biomechatronics, BioRob 2008*, vol. 17, no. 1, pp. 653–658, 2008.
- [75] I. Simionescu and L. Ciupitu, "Static balancing of the industrial robot arms. Part II: continuous balancing," *Mechanism and Machine Theory*, 2000.
- [76] C. Cho, W. Lee, J. Lee, and S. Kang, "A 2-dof gravity compensator with bevel gears," *Journal of Mechanical Science and Technology*, 2012.
- [77] H. S. Kim, J. K. Min, and J. B. Song, "Multiple-Degree-of-Freedom Counterbalance Robot Arm Based on Slider-Crank Mechanism and Bevel Gear Units," *IEEE Transactions on Robotics*, vol. 32, no. 1, pp. 230–235, 2016.
- [78] J. Colgate and M. Peshkin, "Cobots," Patent US 5 952 796, 1997.



- [79] J. E. Colgate, M. Peshkin, and S. H. Klostermeyer, "Intelligent assist devices in industrial applications: a review," in *Proceedings 2003 IEEE/RSJ International Conference on Intelligent Robots and Systems (IROS 2003)*, vol. 3, pp. 2516–2521.
- [80] V. Arakelian, "The History of the Creation and Development of Hand-Operated Balanced Manipulators (HOBM)," in *International Symposium on History of Machines and Mechanisms*, Dordrecht: Springer Netherlands, 2004, pp. 347–356.
- [81] R. A. Olsen, "Balanced assembly," Patent US 3 134 340, 1964.
- [82] R. A. Olsen, "Loading balanced assembly," Patent US 3 259 352, 1966.
- [83] P. N. Belyanin, "Balanced manipulators," *Ed. Mashinostroyenie*, p. 263p, 1988.
- [84] R. Matsumoto, "Load handling equipment," Patent US 3 883 105, 1975.
- [85] I. Vladov and V. Danilevskij, "Loading manipulator," Patent SU 83113, 1981.
- [86] I. Vladov and V. Danilevskij, "Balancing manipulator," Patent SU 1423367, 1999.
- [87] R. Djavakhian and N. Djavakhian, "Balanced manipulator," Patent SU 1521579, 1988.
- [88] G. Derkach and A. Umantsev, "Balanced manipulator," Patent SU 1546408, 1990.
- [89] G. Derkach, "Balanced manipulator," Patent SU 1826956, 1993.
- [90] Y. Zhang, V. Arakelian, and J. Le Baron, "Design concepts and functional particularities of wearable walking assist devices and power-assist suits – a review," in *Proceedings of the 58th International Conference of Machine Design Departmentants (ICDM'2017)*, 2017, no. September, pp. 436–441.
- [91] D. Lloyd-Jones *et al.*, "Heart disease and stroke statistics-2010 update: A report from the american heart association," *Circulation*. 2010.
- [92] T. Hayashi, H. Kawamoto, and Y. Sankai, "Control method of robot suit HAL working as operator's muscle using biological and dynamical information," in *2005 IEEE/RSJ International Conference on Intelligent Robots and Systems, IROS, 2005*.
- [93] K. Suzuki, G. Mito, H. Kawamoto, Y. Hasegawa, and Y. Sankai, "Intention-based walking support for paraplegia patients with Robot Suit HAL," *Advanced Robotics*, 2007.
- [94] A. Goffer, "Gait-locomotor apparatus," Patent US 7 153 242, 2006.

- [95] T. Fujil, Y. Koyama, H. Katoh, T. Hirata, A. Koike, and T. Koyama, "Walking aid device," Patent US 10/557,338, 2006.
- [96] R. Rea, C. Beck, R. Rovekamp, P. Neuhaus, and M. Diftler, "X1: A robotic exoskeleton for in-space countermeasures and dynamometry," in *AIAA SPACE 2013 Conference and Exposition*, 2013.
- [97] A. Zoss, H. Kazerooni, and A. Chu, "On the mechanical design of the Berkeley Lower Extremity Exoskeleton (BLEEX)," in *2005 IEEE/RSJ International Conference on Intelligent Robots and Systems, IROS*, 2005, pp. 3132–3139.
- [98] M. Wehner *et al.*, "A lightweight soft exosuit for gait assistance," *Proceedings - IEEE International Conference on Robotics and Automation*, pp. 3362–3369, 2013.
- [99] A. T. Asbeck, K. Schmidt, and C. J. Walsh, "Soft exosuit for hip assistance," *Robotics and Autonomous Systems*, vol. 73, pp. 102–110, 2015.
- [100] Y. Ding, I. Galiana, C. Siviyy, F. A. Panizzolo, and C. Walsh, "IMU-based iterative control for hip extension assistance with a soft exosuit," in *Proceedings - IEEE International Conference on Robotics and Automation*, 2016.
- [101] Y. Ding *et al.*, "Biomechanical and physiological evaluation of multi-joint assistance with soft exosuits," *IEEE Transactions on Neural Systems and Rehabilitation Engineering*, vol. 25, no. 2, pp. 119–130, 2017.
- [102] R. M. Enoka and J. Duchateau, "Muscle fatigue: What, why and how it influences muscle function," *Journal of Physiology*. 2008.
- [103] Ł. Jaworski, R. Karpiński, and A. Dobrowolska, "Biomechanics of the upper limb," *Journal of Technology and Exploitation in Mechanical Engineering*, vol. 2, no. 1, pp. 53–59, 2016.
- [104] "FORTIS | Lockheed Martin." [Online]. Available: <https://www.lockheedmartin.com/en-us/products/exoskeleton-technologies/industrial.html>. [Accessed: 17-Oct-2018].
- [105] "EXHAUSS." [Online]. Available: [http://www.exhauss.com/fr\\_modelew.htm](http://www.exhauss.com/fr_modelew.htm). [Accessed: 17-Oct-2018].
- [106] D. M. Baechle, E. D. Wetzel, and S. K. Agrawal, "MAXFAS: Mechatronic Arm Exoskeleton for Firearm Aim Stabilization," *Journal of Mechanisms and Robotics*, vol. 8, no. 6, 2016.
- [107] "ISO 10218-1: 2011: Robots and robotic devices—Safety requirements for industrial robots—Part 1: Robots," Geneva, Switzerland, 2011.
- [108] G. Hirzinger *et al.*, "DLR's torque-controlled light weight robot III—are we reaching the technological limits now?," in *Proceedings 2002 IEEE International Conference on Robotics and Automation*, 2002, vol. 2, pp. 1710–

- 1716.
- [109] J. A. Hrones and G. L. Nelson, *Analysis of the Four-Bar Linkage Its Application to the Synthesis of Mechanisms*. Mit Pr, 1951.
- [110] R. S. Hartenberg and J. Denavit, *Kinematic synthesis of linkages*. McGraw-Hill, 1964.
- [111] F. Freudenstein, “Approximate synthesis of four-bar linkages,” *Resonance*, vol. 15, no. 8, pp. 740–767, Aug. 2010.
- [112] I. Artobolevski, *Théorie des mécanismes et des machines*. Moscou: Ed. Mir, 1977.
- [113] A. G. Erdman and G. N. Sandor, *Advanced Mechanism Design : Analysis and Synthesis Vol. 2*. Prentice-Hall, 1984.
- [114] D. E. Goldberg, *Genetic Algorithms in Search, Optimization, and Machine Learning*. Addison Wesley, 1989.
- [115] S. S. Balli and S. Chand, “Transmission angle in mechanisms (Triangle in mech),” *Mechanism and Machine Theory*, vol. 37, no. 2, pp. 175–195, Feb. 2002.
- [116] V. Arakélian, *Structure et cinématique des mécanismes*. Hermès, 1997.
- [117] J. L. Herder, “Energy-free systems: theory, conception, and design of statically balanced spring mechanisms,” Technische Universiteit Delf, 2001.
- [118] M. R. Smith and L. Maunder, “Inertia Forces in a Four-Bar Linkage,” *Journal of Mechanical Engineering Science*, vol. 9, no. 3, pp. 218–225, Jun. 1967.
- [119] V. Arakelian and S. Ghazaryan, “Improvement of balancing accuracy of robotic systems: Application to leg orthosis for rehabilitation devices,” *Mechanism and Machine Theory*, 2008.
- [120] R. Drillis, R. Contini, and M. Bluestein, *Body segment parameters*. New York University, School of Engineering and Science, 1969.
- [121] D. Whitley, “A genetic algorithm tutorial,” *Statistics and Computing*, 1994.
- [122] H. D. Taghirad, *Parallel robots: mechanics and control*. CRC press, 2013.
- [123] N. Saeed, *Introduction to Robotics*. Pearson Prentice Hall, 2001.



### Kinematic and dynamic equation of the robotic suit

This appendix shows the detailed form of the kinematic and dynamic equation of the robotic suit in section 4.2.

The detailed form of the Eq. (4-3) is:

$$\begin{aligned}
 f_1(\theta_1, \theta_2) = & \sqrt{\left[ d_1 \cos(\theta_1 + \theta_2) + (a_1 - b_1) \sin(\theta_1 + \theta_2) - d_2 \cos \theta_1 - (a_2 - b_2 - l_{ar}) \sin \theta_1 \right]^2 +} \\
 & \sqrt{\left[ (a_1 - b_1) \cos(\theta_1 + \theta_2) - d_1 \sin(\theta_1 + \theta_2) - (a_2 - b_2 - l_{ar}) \cos \theta_1 + d_2 \sin \theta_1 \right]^2} \\
 & + \sqrt{(a_3 + a_2 \cos \theta_1 - b_2 \cos \theta_1 - d_2 \sin \theta_1)^2 + (b_3 - d_2 \cos \theta_1 - a_2 \sin \theta_1 + b_2 \sin \theta_1)^2} \\
 & + \sqrt{b_1^2 + (c_1 - d_1)^2} + l_0
 \end{aligned} \tag{A-1}$$

$$\begin{aligned}
 f_2(\theta_1) = & \sqrt{\left[ a_3 + (a_2 - b_2) \cos \theta_1 - d_2 \sin \theta_1 \right]^2 + \left[ b_3 - d_2 \cos \theta_1 - (a_2 - b_2) \sin \theta_1 \right]^2} \\
 & + \sqrt{b_2^2 + (c_2 - d_2)^2} + l_0
 \end{aligned} \tag{A-2}$$

The Jacobean matrix of the robotic suit is:

$$\mathbf{J}_v = \begin{bmatrix} j_{11}^v & j_{12}^v \\ j_{21}^v & j_{22}^v \end{bmatrix} \tag{A-3}$$

, where:

$$j_{12}^v = \frac{\left[ (a_1 - b_1)(a_2 - b_2 - l_{ar}) + d_1 d_2 \right] \sin \theta_2 + \left[ d_1 (a_2 - b_2 - l_{ar}) - d_2 (a_1 - b_1) \right] \cos \theta_2}{\sqrt{\left[ d_1 \cos(\theta_1 + \theta_2) + (a_1 - b_1) \sin(\theta_1 + \theta_2) - d_2 \cos \theta_1 - (a_2 - b_2 - l_{ar}) \sin \theta_1 \right]^2 + \left[ (a_1 - b_1) \cos(\theta_1 + \theta_2) - d_1 \sin(\theta_1 + \theta_2) - (a_2 - b_2 - l_{ar}) \cos \theta_1 + d_2 \sin \theta_1 \right]^2}}$$

$$j_{11}^v = j_{21}^v = \frac{(a_3 b_2 - a_3 a_2 + b_3 d_2) \sin \theta_1 - (b_3 a_2 - b_3 b_2 + a_3 d_2) \cos \theta_1}{\sqrt{\left[ a_3 + (a_2 - b_2) \cos \theta_1 - d_2 \sin \theta_1 \right]^2 + \left[ b_3 - d_2 \cos \theta_1 - (a_2 - b_2) \sin \theta_1 \right]^2}}$$

$$j_{22}^v = 0$$

The detailed form of dynamic equation of the robotic suit Eq. (4-12) is:

$$\left\{ \begin{array}{l}
 M_{\text{shoulder}}^{\text{cable}} = \left[ m_{ua} l_{cua}^2 + I_{ua} + m_{fa} (l_{ua}^2 + l_{cfa}^2 + 2l_{ua} l_{cfa} \cos \theta_2) + I_{fa} + m_{load} (l_{ua}^2 + l_{cload}^2 + 2l_{ua} l_{cload} \cos \theta_2) \right] \ddot{\theta}_1 \\
 \quad + \left[ m_{fa} (l_{cfa}^2 + l_{ua} l_{cfa} \cos \theta_2) + I_{fa} + m_{load} (l_{cload}^2 + l_{ua} l_{cload} \cos \theta_2) \right] \ddot{\theta}_2 - m_{fa} l_{ua} l_{cfa} \sin \theta_2 (2\dot{\theta}_1 \dot{\theta}_2 + \dot{\theta}_2^2) \\
 \quad - m_{load} l_{ua} l_{cload} \sin \theta_2 (2\dot{\theta}_1 \dot{\theta}_2 + \dot{\theta}_2^2) + m_{ua} g l_{cua} \sin \theta_1 + m_{fa} g [l_{ua} \sin \theta_1 + l_{cfa} \sin(\theta_1 + \theta_2)] \\
 \quad + m_{load} g [l_{ua} \sin \theta_1 + l_{cload} \sin(\theta_1 + \theta_2)] \\
 M_{\text{elbow}}^{\text{cable}} = \left[ m_{ua} (l_{cfa}^2 + l_{ua} l_{cfa} \cos \theta_2) + I_{fa} \right] \ddot{\theta}_1 + (m_{fa} l_{cfa}^2 + I_{fa} + m_{load} l_{cload}^2) \ddot{\theta}_2 \\
 \quad + (m_{fa} l_{cfa} + m_{load} l_{cload}) l_{ua} \sin \theta_2 \dot{\theta}_1^2 + (m_{fa} l_{cfa} + m_{load} l_{cload}) g \sin(\theta_1 + \theta_2)
 \end{array} \right. \quad (\text{A-4})$$

## Simulink model for the dynamic simulation of the robotic suit

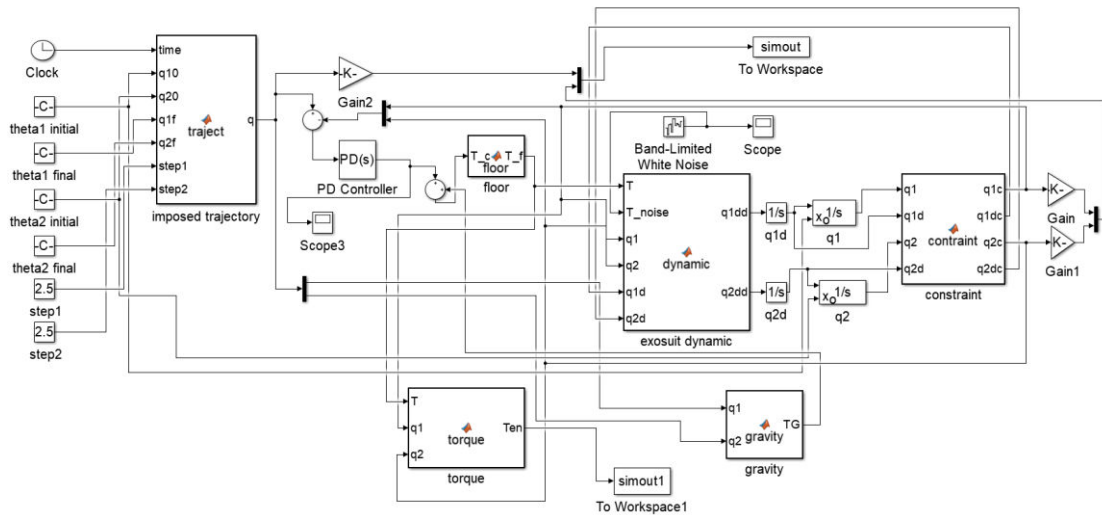


**Figure B-1.** Simulink model of the robotic suit with PD controller





## Simulink models of the cobot-HOBM coupled system in Chapter 5

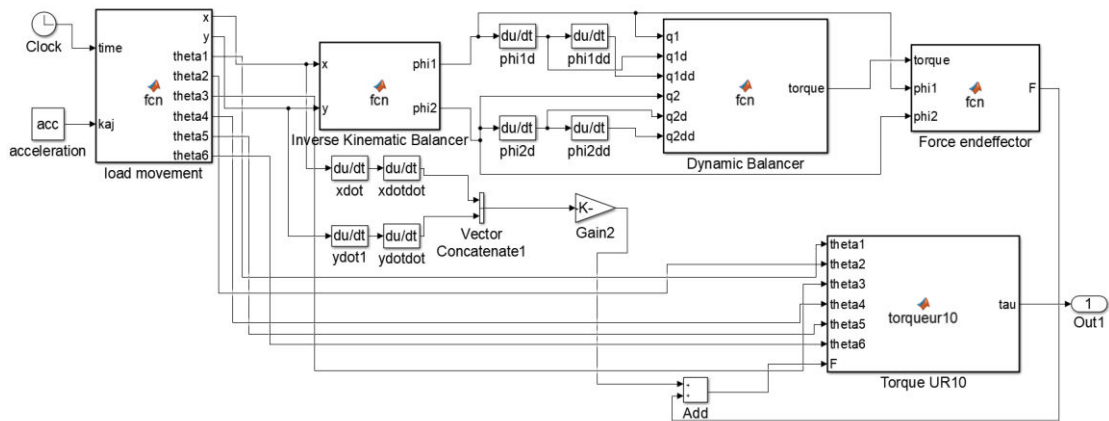


**Figure C-1.** The general system of the cobot-HOBM coupled dynamic model when cobot and HOBM are linked via a telescopic axis

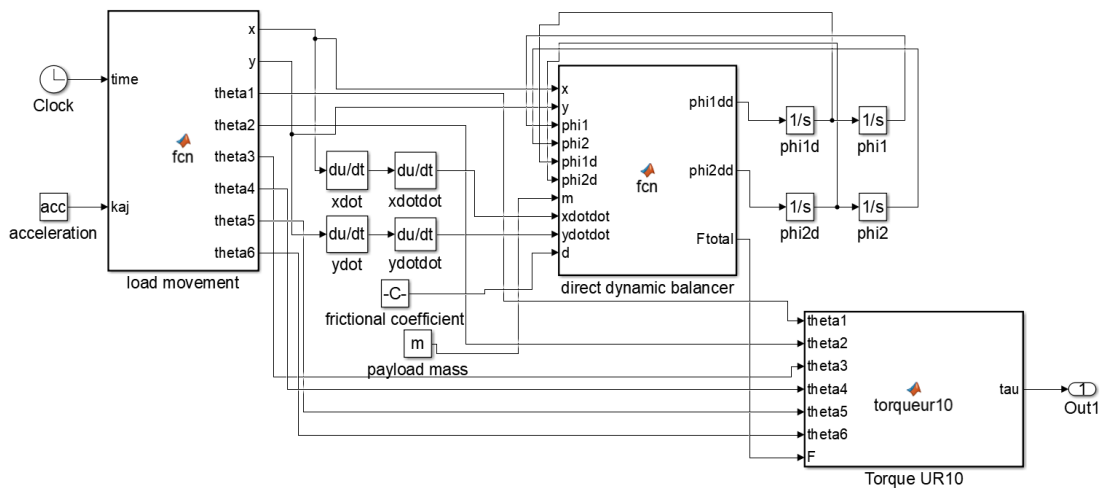


**Figure C-2.** The general system of the cobot-HOBM coupled dynamic model after introducing frictions on the HOBM's joints



---

---

## List of publications

---

---

### Peer-reviewed journals

[1] **Y. Zhang** and V. Arakelian, “Design of a Single Actuator Walking Robot via Mechanism Synthesis Based on Genetic Algorithms,” *Journal of Robotics and Mechanical Engineering Research*, vol2(3): 1-7, 2018.

[2] V. Arakelian and **Y. Zhang**, “An Improved Design of Gravity Compensators Based on the Inverted Slider-Crank Mechanism,” *ASME. Journal of Mechanisms and Robotics*. (Accepted, in press)

### Conference proceedings

[1] **Y. Zhang**, V. Arakelian, “Design of a Passive Robotic ExoSuit for Carrying Heavy Loads,” in *IEEE-RAS 18th International Conference on Humanoid Robots (Humanoids)*, November 6-9, Beijing, China, 2018.

[2] **Y. Zhang**, V. Arakelian and J.P. Le Baron, “Linkage Design for Gravity Balancing by Means of Non-zero Length Springs,” in *22nd CISM IFToMM Symposium on Robot Design, Dynamics and Control (ROMANSY 2018)*, June 25-28, Rennes, France, 2018.

[3] V. Arakelian, **Y. Zhang**, “Improvement of the Balancing Accuracy in Gravity Compensators Based on the Inverted Slider Crank Mechanism,” in *ASME 2018 International Design Engineering Technical Conferences and Computers and Information in Engineering Conference (IDETC-CIE 2018)*, August 26-29, Quebec City, Quebec, Canada, 2018.

[4] **Y. Zhang**, V. Arakelian and J.P. Le Baron, “Design concepts and functional particularities of wearable walking assist devices and power-assist suits - a review,” in *Proceedings of the 58th International Conference of Machine Design Departments (ICDM'2017)*, September 6-8, Prague, Czech Republic, pp. 436-441, 2017.

[5] **Y. Zhang**, V. Arakelian and J.P. Le Baron. “Design of a legged walking robot with adjustable parameters,” in *Proceedings of the 12th International Conference on the Theory of Machines and Mechanisms*, September 6-9, Liberec, Czech Republic, pp. 65-71, 2016.

[6] **Y. Zhang**, V. Arakelian, B. Véron and D. Chablat, “Key Features of the Coupled Hand-operated Balanced Manipulator (HOBM) and Lightweight Robot (LWR),” *The 15th IFToMM World Congress*, June 30 – July 4, 2019, Krakow, Poland. (Accepted)



## AVIS DU JURY SUR LA REPRODUCTION DE LA THESE SOUTENUE

**Titre de la thèse:**

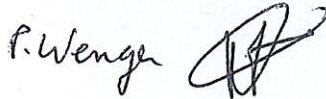
Design and synthesis of mechanical systems with coupled units

**Nom Prénom de l'auteur : ZHANG YANG**

**Membres du jury :**

- Monsieur BEN OUEZDOU Féthi
- Monsieur COSTE Michel
- Madame SMITH-GUERIN Nathalie
- Monsieur WENGER Philippe
- Monsieur ARAKELYAN Vigen
- Monsieur Aoustin Yannick
- Monsieur DELALEAU Emmanuel

Président du jury :



Date de la soutenance : 19 Avril 2019

Reproduction de la these soutenue

- Thèse pouvant être reproduite en l'état  
 Thèse pouvant être reproduite après corrections suggérées

Fait à Rennes, le 19 Avril 2019

Signature du président de jury



Le Directeur,

M'hamed DRISSI



**Titre :** CONCEPTION ET SYNTHÈSE DES SYSTÈMES MÉCANIQUES AUX UNITÉS COUPLÉES.....

**Mots clés :** Conception de mécanismes, Robot marcheur, Équilibrage de la gravité, Exosquelette, Système couplé

**Résumé :** Ce mémoire traite de nouveaux principes de conception qui sont inspirés par le couplage de deux unités représentant les différentes structures mécaniques. Les critères de conception optimale et les types d'unités combinées sont différents. Cependant, toutes les tâches sont considérées dans le couplage de ces unités.

L'examen critique présenté dans le premier chapitre est divisé en trois sections en raison de la nature des problèmes traités : les robots marcheurs, les compensateurs de gravité et les robots collaboratifs. Le deuxième chapitre traite du développement de robots marcheurs à actionneur unique, conçus par couplage de deux mécanismes ayant les fonctionnements de jambe. Basée sur l'algorithme génétique, la synthèse proposée permet d'assurer la reproduction de la trajectoire obtenue à partir de la marche humaine. Par l'ajustement des paramètres

géométriques des unités conçues, il devient possible non seulement d'assurer une marche du robot à des pas variables, mais également de monter les escaliers. Ensuite la conception et la synthèse des équilibreurs pour les robots sont considérés. Un costume robotisé type exosquelette permettant d'aider aux personnes transportant des charges lourdes est examiné dans le chapitre suivant. La conception proposée présente une symbiose d'un support rigide et léger et d'un système de câbles monté sur ce support. L'étude et l'optimisation statique et dynamique ont conduit aux tests sur un mannequin. Le dernier chapitre propose l'étude et l'optimisation d'un système couplé, comprenant un manipulateur équilibré à commande manuelle et un robot collaboratif. Le but d'une telle coopération est de manipuler de lourdes charges avec un cobot.

**Title:** DESIGN AND SYNTHESIS OF MECHANICAL SYSTEMS WITH COUPLED UNITS.....

**Keywords:** Mechanism design, Walking robot, Gravity balancing, Exoskeleton, Coupled system

**Abstract:** This thesis deals with the design principles, which are based on the coupling of two mechanical structures. The criteria for optimal design and the types of combined units are different. However, all the tasks are considered in coupling of given mechanical units.

The critical review given in the first chapter is divided into three sections due to the nature of the examined problems: legged walking robots, gravity compensators used in robots and collaborative robots. Chapter two deals with the development of single actuator walking robots designed by coupling of two mechanisms. Based on the Genetic Algorithm, the synthesis allows one to ensure the reproduction of prescribed points of the given trajectory obtained from the walking gait. By adjusting the geometric parameters of the designed units, it becomes possible not only to operate the robot at variable steps, but also

to climb the stairs. The next chapter deals with the design and synthesis of gravity balancers. A robotic that can help people carrying heavy load is the subject of chapter four. The proposed exosuit presents a symbiosis of two systems: rigid lightweight support and cable system. Static and dynamic study and optimization are considered. Experiments are also carried out on a mannequin test bench. The last chapter presents a coupled system including a hand-operated balanced manipulator (HOBM) and an industrial collaborative robot. The aim of such a cooperation is to manipulate heavy payloads with less powerful robots. Dynamic analysis of the coupled system is performed and methods for reducing the oscillation of the HOBM at the final phase of the prescribed trajectories are proposed.